UNIVERSITY OF CALIFORNIA, SAN DIEGO

X-Ray Studies of Diffusion Dynamics in Nano-Confined Geometries

A dissertation submitted in partial satisfaction of the
requirements for the degree
Doctor of Philosophy

in

Physics

by

Leandra Boucheron

Committee in charge:

Oleg Shpyrko, Chair
Michael Anderson
Ying Shirley Meng
Sunil Sinha
Andrea Tao

2015

The dissertation of Leandra Boucheron is approved, and it is acceptable in quality and form for publication on microfilm and electronically:

_____

_____

_____

_____

_____

Chair

University of California, San Diego

2015

EPIGRAPH

I do not know what I may appear to the world, but to myself I seem to have been only like a boy playing on the sea-shore, and diverting myself in now and then finding a smoother pebble or a prettier shell than ordinary, whilst the great ocean of truth lay all undiscovered before me.

—Sir Isaac Newton

Graduate school is where you choose to forgo current earnings so that you can later forgo future earnings.

—Oleg Shpyrko

Synchrotrons. They generate pure and more complete patterns than x-ray beams. Data collection takes a fraction of the time.

—Walter White, *Breaking Bad*

TABLE OF CONTENTS

LIST OF FIGURES

LIST OF TABLES

ACKNOWLEDGEMENTS

In early elementary school, I wrote that "I want to be an author, a teacher, a mathematician, a magician, a musician, and a mom when I grow up." This list of career aspirations is admittedly daunting for me in retrospect, nearly two decades later. As I am completing my Ph.D., I am beginning my post-school career as a lecturer at the University of New Mexico. And with the publication of this dissertation, I suppose you could say I'm two for six on career goals. We'll see what the future holds. But it's taken a long time and the help of many individuals and groups to get me this far, so lest I seem ungrateful that I haven't achieved much in the eyes of my younger self, I think it best to give credit where credit is due.

Thank you to my parents Susan and Edward for their constant love, support, and upbringing over the years.

Thank you to my sister Laura for putting up with my constant tattling as a child.

Thank you to my sister Alina, who has turned into my lifelong best friend despite being a constant source of annoyance to me as a child.

Thank you to my teachers, preschool and grades 1-11 for my educational background.

Thank you to the high school nurse for signing the form to allow me to withdraw from school, despite insisting that I was throwing my life away.

Thank you to my professors from New Mexico Tech for providing me with the best undergraduate education I can imagine.

Thank you to my mentors from Sandia National Laboratories for giving me an introduction to the world of research.

Thank you to Professor Oleg Shpyrko for recruiting me to UC San Diego, for being a research mentor and sounding board, and most of all for allowing me the freedom

to explore teaching and encouraging me towards the career path I wanted, while working in his research group.

Thank you to Lecturer Michael Anderson for recognizing my interest in teaching and for guiding and mentoring me as I taught my first few college courses.

Thank you to Professors Shirley Meng, Sunil Sinha, and Andrea Tao for rounding out my dissertation committee.

Thank you to Suresh Narayanan, Zhang Jiang, Alec Sandy, and Mati Meron at the Advanced Photon Source for their patience helping me with experiments.

Thank you to Binhua Lin at the University of Chicago for her help with experiments, writing, and overall being my tiger mom and making sure I was well fed and rested during experiments.

Thank you to Yeling Dai for being a mentor and a friend in my graduate studies.

Thank you to Jacob Stanley for suffering through grad school alongside me, for our daily commiseration sessions, and I guess for helping me with research projects too...

Thank you to Sean You for help running experiments, and for being an easy target to make fun of.

Thank you to the rest of the Shpyrko group members for their help along the way.

Thank you to the administrative staff at UC San Diego for their work behind the scenes to keep the department functioning.

Thank you to all of my friends, past and present, for their invaluable support and kindness.

Thank you to Micha Goldflam for loving me through it all. The past few years haven't been easy for me, and I know that Micha has borne the brunt of it. I hope to repay him in kind now.

Last but not least, thank you to my cats Winston and Oliver for listening to me without complaining and providing stress relief.

Chapter 12, in part is currently being prepared for submission for publication of the material. Leandra S. Boucheron, Jacob T. Stanley, Yeling Dai, Siheng Sean You, Christopher T. Parzyck, Suresh Narayanan, Alec R. Sandy, Zhang Jiang, Mati Meron, Binhua Lin, and Oleg G. Shpyrko. "Jamming and ordering in quasi-2D self-assembled nanoparticle monolayers". The dissertation author was the primary investigator and author of this material.

VITA

2010	Bachelor of Science in Physics *with highest honors*, New Mexico Institute of Mining and Technology
2012	Master of Science in Physics, University of California, San Diego
2014 Summer	Summer Graduate Teaching Scholar, Center for Teaching Development, University of California, San Diego
2015	Doctor of Philosophy in Physics, University of California, San Diego

PUBLICATIONS

Leandra S. Boucheron, Jacob T. Stanley, Yeling Dai, Siheng Sean You, Christopher T. Parzyck, Suresh Narayanan, Alec R. Sandy, Zhang Jiang, Mati Meron, Binhua Lin, and Oleg G. Shpyrko. "Jamming and ordering in quasi-2D self-assembled nanoparticle monolayers", Manuscript in preparation.

Jacob Stanley, **Leandra Boucheron**, Binhua Lin, Mati Meron, and Oleg Shpyrko. "Spontaneous phase separation during self-assembly in bi-dispersed spherical iron oxide nanoparticle monolayers", *Applied Physics Letters*, **106**, 101602 (2015).

Jacob Stanley, Yeling Dai, **Leandra Boucheron**, Binhua Lin, Mati Meron, and Oleg Shpyrko. "Novel comparison of microscopy and diffraction techniques on the structure of iron oxide nanoparticle monolayers transferred by Langmuir-Schaefer method", *Review of Scientific Instruments*, **86**, 063704 (2015).

Andrej Singer, **Leandra Boucheron**, Sebastian H. Dietze, Katharine E. Jensen, David Vine, Ian McNulty, Eric R. Dufresne, Richard O. Prum, Simon G. J. Mochrie, and Oleg G. Shpyrko. "Domain morphology, boundaries, and topological defects in biophotonic gyroid nanostructures of butterfly wing scales", Manuscript submitted for publication.

J. W. Kim, A. Ulvestad, R. Harder, S. Manna, E. Fohtung, A. Singer, **L. Boucheron**, E. E. Fullerton, and O. G. Shpyrko. "Observation of x-ray radiation pressure on nanocrystals", Manuscript in preparation.

ABSTRACT OF THE DISSERTATION

X-Ray Studies of Diffusion Dynamics in Nano-Confined Geometries

by

Leandra Boucheron

Doctor of Philosophy in Physics

University of California, San Diego, 2015

Professor Oleg Shpyrko

Since their discovery in the late 1800s, x-rays have taken the stage as one of the most powerful research techniques for materials science. Their element-specific absorption has allowed for everyday applications in security and medical imaging, while their short wavelength has a tremendous ability to resolve materials on a molecular or even atomic level. In this dissertation, I will discuss basic properties of x-rays as well as how they are produced and detected. I will also present x-ray scattering and analysis techniques before moving onto a discussion of my research on diffusion in soft-matter systems. I provide a full alignment guide for a lab-based dynamic light scattering (DLS) goniometer system, which I used for some preliminary studies of

systems. I proceed to discuss diffusion on the nanoscale in quasi-1D (nanopores) and quasi-2D (liquid surface) systems. The latter of these systems was the main focus of my dissertation research. I utilized x-ray photon correlation spectroscopy (XPCS) to study the diffusion and interparticle dynamics of iron oxide nanoparticles at the air-water interface. Autocorrelation analysis revealed that these particles show signatures of a jammed system under lateral compression. I present these results as well as a description of their interpretation and importance in the main text.

Chapter 1

Introduction

X-rays are awesome. This dissertation represents my attempts to explain x-ray physics in the most accessible way possible and with the least amount of math involved. While a sizable amount of math is inevitable and even necessary, I am of the opinion that math can never provide an intuition. Without this deep conceptual understanding, it is nearly impossible for me to apply physical concepts to new situations and problems. I can plug in the correct numbers and equations, but this has never given me a feel for what is actually happening in the system. Where math is required and if feasible, I have tried to give detailed explanations or step-by-step derivations along with physical insights. In most cases, however, I admit defeat. The equations were derived by someone much smarter than myself and so I must simply state them without too much elaboration.

In recent years, x-rays have taken the stage as one of the most powerful techniques for probing materials on an atomic scale. Under most conditions, electromagnetic radiation is only useful for resolving objects on a lengthscale larger than its own wavelength. As a result, visible light microscopes are only able to magnify objects to a certain limited extent, on the order of hundreds of nanometers. For finer detailed examinations of nanostructures, an electron microscope may be necessary. Such microscopes make use of

the wavelike properties of electrons; their effective wavelength is shorter than that of light, making them better able to resolve material features. X-rays also have wavelengths many orders of magnitude smaller than those of visible light and are able to take measurements on the size scale of individual atoms. For this reason, they are becoming more and more popular as technological applications require scientific understanding on a smaller and smaller scale.

While many current microscopy techniques, such as atomic force microscopy (AFM) or scanning tunneling microscopy (STM) are also able to resolve individual atoms within a sample, x-rays are able to fill a niche where these standard techniques fail. As one example, microscopy can typically only be used to probe solid surfaces, while many cutting edge research projects require studies of liquids or liquid interfaces. X-rays are commonly used in grazing incidence configuration for observing such interfaces in surface sensitive applications *in situ*.

Additionally, microscopy is only able to provide images of relatively small areas of a sample. In order to gain *quantitative* information about a surface, a very large number of microscopic images will need to be collected and analyzed. It is incorrect to jump to the conclusion that the entire surface of a material can be characterized by the features seen in one or two images, especially if this surface has the potential to be highly inhomogeneous. X-rays, on the other hand, can simultaneously be scattered from all of the features on a macroscopic sample to produce a single image. This image can then be analyzed to provide *global statistical* information about material structure on a much larger scale than traditional microscopy allows for.

Many microscopy techniques can provide relatively good images of surfaces and surface features, but provide little if any information about the interior of materials. The high energy of x-rays grants them the ability to penetrate many materials in a non-invasive fashion; this means that materials which are opaque in the visible spectrum are often

nearly transparent when viewed with x-rays. This penetrative power allows x-rays to provide information about a bulk sample as a whole, both its interior and exterior.

Finally, third and fourth (x-ray free electron lasers) generation synchrotron sources afford the capability to produce coherent beams of x-rays with ever-increasing time resolution. This coherence enables the collection of phase-sensitive information on material samples. All of these properties combine to make x-rays a powerful and irreplaceable technique for past, current, and future scientific endeavors.

Chapter 2

X-Ray Production

2.1 Characterization of X-rays

X-rays are a form of electromagnetic radiation, travelling at the speed of light ($c \approx 2.99792 \cdot 10^8 \frac{\mathrm{m}}{\mathrm{s}}$) in vacuum. This speed is related to both their frequency and wavelength by the following relation:

$$c = \lambda\nu \tag{2.1}$$

where λ is the wavelength, typically expressed in meters (m), and ν is the frequency, expressed in Hertz (Hz), with $1\mathrm{Hz} = 1\mathrm{s}^{-1}$. The energy of a single packet of light, also known as a photon, can be found as:

$$E = \frac{hc}{\lambda} \tag{2.2}$$

while its momentum is:

$$p = \frac{h}{\lambda} \tag{2.3}$$

where h is known as Planck's constant ($h \approx 4.136 \cdot 10^{-15}$eV·s $\approx 6.626 \cdot 10^{-34}$J·s). These two values for h differ only in their respective units. While Joules, with $1\text{J} = 1\text{N} \cdot \text{m}$, is the typical measure of energy in the SI system, it is more convenient to deal with energies in terms of electron Volts (eV) for x-ray photons since each photon carries a relatively small amount of energy ($1\text{eV} = 1.602 \cdot 10^{-19}\text{J}$). One electron Volt is the unit of energy gained by a single electron when it is accelerated through a potential difference of one Volt; similarly a keV, or kiloelectron Volt is the energy gained from acceleration through a potential difference of 1000 Volts.

X-rays comprise the portion of the electromagnetic spectrum ranging from about 0.01nm to 10nm in wavelength. Typically, the units used for the measurement of wavelengths are nanometers. Traditionally, however, Ångströms were the common unit, with $1\text{Å} = 0.1\text{nm}$. These units are introduced here to avoid confusion with other references. This wavelength range corresponds to a frequency range from $3 \cdot 10^{16}$ to $3 \cdot 10^{19}$Hz, or an energy range from 0.124 to 124keV. While γ(gamma)-rays are depicted as the form of electromagnetic radiation above x-rays on the energy spectrum, what distinguishes the two is the process by which they are produced, not uniquely by their energies. X-rays are produced by electron processes – either by bound or unbound electrons – while γ-rays are produced by nuclear processes (those involving protons and neutrons) within an atom. γ-rays, especially those emitted by cosmic sources, extend to a much higher energy range than electron processes can achieve; however the two forms of radiation overlap substantially in the lower energy regime. Once they have left their respective sources, however, an x-ray and γ-ray of equal energies are indistinguishable and undergo the same physical processes including absorption, scatter, and diffraction. Thus, the development of x-ray techniques in this manuscript is equally valid when applied to γ-rays of similar energies. However, coherent and tunable sources of x-rays are much more common and so discussions will primarily involve x-rays.

As an aside, x-rays can be created by any charged particles, not just electrons. Protons and even molecular ions are also capable of producing this form of radiation; however because they are much more massive than electrons ($m_{\text{proton}} \approx 10^3 m_{\text{electron}}$), they require much more input energy in order to emit an equal amount of radiation. As a result, x-ray generation typically focuses on electrons as the source.

When two x-rays are incident on the same point in space, they behave much as waves. The overall wave at a point is determined by the superposition, or sum, of all incident waves. When two waves arrive at a point with the same phase (peaks and troughs aligned), they interfere constructively and the amplitude of the resultant wave is increased. Similarly, if they arrive exactly out of phase, they interfere destructively and the amplitude of the resultant wave is decreased. Two waves arriving with slightly different phases will result in a wave with an amplitude somewhere between these two extremes. In this manner, x-rays undergo interference and diffraction just as visible light waves.

Wave interference is the phenomenon responsible for the outcome of Young's famous double-slit experiment. When coherent (in-phase) light – such as light from a laser source – is incident upon a set of two slits separated by a small distance, waves travelling through each of these slits interfere with each other. This interference creates patterns of light and dark bands known as interference fringes. While the interference patterns from x-rays are not visible to the naked eye, they behave in just the same way.

2.2 X-ray Production by Bound Electrons

2.2.1 Auger Electrons

When an inner shell electron of an atom (an electron located close to the nucleus) is removed by collision with a photon or a fast-moving electron, it creates a vacancy in

the inner shell. For our purposes, "inner shell" electrons refers to all electrons with the exception of the valence band – the outermost shell of electrons readily available for chemical bonding. This vacancy leaves the atom in an unstable energy state. It is more energetically favorable for the inner orbitals, which are at a lower energy to be filled, with the vacancy transferred to an outer shell. Typically, an outer shell electron will fill this vacancy, but to do so, it must first release its excess energy. Electrons can release this energy in one of two ways, resulting in the production of either Auger electrons or x-rays. In the first method, the electron transfers its excess energy to an outer shell electron, providing this electron with an amount of energy greater than its binding energy, enough to escape from the host atom. This ejected electron is known as an Auger electron. Auger processes typically only occur for low-Z (low atomic number, where Z is the number of protons in the nucleus) elements due to their low binding energies. These low binding energies are a result of the overall smaller charge on the nucleus of an atom; inner shell electrons feel a smaller electric force and are thus less tightly bound to the nucleus. For elements with $Z < 31$ (preceding gallium on the periodic table), the emission of Auger electrons is more likely than the emission of x-rays, so their effects can be quite substantial. In fact, there are experimental techniques devoted to Auger spectroscopy to probe the chemical identity of materials.

2.2.2 Fluorescence

The second way in which an electron fills an inner orbital is by x-ray fluorescence. Fluorescence is a process in which an outer shell electron releases its excess energy in the form of an x-ray photon while transitioning to a lower energy (inner shell) state. The energy of this photon is dictated by the energy difference between the outer and inner shell orbitals. Thus, these "characteristic" x-rays vary widely in energy between atoms of different elements, and between different orbital levels in atoms of the same element.

As a result, characteristic radiation from materials of a known composition is often used for energy calibration of radiation detectors. In reverse, calibrated detectors can easily be used for analysis of unknown substances. The energy "signature" of specific elements can be seen in the energy spectrum emitted by the source as will be discussed shortly.

Binding energies of inner shell electrons typically increase as a function of atomic number. These inner electrons feel the largest electrical attraction from the nucleus, the total charge of which increases monotonically with atomic number. Outer shell electrons are somewhat "shielded" from this increase in central charge by the negatively charged inner shell electrons located between themselves and the nucleus. Since this screening effect is negligible for inner shell electrons, the higher the atomic number, the more tightly bound the inner electrons and thus the higher energy the characteristic x-rays produced by that element. Elements of lower atomic number produce "soft," or lower energy x-rays, while those of high atomic number produce "hard," or higher energy rays.

2.2.3 Other Processes

Certain nuclear decay processes can also lead indirectly to the production of characteristic radiation. In an event known as electron capture, an inner orbital electron enters the nucleus of the atom, combining with a proton to form an uncharged neutron. As a result, the chemical identity of the atom is changed due to the reduction in number of protons, though the net charge remains unchanged. This process leaves a vacancy in an inner shell electron orbital, which may subsequently be filled through the emission of characteristic x-rays.

Additionally, as mentioned earlier by the way of distinguishing between γ- and x-ray radiation, nuclear deexcitations typically result in the production of gamma rays. In some cases however, the excess energy of a nucleus may be dissipated by ejection of an inner shell electron in a process known as internal conversion. Again, this process

will also leave an inner shell vacancy which can lead to the emission of characteristic radiation.

As an electron transitions from an outer to an inner orbital, the emitted Auger electron or x-ray can leave the atom travelling in any direction. It has no "knowledge" of the initial process that removed the inner shell electron and thus exhibits no directional dependence (emitted isotropically, or equally in all directions). This distinction becomes important when dealing with processes such as x-ray scatter, which exhibit a strong directional dependence, often concentrated in the "forward" direction of the incident beam.

2.2.4 Nomenclature

To distinguish between different energies of x-rays produced by the same element, characteristic x-rays are named according to the principal quantum number (n) of initial and final orbital states of the electron that produced them. The $n = 1$ shell is known as the K shell, $n = 2$ as the L shell, and so on through M, N, and O shells. These shells are denoted by letters starting in the middle of the alphabet due to Charles Barkla, who observed characteristic radiation without understanding that the radiation came from electron transitions. He figured that higher energy radiation than the K and L lines he observed must exist, so reserved the letters A-J for these forms of radiation. When the production mechanism for x-rays was determined, it became clear that there are no higher energy lines exist, but the K-shell nomenclature remains for historical reasons.

A characteristic x-ray is distinguished first by the letter corresponding to the shell in which the vacancy was produced. A subscript Greek letter indicates the initial shell of the electron which drops its energy state to fill this vacancy. Thus, a subscript α indicates that the electron started out one shell higher than the vacancy, a subscript β two shells, and so forth. However, not all orbitals within the same shell are at the same energy level;

other factors, primarily the angular momentum carried by the orbital, affect the energies of specific electrons. To account for this, subscript numbers further separate energy levels in the initial state, with lower numbers indicating higher energy transitions. Not all transitions, however, are allowed; x-ray photons carry angular momentum, so a transition in which the angular momentum state of the electron remains the same is forbidden. Thus, the nomenclature procedure involving subscript numbers can be somewhat complicated. In practice, however, the energy differences between x-rays of a given type such as $K_{\alpha 1}$ and $K_{\alpha 2}$ are small enough that the energy resolution of an x-ray detector will not be able to distinguish them. In this case, photons of the two energies are grouped together in a single K_α peak known as a doublet. The energy for a doublet line is taken as the average of the energies of the two peaks, weighted by their intensities.

2.2.5 Spectra

The energy levels of electron orbitals in atoms of different elements are dependent on many factors. The wave equation governing the behavior of electron orbitals is not analytically solvable except in the case of hydrogen or hydrogen-like atoms (two-body problem). However, it is possible to determine empirical relations between the atomic number of an atom and the energy or frequency of its characteristic x-ray lines. Such relations are collectively known as Moseley's law. This law states that, for K_α and L_α, the lines of highest intensity in the K and L series are respectively:

$$E_{K_\alpha} = 10.2 \cdot (Z-1)^2 \text{eV} \tag{2.4}$$

$$E_{L_\alpha} = 1.89 \cdot (Z-7.4)^2 \text{eV} \tag{2.5}$$

where Z is the atomic number. While most values of x-ray line energies are determined by direct observation and measurement, Moseley's law can be useful for finding approximate energies when a table of values is not readily available.

X-ray spectra are typically shown as a graph of intensity (or log intensity) versus energy; characteristic x-rays appear as peaks within this spectrum. The dimensions of these peaks can be affected in a number of ways. First, the relative height of a peak in the spectrum indicates the relative rate at which x-rays of these energies are produced. These rates in turn depend on the probabilities of electrons transitioning between certain orbital levels in an atom. The most intense (highest) peak is typically caused by the production of K_α x-rays corresponding to a vacancy in the innermost (K) shell. Such a vacancy is more likely to be filled by an electron from the L shell than an electron from the M or other outer orbitals, causing this peak to be more intense than those corresponding to the K_β or K_γ lines. However, an orbital vacancy is often times not filled in a single step. Rather, emission of a K_α x-ray leaves a vacancy in the L-shell, which can further result in the emission of an L_α or L_β line and so forth. As a result, a cascade of radiation can be produced from the introduction of a single inner shell vacancy.

If a material is placed in between the x-ray source and detector to absorb some of the radiation, the height of all of the peaks will decrease, though each will not decrease by the same amount. This beam attenuation will be discussed further in the next chapter. In addition to peak height, characteristic x-ray lines exhibit a finite (but extremely narrow) energy width despite corresponding to specific energy transitions. The largest contribution to this width relates to the uncertainty principle. The uncertainty in the energies of specific orbitals leads to a spread in possible transition energies. Other physical factors, such as differing thermal energies of electrons or instrumental effects within the radiation detectors, can also lead to energy spread in a spectrum. Due to this line width, the height of a characteristic peak is generally not considered the best

measure of the beam properties. Instead, the integrated area under a peak is used to directly compare the intensities of lines of differing energies.

2.3 X-ray Production by Free Electrons

2.3.1 Bremsstrahlung and X-ray Spectra

Bremsstrahlung, a word meaning "braking radiation" in German, refers to the release of x-ray radiation by the deceleration of free electrons by an electric field while passing through a material. This form of radiation is sometimes also referred to as continuum radiation or "white" radiation. A fundamental tenant of electricity and magnetism maintains that accelerating charges produce radiation. Electrons oscillating along large antennas are responsible for the production of radio waves; much larger accelerations can provide the energy needed to emit radiation in the x-ray region of the electromagnetic spectrum. A stream of fast-moving electrons can be produced by heating a metal filament (often Tungsten) and by applying a large potential difference between this cathode and a target material known as the anode. When the electrons reach this anode, typically a high-density, high-Z material, they interact with the "sea" of positive and negative charges within the material. These electrical interactions cause forces which ultimately decelerate the electrons, causing them to emit radiation.

Some electrons may be stopped in a single interaction within the material while others may give up a fraction of their energy at a time, slowly stopping over a large number of interactions. Since the energies of these x-rays are not fixed or discretized, as in the case of characteristic radiation, bremsstrahlung creates a continuum of energies. In addition, since the interactions producing this form of radiation can occur at any position within the target material, bremsstrahlung photons exhibit no constant phase relationships with respect to each other. As a result, they comprise an incoherent, polychromatic beam.

The emission of this form of radiation is also highly anisotropic; it is concentrated mainly in the forward direction due to the directional dependence of the electron source and subsequent accelerations.

It is important to note however, that the majority $(> 98\%)$ of the energy lost from the initial electron beam is converted directly into heat rather than into x-rays. This phenomenon limits the intensity of x-rays produced by a bremsstrahlung source. At the molecular level, heat is simply related to the vibrations and motions of atoms and molecules. As a beam of electrons passes through a material, much of its energy will be converted directly into vibrations of the atomic lattice of that material. X-rays may also deposit energy into heat in this same manner; however, in a much smaller quantity due to their less frequent interactions. As we have discussed, electrons are able to behave both as waves and as particles. Similarly, these lattice vibrations may behave as either waves or as particles known as phonons. Phonons can both be emitted and absorbed by an electron or x-ray, though in most cases the rate of emission is far greater than the rate of absorption.

The largest fraction of bremsstrahlung x-rays are produced at low energies; the probability of interaction of an electron within a material increases as its energy decreases. The number of x-rays produced therefore decreases as a function of energy until a sharp cutoff at the maximum energy of the incident electrons (since this is the largest amount of energy that can be utilized to produce a single x-ray photon). Electrons passing very close to the nucleus tend to convert all of their energy into radiation at once and thus contribute to the higher energy photons near the cutoff. In practice, the very low energy photons created in this way are susceptible to attenuation (absorption) and their number will be greatly reduced by passage through any material, including air. As a result, the bremsstrahlung spectrum typically peaks somewhere around $\frac{1}{2}$ of the maximum energy, and drops off for both higher and lower energies.

During the bombardment of a material with electrons to produce bremsstrahlung, there are no physical processes to prevent some of the electrons from colliding with inner shell electrons of the atoms. If these inner shell electrons receive enough energy to escape from their host atoms, they create vacancies which can be filled as described in the previous section on characteristic x-rays. Thus, an energy spectrum from a bremsstrahlung source with a sufficiently high energy contains not just the bremsstrahlung background, but also a set of sharp characteristic peaks superimposed on top. These characteristic peaks are often several of orders magnitude more intense than the surrounding background. As the energy of the bremsstrahlung source is increased, the intensities of the characteristic x-ray lines increase, but their locations do not change since the energies of these peaks are a function only of the target material. Additionally, the height of the bremsstrahlung background relative to the peaks depends on the position of the detector. A detector facing the electron source head-on will see the largest background due to the strong directionality of bremsstrahlung. If, instead, the detector is placed at the same distance, but at a fixed non-zero angle relative to the incoming electron beam, it will see roughly the same amount of characteristic radiation while the bremsstrahlung background will be greatly reduced.

Bremsstrahlung was used as the primary source of x-ray radiation for many years. In conventional x-ray tubes, electrons are accelerated through vacuum by an electric field before colliding with a target anode in which the radiation is produced. Due to the extreme heat load of this process ($> 98\%$ of the initial energy), many early designs that could not maintain a fast enough cooling rate also incorporated a mechanism for rotating the anode. This rotation allowed the target beam to constantly be in contact with a new region on the anode. As a result, the cooling system was better able to dissipate the heat load before the same region was struck again by the beam.

For certain applications, such as medical x-rays, the shape of the x-ray spectrum

is not of great importance. Only an average transmission of x-rays through the body is needed to observe bone structure, independent of energy. As a result, bremsstrahlung is sufficient for many such applications. Many other scientific applications, however, are energy-specific. In these cases, a single energy peak of x-rays may be needed. Such a monochromatic beam can mostly be achieved through filtering or diffraction, as discussed in a later chapter on material interactions.

2.3.2 Synchrotron Sources

Introduction to Synchrotrons

In synchrotron sources, x-rays are also produced by the acceleration of free electrons, but these accelerations are caused by a magnetic field. Protons may also be accelerated to produce radiation, but due to their large mass as compared to electrons, using them as a source of radiation results in a $\sim 10^{13}$-fold reduction in beam intensity. Synchrotron sources are able to provide at least 5 orders of magnitude more flux and 10 orders of magnitude higher brightness than traditional x-ray tubes and other conventional sources. In synchrotron facilities, electrons are accelerated by magnetic fields as opposed to electrical interactions in materials, as is the case for bremsstrahlung. As a charged particle passes through a magnetic field, it experiences a force perpendicular to its motion, pushing it into a curved trajectory. Under certain conditions, this trajectory may be made circular. The magnetic force on a charged particle is given by the Lorentz force law:

$$F = q|\vec{v} \times \vec{B}| = qvB\sin(\theta) = qvB \tag{2.6}$$

where q is the charge, v is the velocity, B is the magnetic field, and $\theta = 90^\circ$ for circular motion (velocity and magnetic force kept exactly perpendicular at all times). The centripetal acceleration is given by:

$$a = \frac{v^2}{r} \tag{2.7}$$

as you may recall from basic mechanics, in which r is the radius of rotation. Uniform circular motion requires that:

$$F = ma = \frac{mv^2}{R_c} = qvB \tag{2.8}$$

where R_c is the radius of orbit, known as the cyclotron radius:

$$R_c = \frac{mv}{qB} \tag{2.9}$$

A cyclotron is a type of particle accelerator where the particles accelerate in a spiarl, and so the radius is constantly increasing as the speed increases. In a synchrotron, the speed does not change, so R_c is kept fixed. Since R_c depends on the *classical* momentum, it does not change by much as $v \to c$, for $v \sim c$.

Components of a Synchrotron Facility

Electron Gun and Initial Acceleration The process begins at a pulsed electron source, which is used to create equally spaced bunches of $> 10^{10}$ electrons each. This source normally takes the form of a "thermionic gun," which heats a cathode material to the point of electron emission. A linear accelerator then accelerates these electrons up to an energy on the order of a few hundred MeV apiece, followed by a booster accelerator which increases their final energy to 2-8GeV before they are injected into the main storage ring. This acceleration process can occur in a couple of different types of equipment. The first, known as a microtron, has a variable magnetic field which is continuously increased; as particles are accelerated to higher energies, the radius of their orbit grows according to equation 2.9 and their trajectory takes the shape of a spiral. Electrons of

differing energies simultaneously exist within a single magnetic field (though in spatially different locations). The disadvantage to this configuration is that it requires a large magnetized volume proportional to E^2, where E is the desired energy. This requirement limits practicality and as a result, microtrons are only able to produce electrons with energies on the order of hundreds of MeV.

Booster Synchrotron Most synchrotron facilities use a booster synchrotron in place of a microtron. Booster synchrotrons are often shaped like a racetrack; they have semicircular ends with straight sections connecting the two. As electrons travel through the straight sections, they are accelerated by an electromagnetic field, just as in a linear accelerator. When the electrons reach the semicircular segments, the magnetic field is adjusted to match the condition for circular motion as derived in equation 2.9 above. Thus with appropriate changes in accelerating electric and magnetic fields, electrons can circulate around the booster ring hundreds of times and be accelerated to the desired energy before being injected into the storage ring. This fixed trajectory path minimizes the necessary magnetic field volume and allows for much higher final energies than achievable by a microtron. However, a booster synchrotron only allows one energy of electrons to circulate at a time and thus the maximum pulse length is set by the time it takes an electron bunch to circulate the booster ring.

Injection System After being accelerated to the desired energy, electrons must be "injected" into the storage ring. The injection system is extremely important to the operation of a synchrotron facility because electrons are continuously circulated around the storage ring, and the injection system must accurately synchronize to the passage of electron bunches. Fast switching magnets as well as magnets known as 'kicker' magnets and 'septum' magnets are thus necessary. The injection system represents a substantial portion of the costs of construction of a synchrotron, on the order of $10-40\%$.

Storage Ring After leaving the booster ring, bunches of electrons enter the main storage ring, which consists of many straight sections connected together by arced sections. The radiation generated at such facilities is typically called "synchrotron radiation" despite being produced in the storage ring, not the booster synchrotron itself. This is because in the synchrotron ring, the beam energy is ramped up, which is not good for experiments requiring a steady beam. An electron bunch passing a fixed point in a storage ring lasts on the order of 10 picoseconds, while the time between bunches is on the order of 10 nanoseconds. The electron bunch itself ranges between 0.5 and 5cm in length.

A storage ring recirculates the beam as many times as possible; the lifetime of a synchrotron beam is on the order of 5 to 100 hours. This finite beam lifetime is due to an exponential decay in the storage ring current. The current decreases as electrons are lost due to scattering by remnant gas molecules, intrabeam scattering (known as "Touscheck scattering"), magnetic inhomogeneities in the guiding magnets, and a few other less common effects. The entire system is kept under ultra high vacuum ($< 10^{-9}$ Torr, or $< 10^{-12}$ atmospheres pressure) to minimize collisions of electrons with air molecules. Even still, collisions with residual gases represents the largest component of beam loss. Hard scattering from air molecules can cause electrons to completely leave the main beam, while softer scattering simply broadens the beam. However, broadening effects degrade the beam quality and also contribute to a decrease in beam lifetime.

Design of a vacuum system for synchrotron facilities is made especially important by the phenomenon of photon-stimulated desorption. Photons of radiation emitted from the electron beam are able to excite molecules on exposed surfaces, thereby desorbing gases that remain despite careful cleaning and baking procedures to minimize gas content on the surfaces of the hardware components of the storage ring.

Modes of Operation There are two main modes of operation to account for the loss of beam current over time. In the normal mode of operation, electrons are injected approximately every $\frac{T}{2}$ hours, where T is the beam lifetime. At this point, approximately 40% of the electrons from the initial beam have been scattered. The advantages to the normal mode are that the current decay function is very smooth, and that the electron injection system does not have to be constantly running so there are less interference effects with the injector magnets and the electrons traversing the storage ring. However, a decreasing beam current results on variable heat loads on the ring components and a reduced average photon flux. As a result, another common mode of operation, known as "top-up" mode injects electrons approximately every $\frac{T}{1000}$ hours. This operation requires more frequent use of the injection system (and hence requires a high injector efficiency) and complicates the beam current as a function of time. However, it maximizes photon flux which is an important characteristic for many experiments which specifically make use of synchrotron facilities for their high brightness.

RF Cavity Electrons in the ideal, closed trajectory around a storage ring are those which are said to have a "synchronous energy" E_0 given by:

$$E_0[\text{GeV}] = 0.3B[\text{T}]R[\text{m}] \tag{2.10}$$

where B is the dipole magnet strength, R is the radius of curvature of the ring, and the brackets [] refer to the units of the variables which should be plugged into the equation. Since electrons lose energy to radiation as they undergo centripetal acceleration around the ring, this energy must be replaced using a radiofrequency cavity (typically located in one of the straight sections of the storage ring) to maintain a steady beam. This RF cavity also acts to pull electron bunches back together by providing a lower voltage to the first (fastest) electrons to reach the cavity and a higher voltage to the slower electrons.

The energy lost solely to the magnets keeping the electrons in a circular orbit is given by:

$$\Delta E[\text{keV}] = 88.4 \frac{E_0^4[\text{GeV}]}{R[\text{m}]} \tag{2.11}$$

per revolution. If more than a critical amount of energy is radiated or otherwise dissipated, an electron will no longer be in a stable orbit and will fall out of the beam, since it will be out of phase with respect to the accelerating voltage provided by the RF cavity. Synchrotron facilities are designed to minimize these losses, and the RF cavities replenish the energy lost to synchrotron radiation as well as to intrabeam scattering effects.

Magnet Systems Magnets are arguably the most critical component of a storage ring, since they direct the beam along its intended orbit. Magnet systems undergo extensive design and testing to ensure that they generate precise fields. The complete arrangement of various sets of electromagnets around the ring comprises what is known as the lattice structure.

Electrons of only a very specific energy are able to maintain a constant closed orbit around a storage ring. Slightly off-energy electrons exhibit trajectories that oscillate about the ideal orbit; these deviations are known as betatron oscillations. Dipole ("bending") magnets are the main component used to direct the electron along the circular path of the storage ring. They provide a constant magnetic field across the entire spatial extent of the beam. However, since the electron beams are not ideal and have finite spatial and angular spread, dipole magnets alone are insufficient to maintain a steady beam current.

As a result, quadrupole ("focusing/defocusing") magnets in the straight sections of the storage ring are used to provide a focusing or restoring force to electrons that deviate too much from the orbital path. They act the job of transparent lenses for visible light. The strength of the magnetic field from a quadrupole cancels in the center of the beam and increases linearly as a function of distance from the ideal electron path.

By nature of these fields, quadrupole magnets which focus the beam in the horizontal direction by deflecting electrons back towards the center actually act to *defocus* the beam vertically by deflecting electrons away from the central plane in the vertical direction. Strong focusing systems therefore must include alternating sets of horizontally and vertically focusing quadrupole magnets in specific configurations in order to strongly focus the beam.

Just as passing through a prism separates visible light into its component colors, focusing/defocusing magnets have an inherent energy dependence to their restoring forces. Sextupole ("steering") magnets correct the resulting chromatic aberrations with magnetic fields which vary as the square of the distance from the ideal beam center.

In certain cases, when energy is added to a system of circulating electrons, instabilities can develop from forced oscillations in the plane perpendicular to the direction of motion. A process known as Landau damping can instead convert this energy into increasing the electron bunch size, thereby eliminating potential instabilities. Octupole magnets can be used in a storage ring to provide Landau damping forces.

Smaller dipole magnets known as dipole correctors are operated at reduced field strengths in order to make final corrections to electron bunch trajectories. Static correctors are used to fix known trajectory problems in an otherwise closed orbit. On the other hand, variable field dipoles can be implemented as dynamical correctors. Many modern synchrotron facilities actively monitor beam position and quality and can use dynamic correctors in a feedback control system.

Beam Properties When electrons are first injected into the storage ring, they occupy only a very small spatial extent. As they travel through the storage ring magnetic system and undergo various scattering processes, the energies of the electrons can change slightly, forcing them outside the initial volume they were made to occupy. Consequently, the

lattice structure of the ring's magnetic fields dictate the range of trajectories the electrons are allowed to occupy. All possible locations of an electron fall into an ellipse-shaped region of area:

$$A = \pi\varepsilon_{xy} \tag{2.12}$$

where ε_{xy} is a quantity known as beam emittance. This ellipse of allowed electron states can change its shape and orientation at various points around the ring. As electrons traverse the ring through more and more cycles, the beam tends to expand until electrons occupy the entire allowed area (electrons outside this area do not meet the criterion necessary to continue to circulate in the beam and will thereby be lost). This area may also be known as the "phase space" available to the electrons.

Sources of Radiation

Bending Magnets Each of the arced sections in a synchrotron contains a set of bending magnets, which are designed to deflect the electrons in the direction of the next straight section. This inward acceleration of the electrons produces a continuous spectrum of x-rays. Because the strength of the magnetic field must be fixed in order to deflect the beam into the straight section, the radiation produced by a bending magnet is not tunable in energy, and is emitted tangentially to all points on the arc (is not fixed in a single direction). Bending magnet radiation was the first form of synchrotron radiation discovered in circular accelerators used for particle physics experiments. The 2nd generation of dedicated synchrotron sources consisted primarily of bending magnets. At this stage in the development of synchrotron facilities, electrons were also injected into the main ring before they were at their full energy. As a result, the central ring was also required to accelerate the electrons to their final energy.

Wigglers Contained within the straight sections of synchrotrons are one of two different sets of magnets known as insertion devices. These insertion devices (called wigglers or undulators) have the ability to increase the intensity of the resultant x-ray beam by a factor of $\sim 10^{12}$ as compared to bending magnets. Both types of insertion devices consist of periodic sets of magnets arranged one after another, with opposing poles next to each other. In this manner, any deflection of the x-ray beam caused by one magnet will be corrected by the next, since their magnetic fields point in opposite directions. While most insertion devices are traditionally made using permanent magnets, more recent designs have incorporated the use of electromagnets.

Wigglers operate at high field strengths, producing a continuous spectrum of radiation similar to bending magnets, but with greater energies due to larger accelerations of the electrons and greater collimation (forward directionality of the beam). This continuous spectrum arises because the magnetic field strength is great enough to cause relativistic motion and distort the periodic motion the electrons would otherwise take. The deflections of electrons due to the magnetic fields are larger than the emission angle of synchrotron radiation produced by wigglers. Despite a similar continuous energy spectrum to their bending magnet counterparts, wigglers have several advantages. First of all, every "wiggle," produced by a single magnetic period, produces as many photons as a single bending magnet. Additionally, since the primary purpose of a bending magnet is to direct the beam, *not* to produce radiation, its magnetic field is dictated by electron orbit requirements. On the other hand, the magnetic field in a wiggler can be chosen to produce a specific energy spectrum.

A wavelength shifter is a wiggler containing only a few sets of magnetic dipoles. These magnets have higher field strengths in order to produce a low intensity beam of harder radiation as opposed to a high intensity beam of soft radiation produced in a large array of magnets with small field strengths. In many cases, a wavelength shifter may

consist of only three magnetic dipoles: one central high field strength dipole surrounded by two weaker magnetic fields to keep the electron moving along its original trajectory.

The properties of both bending magnets and wigglers can be expressed by a single quantity known as the critical energy. Half of the continuum beam power is radiated below this energy, while half is radiated above. Note that this definition is dependent on *power*, not number of photons. The critical energy can be found as:

$$E_c[\text{keV}] = 0.66B[\text{T}]E_0^2[\text{GeV}] \tag{2.13}$$

or equivalently:

$$\lambda_c[\text{Å}] = \frac{18.6}{B[\text{T}]E_0^2[\text{GeV}]} \tag{2.14}$$

The total power of radiation emitted by a wiggler can be described as:

$$P[\text{W}] = 632.8E_0^2[\text{GeV}]B^2[\text{T}]L[\text{m}]I_b[\text{A}] \tag{2.15}$$

where L is the total length of the wiggler magnets and I_b is the beam current.

Undulators Undulators are similar to wigglers except that they operate at reduced field strength and reduced gap distance between magnetic poles. In this manner, they accelerate electrons in tighter sinusoidal paths (the electron deflection is on the order of the emission angle of synchrotron radiation), creating a discrete spectrum. Electrons passing through an insertion device are loosely bunched to the extent that they are out of phase with respect to each other. As a result, the radiation produced by different electrons in a single bunch can be out of phase and combine incoherently. However, the undulator period (the distance between opposing magnetic poles) is designed such that while the electrons traverse one period, the photons produced by these electrons advance by one

full wavelength ahead of the electron (since photons travel at the speed of light, while the electrons travel at a slightly lesser speed). As a result, photons produced by the same electron at different points in its trajectory are in phase with respect to each other and add coherently. This coherence results in intensity peaks at discrete energies and their odd harmonics. When an observer looks back along the trajectory of an electron, he sees the sinusoidal electric field created by the radiation in phase with the motion of the electron which created this radiation. On axis, therefore, only odd harmonics can be observed in the frequency spectrum, while remnant even harmonics may affect the radiation seen at slightly off-axis points.

As electrons travel through a straight section of an insertion device, their emitted radiation builds up in the forward direction. Thus, wigglers and undulators are able to produce beams which are much stronger and more unidirectional than those produced by bending magnets. The properties of both wiggler and undulator radiation depend upon the number of magnetic poles along their length and the distance between these poles.

Wigglers and undulators can be distinguished by a quantity known as the deflection parameter K, which is given by:

$$K = 0.934 B_0[\mathrm{T}]\lambda_m[\mathrm{cm}] \tag{2.16}$$

in which B_0 is the magnetic field strength and λ_m is the length of one period of magnetic poles. For a wiggler, radiation is swept back and forth across a wide angle during a period of electron oscillation, and the deflection parameter $K \gg 1$. $K \leq 1$ in the case of an undulator. The peak angular deflection can be given as $\frac{K}{\gamma}$, where $\gamma = \frac{1}{\sqrt{1-\frac{v^2}{c^2}}}$ is the relativistic correction factor. Therefore, when $K < 1$, the electron trajectory overlaps with the emitted radiation, reinforcing coherent addition of radiation. Occasionally, an insertion device may be designed which shows strong interference effects only at low photon energies, and acts more like a wiggler as photon energy is increased. Such a

device is known as a *wundulator*.

The longest wavelength radiation produced by an undulator (its fundamental wavelength) is given by:

$$\lambda_1[\text{Å}] = \frac{13.1\lambda_{\text{und}}[\text{cm}]\left(1+\frac{K^2}{2}\right)}{E_0^2[\text{GeV}]} \tag{2.17}$$

where λ_{und} is the undulator magnetic period length, and E_0 is the beam energy. All higher harmonics are given by:

$$\lambda_n = \frac{\lambda_1}{n} \tag{2.18}$$

though these harmonics only contribute significantly to the overall undulator radiation for odd values of n. The fundamental energy can also be found as:

$$\varepsilon_1[\text{keV}] = \frac{0.95E_0^2[\text{GeV}]}{\left(1+\frac{K^2}{2}\right)\lambda_{\text{und}}[\text{cm}]} \tag{2.19}$$

Looking along the plane of the storage ring, electrons appear to oscillate back and forth while they travel through an undulator or wiggler much like charge oscillations in a dipole antenna. As a result, this in-plane light is linearly polarized. Off-axis, the radiation may be elliptically polarized. For studies requiring high-intensity circularly or elliptically polarized light, a certain class of insertion device, such as a helical undulator, may be required.

Beam Coherence

One of the main advantages to the use of undulator radiation is its high degree of both spatial and temporal coherence. While bremsstrahlung and characteristic radiation may be used to observe material properties by means of x-ray scatter, no phase

information can be deduced since the beams are initially composed of waves of arbitrary phases. In synchrotron sources, however, the coherence can help provide much more information about a material and its scattering properties. The coherence dimensions of a beam depend on both its degree of monochromaticity and on its angular spread due to the finite source size. Within the coherence lengths, the beam is able to interfere while maintaining proper phase relationships, while at greater distances, interference effects may be somewhat limited. The longitudinal coherence length (along the direction of propagation of the beam) is given by:

$$l_{\text{long}} = \frac{1}{2}\frac{\lambda^2}{\Delta\lambda} \tag{2.20}$$

where λ is the wavelength and $\Delta\lambda$ is the maximum difference in wavelength between two waves in the (assumed monochromatic) beam. Similarly, the transverse coherence length (perpendicular to the direction of propagation) is given by:

$$l_{\text{trans}} = \frac{1}{2}\frac{\lambda}{\Delta\theta} = \frac{\lambda}{2}\frac{h}{D} \tag{2.21}$$

where $\Delta\theta$, the angular spread, can be approximated by $\frac{D}{h}$, where h is the source height (the maximum distance apart that two waves can be formed) and D is the distance over which the wave propagates before being measured. At a synchrotron source, the longitudinal and transverse coherence lengths are typically on the order of 5μm and 10μm, respectively. The beam width is generally around 100μm.

2.3.3 Energy Recovery Linac (ERL)

As electrons in a synchrotron facility travel through the storage ring multiple times, they begin to spread out, to a point where the RF cavity and magnets are no longer able to completely correct their trajectories. For this reason, many synchrotron beams

are wider and less intense than would otherwise be desirable. In the ideal situation, each bunch of electrons would only circulate through the ring once, providing a much more focused radiation beam. However, the amount of energy required to accelerate these electrons is prohibitive, both in cost and logistics. In the energy recovery linac design, electrons are decelerated after one cycle around the main ring. As they are decelerated, the majority of their energy is stored in electromagnetic fields, which can then be used to accelerate a new bunch of electrons. Thus, the additional energy input at each cycle is much smaller than the total energy of the beam at any given point.

2.3.4 X-ray Free Electron Laser (X-FEL)

A new generation of x-ray sources known as free electron lasers has recently begun operating. The principle behind their operation is very similar to that of undulators used in the straight sections of current synchrotron sources. However, an X-FEL is based fully on a linear accelerator design, rather than the circular design of synchrotrons containing many insertion devices. In an X-FEL, the periodic magnet structure is optimized such that electron oscillations reinforce each other and add together constructively. Electrons are bunched into thin, pancake-shaped groups and are thus in phase with respect to each other. As a result, in addition to the coherent addition of radiation from different trajectories of the same electron, radiation coherently adds between different electrons. Bunch spacing is also determined such that multiple bunches have the same phase. This process, known as self-amplified stimulated emission (SASE) leads to further bunching of the electrons, creating pointlike charges which are able to emit radiation with a much greater degree of coherence. At the end of the SASE process, the beam is saturated by the time it reaches the end of the undulator. Further development of X-FELs is important due to their high spectral brightness and shorter pulse length (on the order of tens of femtoseconds).

There are two main varieties of free electron lasers known as oscillator and high gain lasers. High gain lasers use only a long undulator device, as described in the previous paragraph. On the other hand, oscillators trap emitted photons in an optical cavity surrounded by two mirrors, just as in a traditional laser. These photons interfere with subsequently arriving electron bunches to produce the desired bunching effect. The optical cavity approach does not work, however, in the x-ray regime since optical cavities require reflection at nearly normal incidence.

2.3.5 Cosmic Sources

Synchrotron radiation has also been found to occur naturally as a portion of the electromagnetic radiation generated by cosmic objects such as stars, nebulae, and active galaxies. Magnetic field lines produced by these objects create effective traps, along which relativistic electrons may be confined to move. As these electrons orbit around the field lines, they emit polarized synchrotron radiation by much the same process as electrons within manmade synchrotron sources. This synchrotron radiation can be distinguished from other radiation produced by cosmic bodies due to both its high degree of polarization and its energy signature. While the majority of the radiation emitted from a cosmic source follows a blackbody spectrum, synchrotron radiation is directly related to the energies of the electrons trapped in the magnetic fields.

2.3.6 Scotch Tape

Tribocharging is a process by which a material can become charged by coming into contact with and then separating from a second material. This charging is often due to frictional forces, as in the example of shuffling wool socks against a carpet. When tribocharging occurs as adhesive tape is removed from a roll, it typically discharges

before too large of a total charge can be accumulated. This phenomenon occurs because of the dielectric breakdown of air and the surrounding media, providing an easy means of charge transport. However, when the tape is placed in vacuum, higher charges are able to accumulate. When stick-and-slip discharge occurs, it can provide enough energy to produce radiation in the visible spectrum, in addition to photons of x-ray wavelengths.

Chapter 3

X-ray Interactions with Materials

3.1 Diffraction in Crystal Lattices

Diffraction of an x-ray beam is a result of the combined effects of coherent scatter and subsequent wave interference. Diffraction occurs within crystal lattices, which are well-arranged periodic arrays of atoms. When x-rays diffract from such a lattice they behave according to a principal known as Bragg's law. This law states that for constructive interference of waves diffracted between different planes of atoms:

$$m\lambda = 2d\sin(\theta) \tag{3.1}$$

where m is an integer known as the order, λ is the wavelength of the light, d is the distance between lattice planes, and θ is the angle between the incoming ray and the plane (half the angle between the incoming and outgoing rays). This condition comes from the pathlength difference between two waves reflecting from adjacent atomic layers in the material. This length difference must be equivalent to an integral (m) number of wavelengths for the two waves to emerge in phase and constructively interfere.

It is not necessarily clear why waves of wavelengths *close* to the Bragg condition

would not also contribute to the diffraction pattern. After all, such waves would exit from two adjacent layers with very similar phases and be able to interfere in a mostly constructive manner. However, x-ray waves entering a crystal scatter from not just one or two planes, but many thousands of planes. A small phase shift is introduced at each plane the x-ray reflects from, and the net effect is that while two adjacent layers interfere constructively, there are two adjacent layers deeper in the crystal that will exactly cancel their contributions. As a result, only waves exactly matching the Bragg condition will exit the crystal completely coherently. However, it may be argued that for very thin crystals, the number of atomic planes is not great enough for certain wavelengths to completely destructively interfere. In this case, x-rays with wavelengths slightly above or below the Bragg condition may also diffract from the crystal. In addition, stresses, strains, or imperfections within the crystal material can result in slight changes in the interplanar distances, affecting the Bragg condition. Both of these factors can result in "diffraction broadening" and a less monochromatic beam than is otherwise achievable by an ideal crystal lattice.

If the plane spacing d and incident angle λ are kept fixed, the Bragg condition will be met for a specific wavelength for order $m = 1$. In addition, the condition will also be satisfied for shorter wavelengths with increasing values of m. These waves are known as the higher harmonics; a wave diffracted to a specific angle will thus be composed of many different energy peaks. A single crystal plane of atoms, such as the surface layer, only scatters a portion of the incident beam; the rest of the beam travels further into the material, where it may diffract from subsequent planes. As a result, if the incident angle θ is kept fixed, and given order $m = 1$, the Bragg condition will be met for a specific wavelength for plane spacing d. However, the condition will also be met for shorter wavelengths with increasing integral multiples of d, corresponding to deeper layers of the crystal plane. This example shows the equivalence between the second

order Bragg condition for the first crystal layer and the first order Bragg condition for the second crystal layer (and so forth with integer multiples). Since the resultant beam is always a superposition of the diffracted beams from all crystal layers, each layer may be considered separately. This fact allows a crystal to be thought of, not just as a set of planes spaced by a distance d, but also as a set of planes spaced by distance $2d$ or $3d$ (skipping over the intermediate layers).

Since a layer of atoms within a crystal only scatters a small fraction of the photons with which it interacts, a diffracted x-ray beam is always much weaker than the incident beam. While the net result of x-ray diffraction is similar to reflection of visible light from a mirrored surface, the two processes differ in some fundamental ways. As mentioned above, x-ray diffraction is much less efficient than reflection. Additionally, strong diffraction only occurs for certain incident and exit angles, as opposed to visible light which is reflected to all angles. Finally, the diffracted beam observed at a point is composed of a superposition of beams scattered from many different atomic layers within a crystal. Virtually all of the energy of visible light incident on a mirror is reflected by the surface layers; the beam does not propagate into the mirror beyond the skin depth (due to the exclusion of electric fields from the interior of conductors).

Electromagnetic rays with wavelengths longer than the lengthscale that is being observed are unable to resolve features adequately; such systems are said to be diffraction limited. As a result, visible light with wavelengths on the order of 400 to 750nm cannot be used to image crystal planes with spacing on the order of 0.15 to 0.4nm. The diffraction limit can be found from Bragg's law; the maximum wavelength that can be used to image a system can be found by maximizing $\sin(\theta) = 1$:

$$m\lambda < 2d \tag{3.2}$$

For first order diffraction, $m = 1$ and:

$$\lambda < 2d \tag{3.3}$$

represents the diffraction limit. A crystal lattice is unable to diffract radiation with wavelengths larger than this limit. While all smaller wavelengths are able to be diffracted by the lattice, as λ decreases, the value of $\sin(\theta)$ must also decrease, since the crystal spacing d is constant. Waves that scatter to small angles are difficult to accurately detect and measure. As a result, a given material is only able to diffract x-rays within a narrow energy range.

For interatomic spacings between 0.15 and 0.4nm, the diffraction limit corresponds to x-rays between 1.5 and 4.1keV in energy. Photons of these or higher energies are able to diffract from the crystal lattice, allowing for atomic-scale resolutions. The similarity between atomic distances and the wavelengths of x-rays explains their prominent role in discovering molecular shapes and their continued use in a wide range of applications involving measurements on the nanometer or atomic scale.

3.2 Interaction Mechanisms in Materials

3.2.1 No Interaction

It is important to understand that many x-rays pass through a material with no interactions. In this case, their energies remain completely unchanged, as if the target material did not exist.

3.2.2 Heat

An x-ray passing through a material may induce vibrations in its atomic lattice, with the net effect of producing phonons and heating the material.

3.2.3 Coherent (Rayleigh) Scatter

When an x-ray photon interacts *slightly* with bound electrons by inducing oscillations in the local electrical fields, this interaction can deflect the x-ray to a small angle relative to its initial trajectory while transferring virtually no energy to the material. In addition, since the same photon is emitted from the atom, it maintains its same phase relationship, hence leading to the term coherent radiation. This process typically occurs for low-energy photons and can be detected at small angles to the incident beam. The shift in direction of the incoming photon without a transfer of energy results in an elastic collision between the photon and an orbital electron.

X-rays are not coherently scattered by the nucleus because the intensity of coherent scattering is inversely proportional to the square of the mass of the scatterer. Thus, the nucleus can not oscillate to any appreciable extent as a result of interactions with passing electrons.

3.2.4 Photoelectric Absorption

A head-on collision between an x-ray photon and an inner orbital electron in the material can result in a deposition of all of the photon's energy into the electron, ejecting it from the host atom. This process may only occur if the initial x-ray photon has an energy greater than the binding energy of the electron with which it collides. At this point, the electron becomes known as a photoelectron. The photoelectron escapes with a kinetic energy equal to the difference between the initial photon and its binding energy. The photon completely disappears during this transfer. This process is an instance of the photoelectric effect for x-rays, and dominates material interactions at high-Z and low energies. When an inner shell electron is removed by photoelectric absorption, it creates a vacancy which may result in the production of further characteristic x-rays.

The energy of this radiation, however, is limited to less than the energy of the incident photon, since some of this initial energy was converted into kinetic energy of the escaped photoelectron.

3.2.5 Incoherent (Compton) Scatter

An x-ray may also interact *strongly* with an outer orbital electron, transferring enough energy to eject it from the host atom without completely annihilating itself. When these electrons are subjected to the electric field of the incident beam, they experience a force and subsequently begin to accelerate and oscillate about their initial position. Through these oscillations, they re-emit a photon of slightly lower energy than the incident photon (radiate as a dipole antenna). The Lorentz force law gives $\vec{a} = -\frac{e}{m}\vec{E}$; since the charge on an electron is negative, its oscillations are 180° out of phase with the incident electric field. As a result, the scattered wave reemitted by the electron is out of phase with respect to the initial wave. Because the phase relationship between the incident and emitted x-rays are lost, this process is known as incoherent scatter. The electron, known as a recoil electron, retains some of the excess energy from the incident wave as kinetic energy. The overall effect of this process is an inelastic collision, resulting in a partial energy transfer between the incident photon and the (initially bound) recoil electron. While Compton scatter does exhibit some directional dependence, scattered photons can be detected at almost any angle with respect to the incident beam. This process dominates interactions at both the low-Z and mid-energy ranges.

Compton scattered photons cannot take part in diffraction since they do not maintain a phase relationship with the incident wave, but the Compton process is an unavoidable side effect which darkens the background of diffraction patterns. What differentiates this process from photoelectric absorption is that electrons are ejected from the atom, but the x-ray is not completely absorbed in the process.

3.2.6 Pair Production

At high energies ($>$ 1MeV, twice the rest mass energy of an electron), a photon may interact with the nucleus of an atom, annihilating itself in the process and creating an electron-positron pair. Any excess energy from the initial photon above the rest masses of the electron and positron contributes to the kinetic energies of these particles. The pair of particles which is produced continues travelling through the material, where the positron typically recombines with an electron in fairly short order, resulting in the creation of a pair of photons known as annihilation photons.

3.2.7 Photodisintegration

Finally, x-rays of extremely high energies may lead to a phenomenon known as photodisintegration of an atom. In this process, an x-ray photon hits the nucleus of an atom, expelling one or more of its subatomic particles and altering the chemical identity of that atom.

3.3 Overall Attenuation

As some or all of the above interactions occur within a material, the incident radiation becomes exponentially attenuated. The fractional decrease in intensity is proportional to distance travelled by the beam:

$$\frac{dI}{I} = -\mu dt \tag{3.4}$$

where I is the beam intensity, dI is the differential change in beam intensity, dt is the differential thickness the beam travels through, and μ is the absorption coefficient for the material. Solving this equation gives:

$$I = I_0 e^{-\mu t} \tag{3.5}$$

where I_0 is the incident intensity, I is the intensity being measured, t is the total material thickness, and μ is, again, the absorption coefficient for the material. This coefficient is a function of both the chemical identity of the target material and the energy of the incident radiation; it is taken as a sum over all possible interactions listed above. While scattered light is not absorbed within the material, it is counted in the attenuation coefficient because it is not contained within the transmitted beam after passing through the material. In other words, a radiation detector must be placed at a different location to observe the scattered beam.

Since most absorption processes depend heavily on the number of electrons in a given volume, μ depends on the material density, ρ. As a rough approximation, μ is directly proportional to the product of Z^3 and λ^3, where Z is the atomic number of the target material and λ is the wavelength of the incident radiation. The value $\frac{\mu}{\rho}$, known as the mass absorption coefficient, is used more commonly than μ; this coefficient allows density-independent comparisons between absorption in different materials. Using this coefficient, the attenuation equation takes the form:

$$I = I_0 e^{-\left(\frac{\mu}{\rho}\right)\rho t} \tag{3.6}$$

Each element has a unique mass attenuation coefficient; the coefficient of a compound or mixture can be determined simply by a weighted average of the coefficients for its individual component elements. By the same exponential attenuation relation, the mean free path that a photon will travel through a material is found as:

$$\lambda_{\text{mfp}} = \frac{1}{\mu} \tag{3.7}$$

In general, x-rays are more easily attenuated at lower energies; high energy "hard" x-rays are able to penetrate materials to much greater depths. However, the specific absorption spectrum of a material contains a few regions contrary this trend. As the energy of an incident beam is increased, there will be energies at which the absorption will jump suddenly to a higher value. This phenomenon can be understood in terms of the binding energies of electrons in the material. Right below a binding energy, an x-ray photon will be unable to remove an inner shell electron. Thus, a material will be less efficient at absorbing an x-ray beam at this energy as it will be just above this energy, when a new absorption mechanism is introduced and the photon has the ability to interact with many more electrons. Thus, the absorption spectrum of a material is shaped roughly like an exponential decay as a function of energy with abrupt spikes corresponding to the "K-edge" (L, M, N, etc. depending on the orbital) of the material. These spikes coincide with the binding energies of electrons in corresponding orbitals of the atom. Since the binding energy of an electron must be larger than the energy difference between any two orbital levels within an atom (which dictates the energy of a characteristic x-ray), these edges occur at slightly higher energies than their counterpart K, L, etc. x-rays. Because of the exponential nature of x-ray transmission, K-edge absorption can lead to a quite drastic decrease in transmitted intensity.

3.4 Energy Selection

3.4.1 Windows

There are many instances in which an x-ray beam needs to be transmitted between materials with the minimum possible absorption. This need arises from the coupling of high vacuum beamlines with external samples and detectors (some of which are under vacuum themselves). "Windows" for x-rays are typically made from a couple different

materials, including beryllium or kapton. Beryllium (atomic number 4) is the lightest element that is not gaseous or highly reactive. The extremely low density of this material allows it to be nearly transparent in the x-ray spectrum. Beryllium is often used for windows into the active regions of solid state detectors, which need to be kept under high vacuum.

Kapton is an orange-colored polymer film developed to remain flexible and stable throughout a wide range of temperature variations. In addition to these properties, kapton is also able to transmit x-rays with a very low rate of attenuation. As a result, windows made of kapton are often used to allow an x-ray beam to enter or exit a beamline under vacuum. Kapton is more flexible, less brittle, and cheaper than beryllium.

3.4.2 Filters

A thick enough block of almost any material (particularly a high-Z material) can be used to preferentially filter out lower energy x-rays due to the shape of the absorption spectrum described above. This form of filtering can be important because lower energy photons represent a common constituent of noise in a system. However, this method is ineffective at creating a monochromatic (single energy) beam. In order to achieve a single peak, pseudomonochromatic beam in an otherwise broad spectrum, the shape of the absorption spectrum of a material can be exploited. Typically, the K_α peak of a spectrum is used due to its largest initial intensity. While many L-shell x-rays are also produced, their low energies cause them to be very easily absorbed and not very useful for many applications. If a material is chosen such that its K-edge for absorption lies in between the K_α and K_β energies of the spectrum to be filtered, it will preferentially pass photons of the lower K_α energy while blocking photons of the higher K_β energy peak, counter to the general trend. This lower energy coincides with the local minimum in the absorption curve before the sharp K-edge rise of the filter which effectively blocks a

large fraction of the K_β photons.

This property can be particularly useful because the K_α and K_β peaks are often similar enough in energy so as to overlap if the peak widths are wide enough. For the best possible single-energy beam, as much of the K_β peak as possible must be attenuated while minimizing attenuation of the K_α peak. Because of the relative closeness of the energy of a K_α x-ray and the K-edge for the same material, an element of similar atomic number to the atoms producing the characteristic radiation can generally be used as a suitable filter. In many cases, a filter can be chosen from an element with an atomic number about one to three lower than that of the source.

However, in addition to reducing the amount of background radiation, a filter will also reduce the amount of usable signal of the desired energy. A filter typically takes the form of a thin foil, the thickness of which can be chosen based on the desired level of attenuation. If the filter material and thickness are chosen correctly, a ratio of intensities of $\frac{K_\alpha}{K_\beta} \approx 500$ can be achieved while only reducing the intensity of the initial K_α peak by about half. While filtering may be a quick and cheap solution for creating a somewhat monochromatic beam, depending on the application there are more suitable methods discussed below which do not result in attenuation of the desired peak.

3.4.3 Monochromators

In a second method, specific energies of x-rays can be selected by passing them through a monochromator. Monochromators come in two main varieties: grating and crystal. Grating monochromators (surfaces designed with a periodic array of geometric features, just as in a visible light diffraction grating) are only useful in the softer x-ray regime $(6 - 12\text{Å})$. Reflection by the grating diffracts the x-rays to different angles depending on their energy (much as passing light through a prism separates it into its component colors). By controlling the exit angle using a slit, the energy of the outgoing

beam can be reduced to a specific frequency range. The dimensions of this slit depend upon the desired energy resolution; a lower energy spread also results in a reduced intensity. However, higher harmonics of the target energy cannot be eliminated by this method since they also satisfy the diffraction condition.

As the wavelength of x-rays decrease, it becomes infeasible to fabricate gratings of the required dimensions. In this case, crystal monochromators become the component of choice. Crystals act as a natural grating with critical dimensions dictated by the interplanar spacing. Once radiation has left a crystal monochromator, it can be selected and controlled in much the same way described above.

3.4.4 Double Bounce Monochromator Systems

A system consisting of double x-ray mirrors may be used to eliminate unwanted higher harmonics. These setups are commonly used because the second crystal can redirect the beam parallel to its incident direction. Passage through a second monochromator also helps to eliminate many instrumental effects. A more thorough understanding of harmonic rejection in this system relies on details involved with x-ray reflection, so a discussion will be delayed until the following chapter.

3.5 Related Techniques

Extended X-ray Absorption Fine Structure (EXAFS) is a technique that makes use of the absorption curves of materials to help determine their compositions and structures. Absorption edges (such as the K-edge discussed earlier) are not perfectly sharp jumps in the level of absorption. Instead, they consist of oscillations corresponding to scattered waves interfering with themselves after being reflected from neighboring atoms. By studying these oscillations, it is possible to gain information regarding the number and

chemical identities of atoms within a crystal lattice.

Chapter 4

X-ray Reflectivity and Grazing Incidence X-ray Off-Specular Scattering

4.1 Reflection and Refraction at Surfaces

Loosely speaking, index of refraction can be taken as a measure of the speed with which light propagates in a material. As a result, the velocity of light travelling through a material with index of refraction n is given by:

$$v = \frac{c}{n} \tag{4.1}$$

where c is the usual speed of light in vaccum (in which $n = 1$). As light enters a medium with higher index of refraction, it slows down and subsequently bends towards the normal to the surface. This bending of light by a material interface is governed by Snell's law, which states that:

$$n_1 \cos(\theta_1) = n_2 \cos(\theta_2) \tag{4.2}$$

where the subscript numerals refer to media 1 and 2, and θ_1 and θ_2 are measured with respect to the interface. This differs from most optics conventions which measure angles with respect to the normal. As we will see shortly, much of x-ray physics involves grazing incidence (light impinging nearly parallel to a surface) so it is more convenient to use the alternative notation introduced here.

In the x-ray region of the spectrum, most materials appear virtually transparent. As a result, most surfaces do not reflect x-rays at large angles of incidence. The index of refraction for a material in the x-ray regime can be given by:

$$n = 1 - \delta + i\beta \tag{4.3}$$

where the meanings of δ and β are discussed shortly but are typically small, positive numbers. As a result, most materials have an index of refraction *less than* 1 in the x-ray spectral region, while the index of refraction is typically greater than 1 within a material in the visible light region. This phenomenon can be explained by x-ray frequencies, which are greater than many of the resonance frequencies of bound electrons. The specific parameters β and δ can be expressed by:

$$\delta = \frac{2\pi\rho r_0}{k^2} \tag{4.4}$$

$$\beta = \frac{\mu}{2k} \tag{4.5}$$

where r_0 is the scattering amplitude per electron, ρ the electron density, μ the attenuation coefficient, and k the wavevector. In these equations, β is a quantity indicative of

absorption losses and is therefore directly proportional to the mass attenuation coefficient.

The coefficient of reflection r is defined as the ratio of amplitude of the reflected wave to the incident wave. It may be expressed as:

$$r = \frac{\theta_1 - \theta_2}{\theta_1 + \theta_2} \tag{4.6}$$

Since the refracted beam represents the portion of the wave which is transmitted into a material, the coefficient of transmission t can be found as:

$$t = 1 - r = \frac{\theta_1 + \theta_2}{\theta_1 + \theta_2} - \frac{\theta_1 - \theta_2}{\theta_1 + \theta_2} = \frac{2\theta_1}{\theta_1 + \theta_2} \tag{4.7}$$

From the expressions for the reflection and transmission coefficients listed above, as θ_2 approaches 0, r approaches 1 and t approaches 0. This limit is known as total external reflection, similar to total internal reflection in water, which has a higher index of refraction than the air above the interface. Since materials have lower indices of refraction in the x-ray regime, they can instead be completely reflected back into air. To find this limit, we set $\cos(\theta_2) = 1$, and $n_1 = 1$. Total external reflection then occurs for all angles less than the critical angle, given by:

$$\theta_{\text{crit}} = \cos^{-1}(n_2) \tag{4.8}$$

Since $n_2 \approx n_1 = 1$, θ_{crit} must be small and the cosine function may be expanded in terms of the first two terms of its Taylor series expansion:

$$n_2 = 1 - \delta + i\beta = \cos(\theta_{\text{crit}}) \approx 1 - \frac{\theta_{\text{crit}}^2}{2} \tag{4.9}$$

As a result (focusing on the real part of the index of refraction), the critical angle below which total external reflection of the incoming beam occurs is given by:

$$\theta_{\text{crit}} = \sqrt{2\delta} \tag{4.10}$$

As an idea for comparison, $\delta \sim 10^{-8}$ in air and $\sim 10^{-5}$ in most solid materials. For a glancing angle below θ_{crit}, the penetration depth of an x-ray wave is reduced to the order of 2 to 7 nanometers. Meanwhile, for angles above θ_{crit}, the penetration depth is on the order of a micron. This property allows x-rays to be used in a variety of surface-sensitive applications. In addition, total external reflection of an x-ray beam is widely used for the guiding and focusing of x-rays in a system.

As a general rule of thumb, the critical angle can be approximated as $\theta_{\text{crit}}[^\circ] \sim \frac{1}{10}\lambda[\text{Å}]$, where λ is the wavelength of the incident radiation.

4.2 Reflective X-ray Optics

While a flat surface of nearly any sufficiently dense material can be used to reflect an x-ray beam at grazing incidence, the properties of certain materials and surfaces can be utilized to obtain a mirror with certain desired properties. Surface coatings are often made from elements with high atomic number and density. By plugging known constants into the equation for δ and the critical angle, the relation:

$$\theta_c = 2.32 \cdot 10^{-3} (\rho)^{\frac{1}{2}} \lambda \tag{4.11}$$

may be obtained, where ρ is the electron density. As a result, heavy metals such as gold and platinum are often used to create mirrors with relatively large critical angles.

Such mirrors also have the advantage of being able to act as low-pass filters to eliminate higher harmonics of radiation which may be allowed by a crystal monochromator. The reflectivity of materials used for these mirrors drops off very steeply as $\left(\frac{\theta}{\theta_{\text{crit}}}\right)^4$,

as the incidence angle increases beyond the critical angle. The critical angle is directly proportional to the wavelength of the incident radiation and thus varies depending on specific harmonics. As a result, if a mirror is set such that the angle of incidence is just below the critical angle for the desired energy, any higher harmonics will be heavily absorbed into the material (since the angle of incidence is well above *their* critical angles). A set of two mirrors can be useful for deflecting the beam back such that its exit angle is identical to its angle of incidence (see the section on double bounce monochromator systems in the previous chapter).

4.3 Refractive X-ray Optics

Optical lenses make use of both curved surfaces and differences in refractive index to bend light and make the width of a beam of light effectively increase or decrease. Lenses are characterized by a focal length; in the case of a converging (convex) lens, incoming parallel light rays focus down to a single point located at this distance with respect to the lens.

Similarly, in the case of a diverging (concave) lens, initially parallel light rays appear to have come from a single point at a distance of one focal length behind the lens. As a reminder, Snell's law states that:

$$n_1 \cos(\theta_1) = n_2 \cos(\theta_2) \tag{4.12}$$

Consequently, the larger the difference in refractive indices (n_1 and n_2) between air and the lens material, the more a light ray is bent to deviate from its initial path. X-ray lenses differ in a couple respects from their optical counterparts. First of all, as you may recall, the index of refraction of x-rays in materials is typically *smaller* than in air while the opposite is true for light in the optical portion of the spectrum. As a result, x-rays

entering a lens bend in the opposite direction than would visible light. Converging lenses for x-rays must then necessarily be made *concave*, counter to intuition. Additionally, indices of refraction for optical light can easily differ from unity by 0.1 or more, many times the amount by which they differ for x-rays. Because of these factors, it is actually quite difficult to bend x-rays to any appreciable extent. Lenses made for this purpose typically have very long focal lengths, on the order of 100m or more. For most practical applications of x-ray optics, systems containing many lenses must be used in series are used in place of a single lens to reduce the focusing distance.

4.4 Reflectivity Studies

For angles of incidence below the critical angle, the reflection of an x-ray at an interface is nearly perfect. However, even when incident at angles greater than the critical angle, a portion of an x-ray beam may be reflected from a surface. The reflectivity coefficient, defining the fraction of the incident beam that is reflected can be found by:

$$r = \frac{\theta - \theta_{\text{crit}}}{\theta + \theta_{\text{crit}}} \tag{4.13}$$

where θ is the angle of incidence. This reflection coefficient is given in the ideal limit of an infinite slab of the reflecting material. In cases involving thin films or coatings, this approximation is not sufficient. For these instances, the wave transmitted through the top surface may reflect from the boundary between the film and substrate, adding to the total reflected wave. In addition, the wave may bounce back and forth between the top layer of the film and the substrate (with lower total intensity each time). The resulting reflection coefficient is:

$$r = \frac{r_{01} + r_{12}p^2}{1 + r_{01}r_{12}p^2} \tag{4.14}$$

where r_{01} is the reflection coefficient between air and the thin film, r_{12} the coefficient between the film and substrate, and p is the phase factor, given by:

$$p = e^{\frac{4\pi\sin(\theta_1)t}{\lambda_1}} \tag{4.15}$$

in which t is the film thickness, and λ_1 and θ_1 are the wavelength and angle of reflection within the thin film. This phase factor is introduced because depending on the thickness of the film, subsequent reflections may be in phase or out of phase with the initial reflections. The reflection coefficient alone contains no phase information, so the phase factor reintroduces this phase when examining the superposition of waves composing the total reflected wave. For a thin film, the reflectivity becomes:

$$r_{\text{thin}} \approx -i\frac{\lambda\rho r_0 t}{\sin(\theta_1)} \tag{4.16}$$

Kinematical and recursive methods can be used to reconstruct reflectivity values from complex or multilayered surfaces.

The equations listed above can be examined for a few take-away messages. First of all, both the reflection coefficients and phase factors depend on the angle of incidence of the x-ray beam. Specular reflections are those for which the angle of incidence is equal to the angle of reflection. In a specular reflectivity scan, therefore, both the angle of incidence of the beam and the angle of the detector relative to the sample are varied to keep with the specular condition. In practice, however, it is typically much more difficult to move the incoming beam than the sample, so both the sample and detector positions are moved. Such scans are commonly called two-theta scans because as the angle of incidence is varied by an angle θ, the detector must be moved by an angle of 2θ.

The result of a reflectivity scan from thin layers results in a phenomenon known as Kiessig fringes. The angle between successive maxima can be used to measure film

thickness. Thus, reflectivity scans can be very useful for gaining information about multilayer structures.

A reflectivity scan is typically run for a range of incident angles between a fraction of the critical angle and several times the critical angle. In order to get the best possible signal from a thin film on a substrate, the starting angle for a reflectivity measurement is an angle intermediate between the critical angle for the film and the critical angle for the substrate (which is typically denser and has a larger critical angle). At this starting angle, a portion of the incident beam is transmitted into the film, but is completely reflected by the substrate. As a result, the maximum beam intensity is maintained by not losing any portion of the beam to transmission into the substrate material.

4.5 Porod's Law

The Fresnel equations of reflectivity provide us with an asymptotic form for intensity as a function of momentum transfer q by:

$$I(q) \propto \frac{1}{q^4} \tag{4.17}$$

for a smooth interface or:

$$I(q) \propto \frac{A_1}{q^4} + \frac{A_2}{q^{3+h}} \tag{4.18}$$

for a rough interface, where h is the roughness exponent [1].

4.6 Grazing Incidence X-ray Off-Specular Scattering (GIXOS)

Grazing Incidence X-ray Off-Specular Scattering, or GIXOS, is a more recent technique that is coming to replace X-ray Reflectivity for many applications. In GIXOS, guard slits are used to block all radiation except that incident at an off-specular angle, or $\theta \neq 0$ in the x-y plane. A 1-D profile of intensity in the z-direction is taken at a particular instant in time. This intensity profile can then be analyzed to reveal the out-of-plane structure of an interface.

Because GIXOS measurements are taken in a single shot, they reduce the amount of time the sample is exposed, and thus subsequently minimize radiation damage. Additionally, they require no movement of the sample or detector, as in x-ray reflectivity, and thus minimize motion of the sample due to motor movements and maintain a consistent x-ray footprint across the sample for the duration of the measurement.

GIXOS has been shown to provide roughly equivalent structural information as x-ray reflectivity, though with somewhat sharper interfaces [2]. Due to the advantages mentioned above, GIXOS provides an attractive alternative to reflectivity particularly in the case of soft matter samples which are easily damaged, or liquid interfaces, which can be disturbed significantly by either lateral or vertical movement of the sample motors.

Chapter 5

X-ray Detectors

5.1 Analog Detectors

5.1.1 Fluorescent Screens

Certain compounds such as zinc sulfide emit visible light in response to being struck by x-rays (in this specific case the emitted photons are yellow). Fluorescent screens are not often used except perhaps as a visual means of determining the location of an x-ray beam. However they are worth mentioning for historical purposes, as the discovery of x-rays was made by the observation of unexpected fluorescence indicating the presence of a previously unknown form of electromagnetic radiation.

5.1.2 X-ray Film

X-ray film and photographic plates were the first forms of x-ray detectors used for producing images and are still commonly used today in medical imaging. These films are composed of grains of silver halide compounds embedded in a matrix of gelatin. When ionizing x-rays interact with this film, some of the silver halide molecules become

sensitized and chemically reduced to neutral silver atoms. This change in the chemical composition of the film results in the formation of a latent image. When the film is later developed, the unmodified silver halide grains are washed away. Wherever metallic silver remains, it is effective at blocking light; thus the difference in light intensities transmitted through the film corresponds to areas of high or low radiation. The higher mass attenuation of bone as compared with soft tissue results in the characteristic black-and-white medical x-ray images. The only difference between x-ray film and traditional photographic film is that x-ray films are typically made thicker and contain larger silver grains. This is because x-rays interact with matter less strongly than visible light does; the added thickness of x-ray film provides a larger interaction region.

Conventional silver halide x-ray films are single use; the chemical change induced is not easily reversed. More recently, a form of x-ray plates which make use of the phenomenon of photostimulated luminescence have been put into production. When an x-ray hits a plate coated with a layer of a phosphor material, it can excite an electron into a metastable state from which it is unlikely to spontaneously become deexcited. Continued exposure to an x-ray source thus creates a latent image of excited electrons. Such a signal, however, is not viewable to the human eye. Instead, these images can be read by exposing the plate to red laser light. The energy of this light is sufficient to knock the electrons back out of their metastable excited state, releasing a higher energy (typically blue) photon in the process. These released photons can be detected to produce an electronic image of the beam intensity. Since the wavelengths of the incident and reemitted light are different, a filtered detector only sensitive to the emitted light is used to avoid “contamination” of the image by the scanning laser light. Since electrons transitioning between orbital levels is an easily reversed process, this form of image plate can be fully erased by exposure to a light source and thus can be reused to produce multiple x-ray images across its usable lifespan.

Since x-ray film is essentially an analog detector (as opposed to electronic detectors covered next), it has extremely high resolution and is relatively inexpensive. It also is not subject to electrical noise which is a common problem exhibited by many other types of detectors. However, photographic plates provide very little information on the energy of the incoming radiation and only provide a qualitative view of transmission and beam intensity. As a result, other forms of digital detectors have taken the stage in recent years.

5.2 Basic Properties

Other forms of x-ray detectors all share some properties in common; these will be covered in general before discussing specific instruments. The basic principle behind an electronic radiation detector is the ionization of molecules caused by the photoelectric effect. The charges that are created during this process are then collected and turned into an electrical signal. Because it is possible for radiation to pass through a detector without interacting at all, detectors may be characterized by their intrinsic efficiencies. The intrinsic efficiency of a system is defined as the ratio of recorded photons to the total number of incident photons on the detector. This quantity is often times a better measure of detector performance than the absolute efficiency (ratio of recorded photons to total photons emitted by the source) since it takes into account the finite size of the detector relative to the entire area over which photons are emitted. Many electronic detectors are also limited by a factor known as dead time, which is the minimum time separation required such that two photons are recorded as separate events. If two photons interact in the detector volume within a very small period of time, the effects of these two photons can pile up, making the two separate events look like a single larger event. Thus, dead time can be used as a measure of the best possible time resolution of a detector.

Detectors used for x-ray scattering experiments are called square law detectors. This is because the signal recorded by the detector is proportional to the square of the electric field. Equivalently, the signal is proportional to the signal intensity or the number of incident photons.

5.3 Gas Detectors (Ionization, Proportional, Geiger-Mueller)

When radiation is incident on an inert gas, it can provide enough energy to strip electrons from the surrounding air molecules, creating ion pairs; typically a pair will consist of a heavy positively charged molecule and an electron. Most commonly, Argon gas is used in such detectors; the process of ionization can be expressed as:

$$\text{radiation} + \text{Ar} \rightarrow \text{Ar}^{+} + e^{-} \tag{5.1}$$

The energy required to produce an Ar ion pair is 26.4eV. As a result, a single x-ray photon is capable of creating many ion pairs and excitations. An electric potential difference is applied across two metal plates (an anode and cathode) within a gas chamber. Often times, the entire apparatus is contained within a glass tube. The electrons that are collected at the anode collectively produce an electric current. The magnitude of this current is a measure of the relative intensity and energy of the radiation. It is possible, however, for a positive ion to recombine with an electron before reaching the anode, effectively eliminating detection of the original event. An increase in the strength of the electric field across the chamber can reduce the probability of this recombination and subsequent loss of information. However, as the electric field is increased still further, other processes described below must be taken into consideration. Gas detectors are divided into three

main categories depending on the strength of the potential difference across their internal chambers.

A detector with a potential difference of around 100-200V is known as an ionization chamber. Ion pairs created within this chamber drift towards the anode where they are collected, resulting in a relatively small current. Such detectors are prone to a large amount of noise and are particularly bad for application in situations with low levels of radiation; without a large amount of amplification, the current produced can be difficult to detect.

Since ionized air molecules are much more massive than the electrons that are produced during their ionization, they receive a much lower acceleration from the external field. However, with a sufficiently large electric potential difference (700-800V), electrons are able to attain enough kinetic energy to collide with neutral molecules of gas and cause further ionization. This ionization is similar to the photoelectric effect, only caused by an electron instead of an incident photon. This process is known as gas multiplication because a single ionization event can create a cascading effect, resulting in hundreds of detectable ions. These avalanche pulses of current are detected and measured in a set of gas detectors known as proportional counters. Accurate measurements require knowledge of the magnitude to which an avalanche will grow from a single ionization event. However, the resultant signal is much stronger and easier to detect than that in the case of an ionization chamber; gas amplification leads to a gain in current on the order of 10^5. Since the size of the current pulses produced is proportional to the initial number of ion pairs, measurements of current can provide information regarding incident photon energy.

If the electric potential is increased *yet higher* (to around 1000V), a chain reaction may occur in which avalanches of electrons promote further avalanches. This reaction proceeds until almost all of the gas atoms within the chamber are ionized. By the time

these avalanche currents are measured, they have very large amplitudes which require no gain but are also independent of the initial number of ion pairs causing them. Such a detector is known as a Geiger-Mueller tube; measurements from these detectors are simpler than those from proportional counters since knowledge about specific avalanche amplitudes is not needed. However, this also means that they provide little information about the energy of the incident radiation and have very long dead times during which they are insensitive to new radiation events. As a result, Geiger-Mueller tubes have come into use as a relatively simple form of detector to indicate the presence or absence of radiation.

5.4 Scintillator/Photomultiplier

Gas counters are relatively insensitive to photons of shorter wavelengths. To detect such photons, a scintillator-photomultiplier system may be required. Scintillators are materials which convert the kinetic energy of photons directly into light through electronic state transitions. Since visible light is relatively low in energy compared to an incident x-ray, the majority of the energy from an x-ray photon incident on a scintillator is dissipated as heat. Thus, the light signals are very weak and must be amplified into a usable signal.

A photomultiplier tube is a device similar to an ionization chamber, except that it contains high vacuum in the interior of a glass envelope, in place of a gas. Incident photons strike a photocathode, a thin deposit on an entry window, which results in the release of photoelectrons. These electrons are directed by a focusing electrode into a multiplier consisting of a set of plates known as dynodes. Each dynode is held at a higher voltage than the last one, thus accelerating the electrons as they travel from one to the next. As electrons collide with the surface of the dynode, they have enough energy to

further strip electrons from the dynode material, perpetuating a multiplication process similar to that in a gas counter. Photomultipliers are able to increase the initial signal by a factor of up to 10^8. Thus they are commonly used to turn relatively weak signals into measurable pulses of current, especially when coupled with the operation of a scintillator.

5.5 Solid State

Understanding the operation of solid state detectors requires a knowledge of semiconductors and electronic band structures, which will be briefly introduced here. An individual atom has discrete orbital energy levels; when individual atoms bind together into molecules, their electronic energy levels become slightly shifted. These shifts are related to the exclusion principle for electrons; no two electrons may occupy the exact same energy state. If two atoms are far enough apart that their orbitals do not overlap spatially to a great extent, then their electrons will not be significantly affected. However, as the atoms are brought closer and closer together, their electron orbitals begin to overlap and interfere with each other. This interaction results in a distortion of the energy levels slightly higher or lower than their initial states to accommodate all of the electrons without violation of the exclusion principle. As more and more atoms are brought into close contact with each other, these distortions begin to form a set of closely spaced energy levels. Eventually, when a number of atoms on the order of 10^{23} (on the order of Avogadro's number) are brought together into a solid lattice, the energy levels begin to blur and form a continuous distribution, known as a band. Depending on the exact nature of the atoms used to form the solid, some materials may form multiple energy bands, with energy gaps in between; no electrons are allowed to occupy a state with energy within these "forbidden" gaps.

Most materials can be identified in one of three specific groups, based on their

exact band structures. In all cases, the innermost electrons collectively form the inner filled band. Additionally, the outermost filled band is known as the valence band; this band represents the outer electrons which are most readily available for ionization or bonding. Yet higher is the conduction band; electrons occupying this band are no longer confined to a specific atom. While electrons in the conduction band are not considered free (they are still electronically bound to the material as a whole), they may freely move spatially between one atom and another, are easily transported by very little force, and are thus responsible for the conduction of electric currents.

Conducting materials (usually metals) consist of valence and conduction bands which overlap in energy; thus in their ground state, the conduction band is already partially filled. This property results in the ability of conductors to easily transport electrons. On the other hand, insulating materials are those which have a large energy gap between their filled valence band and their empty conduction band. As a result, they do not conduct any electricity in the ground state. In addition, the energy gap, on the order of 5eV or greater, is too large for electrons from the valence band to overcome by thermal excitation or most external forces. In the extreme case of a large electric field, dielectric breakdown may occur; in this process, electrons are stripped from the valence band into the conduction band, typically resulting in permanent material damage.

In between conductors and insulators is a class of materials known as semiconductors. As their name implies, they are able to conduct current in certain cases but not in others. Semiconductor materials have a very small energy gap between their filled valence band and their initially empty conduction band (at a temperature of 0K). In many cases, thermal energy or collisions with nearby particles can be sufficient to knock an electron out of the valence band and into the conduction band. Semiconductors are thus able to transport electric current depending on the population of electrons within their conduction band. Their electrical resistance is intermediate between that of a conductor

and an insulator.

Silicon and germanium, with four electrons each in their outermost shell, are the two most common materials used in semiconductor devices; they have energy gaps of 1.12 and 0.67eV, respectively. At room temperature, their conduction bands are partially filled due to thermal excitations of valence electrons. When an electron is moved from the valence band to the conduction band, it loses its association with its parent atom and leaves an electron vacancy, known as a hole, behind. This hole, by comparison with its surroundings, carries a positive charge since it corresponds to the lack of an electron. When an electric field is applied to a semiconductor, the conduction electron moves opposite the field lines. Additionally, bound electrons may also feel a force in this same direction and jump into the positive vacancies, thus leaving parent atoms ionized and causing holes to move in the direction of the electric field.

Semiconductors are typically elements found within group IV of the periodic table. When a small amount of an element from group III or V is mixed in, causing impurities, the semiconductor material is considered to be doped. These new atoms take the place that would otherwise be held by a semiconductor atom in the square lattice. Group V elements have five electrons in their valence band; due to the band structure of the semiconductor lattice, their fifth electrons are very loosely bound and easily displaced into the conduction band by thermal energy. Thus, even in its normal state, a semiconductor doped with a group V element may be considered to have a set of conduction electrons without the corresponding holes in the valence band. As a result, such a material is known as an n-type semiconductor because the majority of its charge carriers are negative (electrons).

Group III elements, which have three electrons in their valence band, require a fourth electron in order to completely bind into the semiconductor lattice. They normally achieve this desired energy state by borrowing an electron from a nearby atom, resulting

in the formation of a positive hole in one of the semiconductor atoms. If electron-hole pairs are subsequently formed by the addition of energy to the system, the majority of the charge carriers are holes in the lattice as opposed to electrons in the conduction band. As a result, such a material is known as a p-type semiconductor because the majority of its charge carriers are positive.

In a solid-state (semiconductor) radiation detector, a bias voltage is placed across a semiconductor material. Incoming radiation creates electron-hole pairs in much the same way as it creates ion pairs within a gas chamber. This radiation provides enough energy for an electron to overcome the band gap and enter the conduction band. A single photon may be responsible for the production of many charge-carrying pairs. Similarly, if a high enough bias voltage is applied, an electron can gain enough energy to create additional pairs, resulting in an amplification of the initial signal.

One fundamental problem with the use of semiconductor detectors is manifested in the creation of electron-hole pairs from thermal energy at room temperature. These charge carriers result in a phenomenon known as "dark current." Dark current is a type of electronic noise which registers a signal even when no radiation has interacted with the active detector region. As a result, germanium and silicon detectors must be cooled to eliminate these signals in order to most accurately measure the presence of radiation. They are typically cooled by constant thermal contact with a liquid nitrogen dewar (77K).

When solid-state detectors were first being put into use, semiconductor crystals could not be grown to a sufficient level of purity to be used directly in the manner described. Impurities in the materials would lead to trapping of electrons and holes, effectively extinguishing the signal before it could be measured. To turn these semiconductors into detectors, they underwent a "lithium drifting" process in which lithium ions were used to dope the material, effectively covering the impurities and allowing normal transport of electron-hole pairs. However, if allowed to warm to room temperature, the

lithium ions were freed to move around, thus destroying the detector. As a result, these detectors (known as SiLi and GeLi detectors) must continuously be kept at cold temperatures, while newer high-purity detectors may be allowed to warm to room temperature between uses without damage as long as they are cooled again before a bias voltage is applied.

5.6 Charge-Coupled Device (CCD)

When a p-type material is deposited onto the surface of an n-type material (or vice versa), it creates what is known as a p-n junction. Free electrons from the n-type side will tend to flow towards the p-type side, while holes from the p-type side move in the reverse direction. At the junction, free electrons and holes tend to diffuse into opposing regions and recombine, creating a zone with virtually no free charge carriers. This junction region then becomes known as a depletion region (since it is depleted of unbound charges). Both the n- and p-type materials are electrically neutral to start with – remember, it's just the free charges that result in these materials being called "positive" and "negative." However, after this depletion region forms, the net deficit of free electrons in the n-type material creates a net positive charge in this area, while the deficit of holes in the p-type material creates a net negative charge. These charges create an electric field which effectively prevents the depletion region from expanding to fill the entire material.

When a voltage difference is placed across a p-n junction with the p-type material at a higher potential than the n-type material, this difference creates an electric field opposing the field created in the depletion region. Since there are plenty of free holes left in the neutral region of the p-type material, they begin to diffuse across the junction as a result of the applied potential difference. Free electrons from the n-type region also begin to move in the opposite direction. This process decreases the width of the depletion

region and allows a current to flow freely through the junction. If in place of this "forward bias", a "reverse bias" is created by applying a voltage difference with the n-type region at a higher potential than the p-type region, holes are driven from the junction back into the p-type material and electrons are driven into the n-type material, thus widening the depletion region. As the depletion region grows, so too does the strength of the electric field opposing its spread. As a result, very little net current flows through the junction.

P-n junctions thus can be used to create devices known as diodes, which allow the flow of current in only one direction. As forward bias across the junction increases, so too does the current. For small reverse biases, very little current is able to flow. However, as the strength of the reverse bias is increased, a point is reached at which the depletion region spreads across the entire device. At this point, any further increase in voltage beyond this "breakdown voltage" begins to drive a current.

A charge coupled device (CCD) follows similar principles of operation to solid state detectors, but has the added advantage of being position-sensitive. CCDs are typically constructed from a layer of depleted silicon deposited on a substrate of undepleted silicon. Electrodes are positioned at each "pixel," squares on the order of 25μm across. When voltages are placed across these electrodes, they create individual potential wells. Electrons (and holes) are created when photons of radiation interact within the undepleted silicon. Due to the potential wells, these charge carriers are trapped inside the pixel at which they were created, thereby providing spatial information regarding the location of the incident radiation.

In order to read out the information from a CCD, the freed charges must be moved between potential wells. By shifting the phase of voltages across the electrodes, electrons can be moved from one pixel to the next. In a CCD, only a single output pulse can be read at a time. As a result, each single line of pixels is read out individually. After all of the charges from this line have been "pushed" to the output, a new line is brought into

the readout section by shifting every column of the remaining image down by one pixel. This process repeats until the entire image has been processed. Thus, CCD's can provide very useful information on average radiation intensities and locations, but are limited by slow readout times. However, they are typically not used for determining energies since multiple photons of radiation can be captured in a single pixel; thus the magnitude of the current from a pixel provides little information on the initial energy creating the charges.

Because CCD's are based on similar principles of operation as other solid state detectors, they are also prone to some of the same problems. The active detection volume of a single pixel is much smaller than the entire detection region of a high-purity silicon or germanium detector. As a result the effects of "leakage current" due to thermally generated electrons is not as severe; however some sensitive CCD's can be cooled to further reduce this noise. Additionally, while the spatial resolution of this form of detector is relatively good, electrons created by incident radiation may have time to diffuse into neighboring pixels before reaching a potential well. Additionally, each well is only able to hold a certain number of electrons. After this saturation limit is reached, new electrons which are generated cause the signal to "bleed" across a small region of pixels. Both of these effects lead to a broadening of the original signal footprint and it is best to record lower intensity signals if possible (by adjusting exposure time or signal attenuation) to achieve the highest resolution. Finally, as an image is being read out from a CCD, any stray radiation hitting the detector may register in the wrong pixel (since the pixels shift their electrons from their initial locations of generation during the readout phase). This leads to an effect known as "smearing," which can be minimized by shielding the detector from incident radiation as best as possible while the array is being read out.

Another problem that must be mitigated when using CCD's is that they are very prone to radiation damage when a pixel becomes oversaturated. Radiation damage can permanently affect the readout of a detector. In many cases, it can be accounted for by

performing background subtraction, as damage alters the noise level of individual pixels. In other cases though, it can make certain portions of a CCD sensor essentially unusable. To avoid this form of damage, most flight paths in x-ray sources are equipped with a series of filters to reduce the intensity of incident radiation. By choosing an appropriate level of filtering or attenuation, one can successfully avoid damaging both the sample and detector. Typical sets of filters can decrease the intensity of radiation incident on the detector by a factor anywhere from $\frac{1}{2}$ to $\sim \frac{1}{2^{16}}$.

5.7 PILATUS Detectors

A variation on the traditional CCD is the Pixel Apparatus for the Swiss Light Source (PILATUS). A PILATUS detector consists of an array of single-pixel CCDs. In other words, each pixel has its own readout chip. The advantages to this form of detector include greatly reduced readout times of the chip, higher dynamic range since not all pixels need to be read out simultaneously (the higher intensity pixels can be read more often than the darker ones), and a reduced possibility of damage due to oversaturation. The main disadvantages include much higher costs and larger pixel size, due to current technological limitations on the size of readout chips. PILATUS detectors are currently becoming more widespread, especially at x-ray free electron laser sources, and will likely continue to spread in popularity as their price decreases and achievable pixel size decreases. Some sources are also installing longer flightpaths in order to spread diffracted radiation over a greater distance and achieve the same resolution with a PILATUS detector as with a traditional CCD at a closer distance.

Chapter 6

Static X-ray Scatter Concepts

6.1 Introduction to Crystallography

Before we proceed into a discussion of x-ray scattering, it is useful to briefly introduce crystals, as a basic understanding of crystal structure is necessary for understanding some of the derivations that follow. A crystal is a solid material composed of atoms in a periodic arrangement. This periodicity is often called a crystal lattice. The building block of a lattice, known as a unit cell, represents the smallest repeating group of atoms, often in some variation of a cubic arrangement. Many books would now diverge discussing the finite number of atomic arrangements known as crystal systems or Bravais lattices. However, this discussion is very tedious and not particularly useful for a basic discussion of x-ray scatter unless you are specifically doing structural analysis.

When dealing with scattering from crystal planes, it is often important to be able to describe the relevant planes. First, the origin of a system is defined as one of the atoms in a unit cell. The three axes are defined with respect to the cell and thus may not necessarily be perpendicular to each other.

To define the Miller indices for a plane, the plane must first be shifted away from

the origin of the coordinate system (if it passed through it in the first place). It can be shifted in any direction provided that its original orientation is maintained. Next, the reciprocal of the intercepts this plane makes with each of the three crystallographic axes is taken (if the plane is parallel to an axis, this counts as an intercept at ∞ and thus has a reciprocal of 0). This set of three numbers is known as the Miller indices of a plane, and are typically written in the form (a,b,c) where the numbers a, b, and c correspond to the x, y, and z axes respectively. A bar over a number indicates that it has a negative intercept.

In addition to representing the reciprocals of the intercepts, Miller indices can also be taken as the vector direction of the normal to the plane.

6.2 Coherent Scatter

In this section, we will focus on coherent scatter and its measurement. The position of the detector with respect to the incident beam defines the scattering angle at which measurements are being taken. The intersection of the incident and exit beams defines the scattering volume, the region from which structural and dynamical information is gained. The image at the detector is the sum of contributions from all particles within the scattering volume.

A single x-ray photon has energy $\hbar\omega$ ($\hbar$ being Planck's constant $\hbar = \frac{h}{2\pi}$ and ω the angular frequency) and momentum $\hbar\vec{k}$ where $|\vec{k}| = \frac{2\pi}{\lambda}$ is the wavevector. A simple numerical relation between the wavelength and energy of an x-ray can be given by:

$$\lambda[\text{Å}] = \frac{12.4}{\varepsilon[\text{keV}]} \tag{6.1}$$

When a photon undergoes scattering by its interaction with an electron, it changes direction by transferring momentum to the electron. This wavevector transfer, commonly

called $\vec{q}$, is defined by:

$$\vec{q} = \vec{k}_i - \vec{k}_f \tag{6.2}$$

where $\vec{k}_i$ and $\vec{k}_f$ are the initial and final wavevectors, respectively. Since the amount of momentum transferred to the system by the photons can be given by $\hbar\vec{q}$, $\vec{q}$ is often called the momentum transfer, and has units of Å^{-1}. In most cases, we will be dealing with fairly elastic (coherent) scatter, in which the incoming x-ray transfers very little energy to the scattering particle during its collision. Thus, $|\vec{k}_f| \approx |\vec{k}_i|$, and these two vectors differ only by their direction, not by their magnitude. This simplifies much of the math to follow. Additionally, the condition of elastic scattering is a reasonable approximation for many scattering experiments where measurements are made at small angles relative to the incident beam.

The wavevector transfer q can be found in terms of the wavelength of incident light and scattering angle by the following:

$$q^2 = |\vec{k}_i - \vec{k}_f|^2 = k_i^2 + k_f^2 - 2\vec{k}_i \cdot \vec{k}_f \tag{6.3}$$

Assuming that the wavelength is changed very little in the scattering process, $|k_f| \approx |k_i|$ and that 2θ is the scattering angle (by convention):

$$q^2 = k_i^2 + k_i^2 - 2k_i^2\cos(2\theta) = 2k_i^2(1-\cos(2\theta)) = 4k_i^2\sin(\theta) \tag{6.4}$$

$$\therefore q = 2k_i\sin(\theta) = \frac{4\pi n}{\lambda_i}\sin(\theta) \tag{6.5}$$

where n is the index of refraction. Momentum transfer is an important concept for probing molecular structures at various scattering angles. Specifically, a certain value

of momentum transfer corresponds to a specific length scale being "viewed" within the sample. The condition for constructive interference (Bragg diffraction) is that:

$$m\lambda = 2d\sin(\theta) \tag{6.6}$$

As a result, when $m = 1$ (first order diffraction):

$$q = \frac{4\pi\sin(\theta)n}{2d\sin(\theta)} = \frac{2\pi n}{d} \tag{6.7}$$

Thus, different q values (scattering angles) probe different length scales, where length scale d is given by:

$$d = \frac{2\pi n}{q} \tag{6.8}$$

As a function of length scale or momentum transfer, the necessary scattering angle to probe can be found as:

$$2\theta = 2\sin^{-1}\left(\frac{\lambda}{2d}\right) = 2\sin^{-1}\left(\frac{q\lambda}{4\pi n}\right) \tag{6.9}$$

However, if a sample is homogeneous in its composition, it will not scatter the incident beam in any direction besides the forward direction (angle of incidence). If every subregion of the material has the same dielectric constant, then scattered light from these regions will be identical in magnitude but may have a different phase. If the scattering volume is taken to be large enough, then each of these regions can be paired with one opposite in phase. As a result, all scattered light is extinguished due to destructive interference of the waves. Thus, in order to gain information regarding the structure of a material, it necessarily must contain some inhomogeneities to introduce amplitude variations. However, inherent thermal fluctuations of the material cause molecules to

translate, rotate, and/or vibrate. These fluctuations are sufficient to cause the local variations in the dielectric properties of the material necessary to observe scatter.

Additionally, collective motion at different length scales can be probed and resolved as a function of scattering angle only if the sample is nearly transparent (single scattering regime). If the sample is opaque such that photons scatter off many sites before exiting, the wavevector dependence is lost. Static fluctuations (inhomogeneities) of even a small degree scatter light much more strongly than dynamic fluctuations, which are covered in a later chapter.

6.3 Speckle

X-rays passing through an inhomogeneous material (disordered system) will scatter to all angles. However, depending on the specific arrangement of molecules, the waves may constructively or destructively interfere after scattering to a certain angle from different regions of the illuminated volume. The field seen at a particular point on a detector is a superposition of all fields scattered to that angle from all charges in the illuminated volume. This pattern of constructive (light) and destructive (dark) regions is commonly called speckle. This can be understood just as a laser beam projected onto a far wall causes a nonuniform light distribution and appears speckled. In this case, however, the wavelength of the laser light is too long to be scattered off air molecules. The speckle is caused instead by roughness of the projected surface. Laser light bouncing off of portions of the wall of slightly different heights will interfere with itself, causing both light and dark illuminated regions. This is a form of speckle known as subjective speckle. Because the height projection of the wall surface depends upon the viewing angle, the speckle pattern will look different depending on the position from which it is seen. Subjective (or near field) speckle occurs from imaging an illuminated rough

surface and the pattern changes with position, thus appearing different from different angles and for different specifications of the imaging system. You have likely noticed this phenomenon when looking at a laser beam projected on a wall; as you move your head slightly, you will notice the speckled pattern of brighter and dimmer regions changes.

Instead of being formed by the roughness of the projection surface, a laser beam can also be passed through a semitransparent rough material such as a piece of scotch tape or plastic. The length differences upon passage through this rough medium create speckles, which will be projected from this point onto a viewing surface. This is the form of laser speckle known as objective, or far field, speckle. Because the speckles are projected from a source, they are fixed in position and can be viewed from any angle without seeing any changes (like a painted picture). The mean speckle size in this case can be given by the equation:

$$d_{\text{speck}} = \frac{\lambda z}{L} \tag{6.10}$$

where d_{speck} is the speckle diameter, λ is the wavelength of the light, z is the distance between the scattering medium and projection surface, and L is the beam diameter. This speckle size is equal to twice the transverse coherence length. Small speckles come from large regions of multiple scattering, while large speckles come from small regions of single scattering (the preferred regime).

The above discussion assumes that the "roughness" of the illuminated material is stationary. If this is not the case and the medium is moving (imagine the diffusion of particles suspended in solution), then the objective speckle pattern will change as a function of time. At each instant, this speckle encodes information regarding the structure of the target material. By analysis techniques such as those described in the next chapter, the structure of the sample may be recovered from these speckle patterns. Additionally, while analogies were made to laser light, this is because laser speckle is a concept which

can be more easily understood. However, the above information also applies to x-ray speckle if viewed using an x-ray detector.

For most applications, it is highly desirable to position the detector such that the size of the speckle (d_{speck} in equation 6.10 above) is roughly the size of a pixel on the detector. If an individual speckle is larger than the pixel size, then the maximum intensity due to the constructive interference is spread over a larger area and the autocorrelation functions discussed in the following chapter are not able to track the speckle as well. If the speckle size is smaller than the pixel size, resolution is lost. In both cases, the contrast of the measurement is reduced.

6.4 Scattering Math

Solid angle is a tool used for the measurement of angles in three dimensions. The unit used to measure solid angle is the steradian, and there are 4π steradians in a sphere (just as there are 2π radians in a circle). A good way to think of solid angle is as the surface area occupied by an object on a sphere centered at the point of observation. As a result, an object near to the observer will occupy a greater solid angle than that same object at a greater distance. The number of steradians in an entire sphere can be seen from the formula for the surface area of a sphere, $4\pi r^2$, where r is the radius.

The x-ray scattering cross section, σ, is a measure of how well a material is able to scatter incident photons. The spatial distribution of these scattered photons can vary widely from isotropic to mainly concentrated in the forward direction. The differential scattering cross section is a quantity which can be used to measure the angular distribution of scattering. It can be found by:

$$\frac{d\sigma}{d\Omega} = \frac{\text{Number of scattered photons passing through given solid angle}}{\text{Number of incident photons}} \tag{6.11}$$

In terms of the electric incident and radiated electric fields, this quantity is given as:

$$\frac{d\sigma}{d\Omega} = \frac{|\vec{E}_{\text{rad}}|^2 R^2}{|\vec{E}_{\text{in}}|^2} \tag{6.12}$$

where R is the distance from the scattering object to the detector. When the differential cross section is integrated over the entire 4π steradians, it yields the overall scattering cross section for the material. Thus:

$$\sigma_{total} = \int \left(\frac{d\sigma}{d\Omega}\right) d\Omega = \int_0^{2\pi} \int_0^{\pi} \left(\frac{d\sigma}{d\Omega}\right) \sin(\theta) d\theta d\phi \tag{6.13}$$

6.5 Structure Factor

The static structure factor of a material represents a mathematical description of how the material scatters incident radiation. In the case of x-rays, it is a rough measurement of electron density, as electrons are the primary source of scattering. The structure factor of a given arrangement of electrons at a particular momentum transfer value $\vec{q}$ is given by:

$$S(\vec{q}) = \frac{1}{N} \left\langle \sum_{j,k} e^{-i\vec{q}(\vec{R}_j - \vec{R}_k)} \right\rangle \tag{6.14}$$

where N is the number of electrons, j and k are the indices for the electrons, and $\vec{R}_j$ is the position of electron j.

6.6 Introduction to Fourier Transforms

A Fourier transform takes a time-dependent function and breaks it down into its frequency-dependent components. In other words, the transformation breaks a function into pieces which are all sine and cosine waves of varying amplitudes and frequencies. Mathematically, this looks like:

$$F(\xi) = \int_{-\infty}^{\infty} f(x) e^{-2\pi i x \xi} dx \tag{6.15}$$

which bears similarity to a continuous form of the structure factor shown in equation 6.14. In fact, it can be shown that a diffraction pattern formed by x-rays interacting with a material is exactly equal to a spatial Fourier transform of the material structure.

6.7 Reciprocal Lattice

Due to the similarities and overlap between diffraction patterns and Fourier transforms, a common tool used when discussing radiation scattering experiments is reciprocal space. Reciprocal space is a Fourier inversion of real space; thus a reciprocal lattice is the Fourier transform of a real space crystal lattice. In reciprocal space, length scales are inversely related. Thus, crystal planes that are close together in real space are spread far apart in reciprocal space. This is one of the reasons that diffraction is so useful for studying molecular and atomic structures; small structures are spread out and easier to measure in reciprocal space.

Momentum transfer, $\vec{q}$ is the unit of measurement in reciprocal space. Diffraction measurements taken as a function of $\vec{q}$ in real space are often referred to as reciprocal space measurements, since $\vec{q}$ is measured in Å^{-1}. Rotating a sample in real space changes the position of the crystal lattice and the angles of that lattice with respect to the incident

radiation and detector. Thus, rotating a crystal also changes the diffraction pattern and reciprocal lattice.

6.8 Ewald Sphere

The Ewald sphere is a geometric construct used to determine the condition for constructive interference when scattering radiation from a given material. The radius of the Ewald sphere is $\frac{1}{\lambda}$, and is centered about the point from which the radiation is scattered. Geometrically, at all points on the surface of the sphere, $2d\sin(\theta) = \lambda$, which is equivalent to the Bragg condition for constructive interference. Therefore, lattice points on this surface will diffract perfectly. The basic idea of crystallography is to rotate each possible lattice point in a sample through the Ewald sphere and measure the resulting patterns, since not all lattice points lie simultaneously on the surface of a sphere.

6.9 Scattering Regimes

Scattering principles apply validly to all wavelengths of light; what actually matters is the ratio of the wavelength to particle size. There are many different scattering regimes, dictated by this ratio as well as the identity of the scatterers. These are introduced briefly as follows, though a full discussion of these scattering regimes is beyond the scope of this dissertation:

- Thomson: An electromagnetic wave is scattered elastically by charged particles with $R < \frac{\lambda}{20}$, with intensity independent of angle.
- Rayleigh: An electromagnetic wave is scattered elastically by neutral particles with $R < \frac{\lambda}{20}$. Light is scattered by the rotational and translational degrees of freedom

only (no vibrational). Rayleigh scattering is responsible for the sky being blue due to its inverse wavelength^6 dependence.

- Compton: An electromagnetic wave is scattered inelastically by a charged particle $R > \frac{\lambda}{20}$.
- Debye/Mie/Tyndall: All three of these names correspond to an electromagnetic wave scattered by spheres $R \sim \lambda$.
- Geometrical: An electromagnetic wave is scattered by particles $R \gg \lambda$.
- Rutherford/Coulomb: Subatomic particles or nuclei are elastically scattered in a material in this regime.
- Mott: Subatomic particles or nuclei are inelastically scattered in material in this regime.
- Raman: An electromagnetic wave is scattered inelastically by an acoustic phonon.
- Brillouin: An electromagnetic wave is scattered inelastically by an optical phonon.

A good rule of thumb for determining the intensity distribution as a function of scattering angle is that the scattering is concentrated mainly within an angle less than:

$$\theta \sim \frac{35}{d} \tag{6.16}$$

This rule of thumb can give a pretty good indication of how isotropic a scattering center is.

When an electromagnetic wave impinges on a material, it shifts the charges within bound molecules, thereby inducing an oscillating polarized electric dipole. These oscillations emit a new wave of the same wavelength λ.

Small particles act as point scatterers. Once the molecules get larger than 20nm or so, several oscillating dipoles are simultaneously created within the particle, thereby creating dipoles with varying phase differences. These differences introduce interference and a nonisotropic intensity distribution. This distribution causes further complications that are reflected in the structure factor.

The intensity of radiation emitted by an electromagnetic wave is strongest perpendicular to the oscillation axis. As a result, the scattered intensity depends on the polarization of the incident beam:

- horizontal: $I \propto \cos^2\theta$
- unpolarized: $I \propto \frac{1}{2}\left(1+\cos^2\theta\right)$
- vertical: $I \propto 1$

6.10 Neutron Scattering

Neutrons interact with the nucleus of an atom via the strong force (only at short distances). They are weakly scattered but have a large penetration depth and are non-destructive to the sample, which can be useful for studying samples prone to radiation damage. Additionally, neutrons may be used to study magnetic effects from unpaired orbital electrons due to interactions with their own magnetic moment.

We can compare the energy of an x-ray to that of a neutron used to study the same material features. Interatomic spacings are on the order of 1Å. For an x-ray, $1\text{Å} \sim 3\cdot 10^6\text{THz} \sim 12.4\text{keV}$. For a neutron, $1\text{Å} \sim 3.96\frac{\text{km}}{\text{s}} \sim 81.8\text{meV}$.

6.11 Laser Diffraction

Laser diffraction is a method which measures the scattering pattern (intensity) as a function of angle, guesses a size distribution using Mie theory, and compares expected with actual results. This technique is good for particle sizing because it can be done *in situ* without being invasive to the sample.

Multiple scattering is always a potential problem with light scattering techniques. These techniques are designed based on the concept of light either being transmitted directly through the medium or else scattered once into the detector. If the light scatters off a second particle before being detected, this multiple scattering can lead to incorrect informations. The problem of multiple scattering can be solved by sample dilution.

6.12 Liquid Surface Diffraction Grating

Early in my graduate studies, I ran across a study that used light to study capillary wave motion on the liquid surface. I was confused at how changing the angle of observation changed the wavelength, or frequency, of the capillary waves observed on the surface, so I figured out a derivation of this problem. The dispersion relation for capillary waves states that

$$\omega = \sqrt{\frac{\gamma q^3}{\rho}} \tag{6.17}$$

In a diffraction grating:

$$d\sin(\theta) = m\lambda \tag{6.18}$$

so as θ changes, the d ("grating spacing") producing that intensity maxima also changes. d is related to the capillary water waves by:

$$d = \lambda_{\text{water}} = \frac{v_{\text{water}}}{f_{\text{water}}} \tag{6.19}$$

$$v_{\text{water}} = \left(\frac{\gamma q}{\rho}\right)^{\frac{1}{2}} \tag{6.20}$$

Therefore:

$$d = \frac{v_{\text{water}}}{\frac{\omega}{2\pi}} \tag{6.21}$$

$$d = \frac{2\pi}{q} \tag{6.22}$$

Plugging into equation 6.18, we have:

$$\frac{2\pi}{q}\sin(\theta) = \lambda \tag{6.23}$$

Thus, the surface of water with capillary fluctuations behaves as a diffraction grating. Typically, a diffraction grating has a fixed d and separates different wavelengths to different angles. In our case, we have a monochromatic beam, but the liquid surface is a superposition of many different d's, so θ changes for different d's.

Chapter 7

Correlation Functions

7.1 Autocorrelation

In general, a correlation function measures the similarity between two random variables. Specifically, an autocorrelation function measures the similarity between a signal and a time-delayed version of that same signal. Autocorrelation functions can thus be useful for measuring periodicities in a signal or measuring rates of a given process such as diffusion. If $A(t)$ is a changing property, the average value of A over all time may be calculated as:

$$\langle A \rangle = \lim_{T \to \infty} \frac{1}{T} \int_0^T A(t) dt \tag{7.1}$$

The autocorrelation of $A(t)$ is given similarly by:

$$\langle A(0)A(\tau) \rangle = \lim_{T \to \infty} \frac{1}{T} \int_0^T A(t)A(t+\tau) dt \tag{7.2}$$

Or, for discrete time intervals:

$$\langle A(0)A(\tau)\rangle \cong \lim_{N\to\infty} \frac{1}{N}\sum_{j=1}^{N} A_j A_{j+n} \tag{7.3}$$

These last two forms give the value of the autocorrelation function of a signal for a specific time delay τ. It gives an indication of how correlated a signal is with itself after a time τ. To gain any time-resolved information, the autocorrelation function must be found for many values of τ. Correlation functions can be found either in software or by a hardware correlator board.

Since a signal must be perfectly correlated with an exact copy of itself, the maximum possible correlation occurs for $\tau = 0$. The autocorrelation function of a variable may remain equal to this initial value for all time delays τ; in this case, the variable is a constant of motion and the sample is completely static. Otherwise, the function will decay from its initial value for which it is a maximum. This behavior can be understood more simply in the following manner: for small but nonzero values of τ, the property A has not had much time to fluctuate from its initial value. Thus, for most values of t at small τ,

$$A(t)A(t+\tau) \approx (A(t))^2 \tag{7.4}$$

However, for a larger value of τ, $A(t+\tau)$ is nearly completely unrelated to $A(t)$. The average of these cross terms will be smaller than the average of the squares, found for small τ. It may be argued that it might just so happen that $A(t+\tau) \approx A(t)$ for some large value of τ. However, in general, this will only be the case for specific values of t. When averaged across all values of t, this correlation will become irrelevant. However, in certain cases, A may be a periodic function, highly correlated with itself against certain intervals of τ. This case will be discussed in the section below. In other cases, the autocorrelation function will tend to smoothly decay from its initial value as the signal

becomes uncorrelated with itself as the system of interest changes.

Since all experimental autocorrelation functions must be found in discrete and finite time intervals, the number of points used to calculate each value decreases as τ increases. This is because fewer and fewer data points are available at longer time delays before the end of the data set is reached. Autocorrelation for larger time delays is based on fewer and fewer data points – in some cases nonphysical solutions may be caused by finding the average over too few values. Such problems may be manifested in an autocorrelation function which increases above its initial value at some later time, $t \gg 0$. For this reason, many autocorrelation functions are calculated only for $\tau < \frac{T}{2}$, where T is the time length of the data set.

In the large time limit (ignoring the effects discussed above of a finite data set), a signal is expected to become completely uncorrelated with itself. In mathematical forms, these two limits may be expressed as:

$$\lim_{\tau \to 0} \langle A(0)A(\tau) \rangle = \langle A(0)A(0) \rangle = \langle A^2 \rangle \tag{7.5}$$

$$\lim_{\tau \to \infty} \langle A(0)A(\tau) \rangle = \langle A(0)A(\tau) \rangle = \langle A \rangle^2 \tag{7.6}$$

Often times, an autocorrelation function is normalized by dividing by the value at the long time limit, $\langle A \rangle^2$. As a result, the autocorrelation function will decay to a final value of 1 from an initial value of $(1+\beta)$, with $(1+\beta) = \frac{\langle A^2 \rangle}{\langle A \rangle^2}$, where $0 < \beta < 1$, with the exact value dependent upon the measuring instruments and alignment. β is called the contrast of a system; in experiments, a higher value of β is desirable.

7.2 Time-Fitting Models

In general, the autocorrelation function of a variable fits both the zero and long time limits. What happens between these two limits, however, may vary. Typically, it can be modeled in one of several ways involving an exponential function. These solutions take the following general form:

$$\langle A(0)A(\tau)\rangle = \langle A\rangle^2 + \{\langle A^2\rangle - \langle A\rangle^2\}e^x \tag{7.7}$$

In this equation, x varies according to the physical system but in all cases is proportional to $-t$ or $-(t^n)$. As a result, for $t \to 0$:

$$\langle A(0)A(\tau)\rangle = \langle A\rangle^2 + \{\langle A^2\rangle - \langle A\rangle^2\} \cdot 1 = \langle A^2\rangle \tag{7.8}$$

and for $t \to \infty$:

$$\langle A(0)A(\tau)\rangle = \langle A\rangle^2 + \{\langle A^2\rangle - \langle A\rangle^2\} \cdot 0 = \langle A\rangle^2 \tag{7.9}$$

which agree with the time limits set by the autocorrelation function in equations 7.5 and 7.6.

7.2.1 Regular Exponential

Most stochastic variables (those whose values are dictated by probabilities) have an autocorrelation function which decays as a single exponential:

$$\langle A(0)A(\tau)\rangle = \langle A\rangle^2 + \{\langle A^2\rangle - \langle A\rangle^2\}e^{-\frac{t}{\tau}} \tag{7.10}$$

A graph showing the correlation as a function of time is often known as a correlogram. In this (and future) forms, τ represents the relaxation time of the system, or the time required for the autocorrelation function to decay from its initial value to a value smaller by a factor of $\frac{1}{e}$.

7.2.2 Stretched or Compressed Exponential

When an autocorrelation function is measured for a soft matter system, the decay may take place over a much longer or shorter time interval. Such a form may be modeled by the following form, where α varies from its value of 1 for a regular exponential decay:

$$\langle A(0)A(\tau)\rangle = \langle A\rangle^2 + \{\langle A^2\rangle - \langle A\rangle^2\}e^{-\left(\frac{t}{\tau}\right)^{\alpha}} \tag{7.11}$$

For values of $0.5 < \alpha < 1$, or a stretched exponent, the system is said to be glassy, with little spatial ordering and long-timescale dynamics. For values of $\alpha > 1$, or a compressed exponent, the system is said to be jammed, or in a state of structural arrest. A compressed exponential represents a faster decay, which seems to be counterintuitive to the idea of a jammed system in which the system is largely static. However, it can be understood in the context that a jammed system is one in which there are long periods of time with little motion, and short periods of time with lots of motion. For example, imagine pouring grains of sand onto a pile. The height of the pile of sand increases most of the time, but there are occasionally avalanches in which a large fraction of the grains become rearranged and the height of the pile suddenly decreases. These are the dynamics that are picked up by a compressed autocorrelation function. In another example, imagine being packed onto a crowded bus. In order to get off the bus at a given stop, instead of pushing your way through the crowd, it is easiest to wait for those closest to the door to file off, then follow the string of people who leave the bus in their wake.

7.2.3 Superposition of Exponentials

Some systems may involve different sizes of particles that exhibit molecular motions at different rates. Instead of a single exponential decay, the autocorrelation function for this type of system will appear as a superposition (sum) of different single decays:

$$\langle A(0)A(\tau)\rangle = \langle A\rangle^2 + \sum_{i=1}^{N} C_i\{\langle A^2\rangle - \langle A\rangle^2\}e^{-\frac{t}{\tau_i}} \tag{7.12}$$

In this form, N represents the number of different decay times, each with a different coefficient C.

7.2.4 Oscillating Decay

When a system exhibits periodicities (such as from an external oscillating field), the autocorrelation function will not take the form of a simple decay. Instead, after one period, the variable will appear more correlated with itself than it does at some intervening time. At half-period increments, the signal will be anti-correlated with itself and may even dip below the lower decay limit of $\langle A\rangle^2$. However, due to some irregularity in the system, the function does not typically return to its initial value, but will instead peak at some lower value, following the trend of a decaying exponential:

$$\langle A(0)A(\tau)\rangle = \langle A\rangle^2 + \{\langle A^2\rangle - \langle A\rangle^2\}\cos(\omega t)e^{-\frac{t}{\tau}} \tag{7.13}$$

7.2.5 Gaussian

Systems with an equilibrium (Gaussian) distribution of velocities among its particles may be modeled with a Gaussian decay:

$$\langle A(0)A(\tau)\rangle = \langle A\rangle^2 + \{\langle A^2\rangle - \langle A\rangle^2\}e^{-\left(\frac{t}{\tau}\right)^2} \tag{7.14}$$

7.3 Autocorrelation Functions for EM Waves

The first order normalized autocorrelation function for an electromagnetic wave is defined in terms of the electric field magnitudes:

$$g_1(\tau) = \frac{\langle E(0)E^*(\tau)\rangle}{\langle E(0)E^*(0)\rangle} \tag{7.15}$$

The complex conjugate on $E(t)$ is used to eliminate the $e^{(-i\omega t)}$ component common to all such waves, to allow for a real solution for $g_1(\tau)$. However, this equation is of limited use because it is difficult to measure $E(t)$ directly. Instead, the intensity of a wave is typically measured. Since the intensity is proportional to the square of the electric field, this gives rise to the second order correlation function which can thus be expressed in the form:

$$g_2(\tau) = \frac{\langle I(0)I(\tau)\rangle}{\langle I(0)I(0)\rangle} \tag{7.16}$$

In this equation, complex conjugates are no longer needed because $I(t)$ represents a real function. This is the form of the autocorrelation calculated for most experiments. The two autocorrelation functions can be expressed in terms of each other using the Siegert relation, derived below:

$$I(t) = E(t)E^*(t) \tag{7.17}$$

Therefore,

$$\langle I(0)I(\tau)\rangle = \langle E(0)E^*(0)E(\tau)E^*(\tau)\rangle \tag{7.18}$$

Since $E(t)$ is a Gaussian variable of zero mean, this reduces to a sum over all possible products of their second moments, according to Isserli's theorem:

$$\langle I(0)I(\tau)\rangle = \langle E(0)E^*(0)\rangle\langle E(\tau)E^*(\tau)\rangle + \langle E(0)E(\tau)\rangle\langle E^*(0)E^*(\tau)\rangle + \langle E(0)E^*(\tau)\rangle\langle E^*(0)E(\tau)\rangle \tag{7.19}$$

Looking at the first of these terms:

$$\langle E(0)E^*(0)\rangle\langle E(\tau)E^*(\tau)\rangle = \langle I(0)I(\tau)\rangle = \langle I\rangle^2 \tag{7.20}$$

while the second term averages to zero since:

$$E \propto e^{-i\omega t} \Rightarrow |\langle E(0)E(\tau)\rangle|^2 \propto |e^{-2i\omega t}|^2 \tag{7.21}$$

This leaves:

$$\langle I(0)I(\tau)\rangle = \langle I\rangle^2 + |\langle E(0)E^*(\tau)\rangle|^2 \tag{7.22}$$

Dividing by the square of the average intensity gives the final form:

$$g_2(t) = \frac{\langle I(0)I(\tau)\rangle}{|\langle I\rangle|^2} = \frac{|\langle I\rangle|^2}{|\langle I\rangle|^2} + \frac{|\langle E(0)E^*(\tau)\rangle|^2}{|\langle E(0)E^*(0)\rangle|^2} = 1 + g_1^2(t) \tag{7.23}$$

In practical applications, the Siegert relation is used in the form:

$$g_2(t) = 1 + \beta g_1^2(t) \tag{7.24}$$

where β is known as the Siegert relation coefficient, or the contrast, which varies between a value of 0 and 1. In the ideal case, $\beta = 1$, but owing to current experimental limitations

such as finite detector resolution, limited beam coherence, and thermal noise, a value on the order of 0.1 is more common.

Chapter 8

Time-Resolved (Dynamic) X-ray Scatter

8.1 Spectral Density and Filter Technique

When light is bounced off of a medium in a state of motion (such as particles suspended in a colloidal solution jostling around due to Brownian motion), the electrons which scatter the light are thus also in motion. As a result, they represent moving radiation sources which shift the frequency of the radiated light via the Doppler effect.

The spectral density, also known as the power spectrum, of a time-dependent autocorrelation function for an electromagnetic wave is given by:

$$I(\omega) \equiv \frac{1}{2\pi} \int_{-\infty}^{+\infty} \langle E^*(t) E(t+\tau) \rangle e^{i\omega t} d\tau \tag{8.1}$$

This function represents how much the frequency of light is "spread" by the motion of the medium under study. Consequently, the amount of broadening seen in the power spectrum is related to the diffusion coefficient of the particles, which is in turn related to their size and shape. This density function is the Fourier transform of the first order

autocorrelation. By setting $\tau = 0$ and inverting this equation, the mean square of the electric field can be found by:

$$\langle |E(t)|^2 \rangle = \int_{-\infty}^{+\infty} I(\omega) d\omega \tag{8.2}$$

As a result (in the discrete time limit), $I(\omega)\Delta\omega$ represents the fraction of the magnitude of E that falls within a frequency interval of width $\Delta\omega$. If monochromatic (single frequency) light is incident on a system, it will have a very small spectral spread. The spectral density can thus be used to measure how much the spread in frequencies changes as a result of scattering through a material. While many molecular processes may be studied by the x-ray photon correlation spectroscopy technique discussed below, the finite readout time of detectors and computation time of autocorrelators limits their use to timescales $> 10^{-6}$s. Additionally, the motion of large molecules is too slow to observe the broadening of the power spectrum. As a result, slower processes must be studied in the time domain, which is the Fourier transform of the power spectrum.

Faster processes may be studied by using a diffraction grating or other filter to separate the outgoing waves into their corresponding frequencies. As the filter is swept through a range of frequencies, the detector is able to measure how much of the scattered beam lies within certain frequency ranges. The faster the particle motions within the sample, the wider the spectral distribution. Since this spectral spread is directly related to the correlation of electric fields via a Fourier transform, these techniques may be used to study time dependent properties on very short timescales.

Direct measurement of the frequency spectrum is the most straightforward use of dynamic scattering techniques. However, it is more common to use optical mixing techniques whereby fluctuations in speckle patterns are monitored. The two techniques are related under certain conditions. First, the sample must consist of a large number of uncorrelated scattering sites. Second, interparticle motions must be large enough to fully

randomize speckle pattern (fluid sample or loosely bound scattering sites). In the case of multiple speckle correlations (line/area detector), this requirement is relaxed. Finally, the scattering site dynamics must not vary over the time scale of the measurement (the sample must be in thermal equilibrium and produce no gradual phase change).

8.2 Optical Mixing Techniques

For measuring processes on longer length scales, an optical mixing technique must be used in conjunction with x-ray photon correlation spectroscopy, described below. There are two main methods which can be used: homodyne and heterodyne. In the homodyne configuration, only the scattered light is measured at the detector, whereas in the heterodyne configuration, the scattered light is mixed with a reference (unscattered) beam before reaching the detector. In the homodyne method, since only the scattered field is involved, the autocorrelation of the measured intensity (in terms of E_s, the scattered field, is given by:

$$\langle |E_s(0)|^2 |E_s(t)|^2 \rangle \tag{8.3}$$

which is identical to the second order autocorrelation function for an EM wave. However, in the case where the detected light is a superposition of the scattered (E_s) and incident unscattered (E_u) fields, the intensity autocorrelation is defined by:

$$\langle |E_u(0) + E_s(0)|^2 |E_u(t) + E_s(t)|^2 \rangle \tag{8.4}$$

which can be expanded to:

$$\begin{aligned}
&\langle E_s(0)E_s^*(t)E_s^*(0)E_s(t) + \cancel{E_s(0)E_s^*(t)E_s^*(0)E_u(t)} + \cancel{E_s(0)E_s^*(t)E_u^*(0)E_s(t)} + \\
&E_s(0)E_s^*(t)E_u^*(0)E_u(t) + \cancel{E_s(0)E_u^*(t)E_s^*(0)E_s(t)} + E_s(0)E_s^*(t)E_s^*(0)E_u(t) + \\
&\cancel{E_s(0)E_u^*(t)E_u^*(0)E_s(t)} + \cancel{E_s(0)E_u^*(t)E_u^*(0)E_u(t)} + \cancel{E_u(0)E_s^*(t)E_s^*(0)E_s(t)} + \\
&\cancel{E_u(0)E_s^*(t)E_s^*(0)E_u(t)} + E_u(0)E_s^*(t)E_u^*(0)E_s(t) + \cancel{E_u(0)E_s^*(t)E_u^*(0)E_u(t)} + \\
&E_u(0)E_u^*(t)E_s^*(0)E_s(t) + \cancel{E_u(0)E_u^*(t)E_s^*(0)E_u(t)} + \cancel{E_u(0)E_u^*(t)E_u^*(0)E_s(t)} + \\
&E_u(0)E_u^*(t)E_u^*(0)E_u(t)\rangle
\end{aligned} \tag{8.5}$$

where the crossed out terms are zero due to a missing or extra complex conjugation (the complex conjugation rids the electric fields of their time-dependent oscillations, causing the intensity autocorrelation to be a real function). Thus any terms, E_s or E_u that are not multiplied by their complex conjugates oscillate in time and thus average to zero. With the assumption $E_u \gg E_s$, the first term can be considered negligibly small, and the last term is simply written as I_u^2, where I_u is the intensity of the unscattered field. This correlation is simplified to:

$$\begin{aligned}
&\langle E_s(0)E_s^*(t)E_u^*(0)E_u(t) + E_s(0)E_u^*(t)E_s^*(0)E_u(t) + \\
&E_u(0)E_s^*(t)E_u^*(0)E_s(t) + E_u(0)E_u^*(t)E_s^*(0)E_s(t) + I_u^2\rangle
\end{aligned} \tag{8.6}$$

If the scattered and unscattered fields are statistically independent, then the second and third terms are constants, since they each depend on both fields at a different time. Combining the first and fourth terms results in:

$$\langle I_u^2 + 2I_u \mathrm{Re}(E_s^*(0)E_s(t))\rangle \tag{8.7}$$

Therefore, while the homodyne method results in the second order correlation function, the heterodyne method is dependent upon the first order correlation function of the scattered wave. It is sometimes more useful to make measurements using the heterodyne method because all phase information is lost when measuring just the intensity of the scattered beam. Heterodyne mixing allows the system to maintain some of its phase information.

8.3 Photon Correlation Spectroscopy

The overall method of Photon Correlation spectroscopy, or PCS, is to measure the second-order autocorrelation function g_2 and extract g_1, which gives information on the dynamics of the scattering sites on the sample.

Speckle patterns, such as the laser speckle described earlier, are typically only able to be seen using sources of coherent light. This is because the phase of the light when it scatters from the sample must be taken into consideration. Without a coherent light source, light scattering from different regions on the sample will not be in phase with each other, and will have the same average intensity almost everywhere. The only way to extract information from constructive and destructive interference is when the initial phase of the light is known. Until recently, lasers were the only readily available source of coherent radiation. Thus the technique of dynamic light scatter (DLS), measuring time-dependent properties using laser speckle, came about.

Recently, with the advent of bright third-generation synchrotron sources, the new technique of x-ray photon correlation spectroscopy (XPCS) has become feasible. Because x-rays have much smaller wavelengths, they are able to probe systems on a much smaller length scale. The basic principle underlying both DLS and XPCS regards the spatial arrangements of particles or molecules in the materials through which the

beam passes. Changes in the spatial arrangement of these particles causes a change in the speckle pattern (as particles move, the interference pattern will change according to the new positions of the scatterers). As projected on a detector (with the types of detectors listed below), these changes in speckle will appear as intensity fluctuations. Because the size of the beam is typically large compared with the size of the particles under study, the illuminated volume contains a large number of particles. This large number can lead to very fast changes in the intensity of scattered light. These intensity fluctuations thus encode important structural and dynamical information regarding the sample and its molecules. The autocorrelation of intensity can be used to find rates of motion of particles within the illuminated volume. For instance, DLS is commonly used to measure the diffusion rate of particles in a colloidal solution. In this technique, the relaxation time from a fitted decay of the autocorrelation of intensity is directly related to the diffusion rate; the faster the speckles change, the faster the particles were moving.

XPCS can be operated in one of two main modes. In transmission mode through a thin sample, bulk properties of a material may be probed. Additionally, when operated at a grazing incidence (due to the critical angle reflection of x-rays), XPCS becomes a highly surface sensitive technique.

8.3.1 Point Detector (0D)

A 0-dimensional point detector, such as a PIN diode or a scintillation counter can be used to obtain intensity information at a single q-value (scattering angle). While it has the fastest readout time of the detectors, it is only able to probe a single point and thus may be more prone to noise than the other systems which are able to average fluctuations across multiple points.

8.3.2 Linescan (1D)

A linescan consists of a CCD array one or two pixels wide and up to a few thousand pixels in length. It has an intermediate readout time and allows for q-value binning; averaging across a set of pixels can provide a more accurate autocorrelation function than that found from a single point.

8.3.3 Area CCD (2D)

While a CCD detector has the slowest readout time, it allows for the most averaging over various scattering angles. The two dimensional area also allows for full imaging of large speckles, as opposed to a linescan detector which will only display cross sections of speckles.

In all of the above cases, accurate information is required regarding the position of the detector relative to the incoming beam. This is the parameter that dictates the scattering angle and subsequent length scale being probed.

Since it is the readout time of a CCD that is prohibitive to studying faster dynamics, not the line transfer rate within the CCD, XPCS can be performed in a hybrid "kinetics" mode to combine the advantages of a 1D detector with that of a 2D detector. In kinetics mode, slits are used to confine the incident radiation to a small portion of the 2D detector. This portion is exposed for a set time, then all lines on the CCD are shifted downwards before the next exposure. Since this shifting time is fast, a full CCD image can end up with a set of strips, separated in time by only a small increment.

8.4 Characteristics of XPCS Autocorrelation Curves

Before XPCS measurements are taken on a dynamic sample, a known static reference sample such as aerogel is often used to establish the maximum contrast due to

the sample setup and beam characteristics. Likewise, measurements on this static sample over a long period of time establishes the maximum delay time before stability of the beam and/or sample setup interfere with accurate measurements of sample dynamics.

If the autocorrelation curve from a sample is completely flat, it can either mean that the sample is completely static, or that the dynamics are too fast to resolve using the given detector settings. These options can be distinguished between depending on the value of the autocorrelation. If close to 1 (the baseline), then the dynamics are too fast to resolve. If close to the value seen for the static reference sample, then the dynamics are too slow to measure in the given setup.

Chapter 9

Dynamic Light Scattering Alignment

9.1 Introduction

The purpose of this chapter is to provide a complete procedure and guide to alignment of a laboratory Brookhaven Instruments BI-200SM goniometer system for dynamic light scattering (DLS). This guide was developed by myself (Leandra Boucheron) and Jacob Stanley, as we found the pre-existing procedure lacking for our research purposes. Towards the end of the chapter, we provide a complete rationale describing the differences between our alignment procedure and that provided by the company. This procedure could be adapted to other models of laboratory DLS systems.

9.2 Laser Polarization Alignment

The distribution of radiation produced by scattered light depends on the initial polarization of the incident beam (and thus how well it is able to effectively induce oscillations in the scattering centers). As a result, it is important to properly orient the laser.

- By markings on the laser housing, comparison with a polarizer of fixed (known) polarization, or some other means, rotate laser such that its beam is vertically polarized.

9.3 Optical Axis Alignment

This section results in the optical axis of the laser being parallel to optical table axis. No further adjustment of 'pitch' and 'yaw' (i.e. laser angles) should be done. Remaining laser adjustments after this step will only be translational.

- Choose table axis (line of screw holes) to which the optical axis (laser path, i.e. z-axis) will be aligned.

- Mount two identical ThorLabs optical bases (BA2) along the chosen table axis.

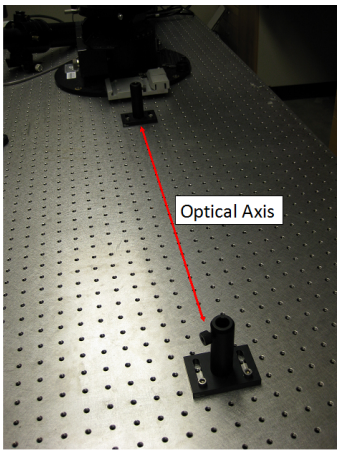

Figure 9.1: Optical axis with optical bases mounted along table axis

- Place ThorLabs lens mounting rings (LMR1) onto 8 inch posts and insert into optical bases.

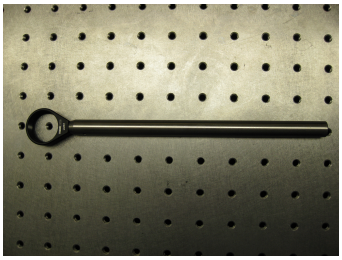

Figure 9.2: An 8” standard optical post with attached lens mounting ring

- It is essential that the optical bases and lens mounting rings be as normal to optical axis as possible.
- Place ThorLabs lens alignment targets with pinholes (LMR1AP) onto lens mounting ring.

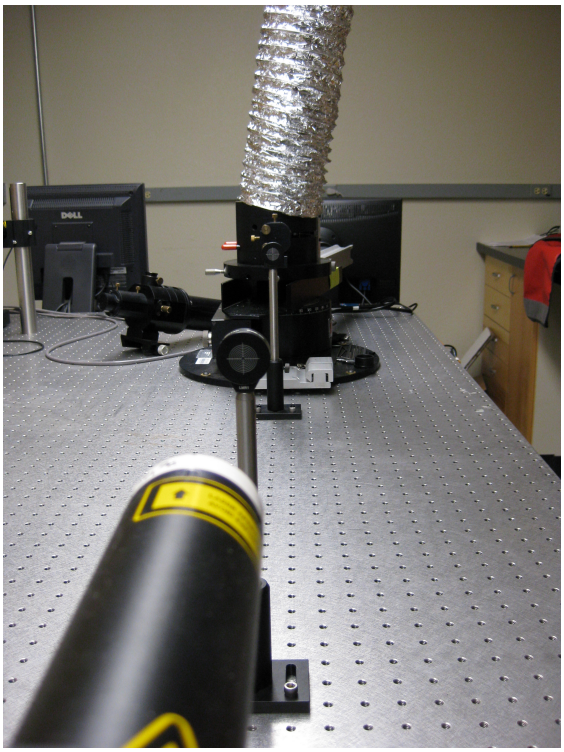

Figure 9.3: Looking down the optical axis with alignment targets in place

- Turn on laser. Laser should already be positioned and adjusted reasonably close to the front alignment target.

- The ‘x-axis’ is that which is parallel to the table’s surface (i.e. horizontal). The ‘y-axis’ is that which is normal to the table’s surface. Both are perpendicular to the optical (i.e. z-) axis.

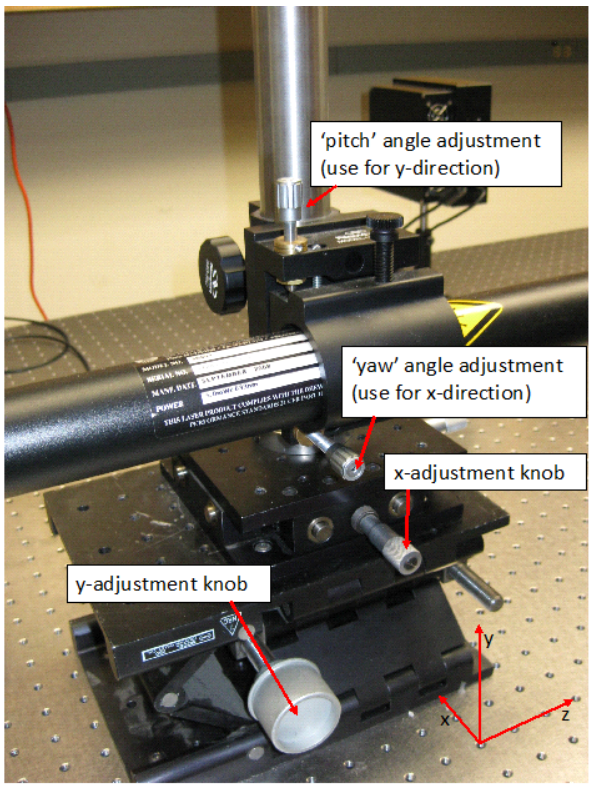

Figure 9.4: Adjustment knobs and axes labels for laser

- Adjust x and y translation knobs so that laser passes through pinhole on the first (closer to laser) alignment target.

- Now one must iteratively align the x and y directions of the laser using the translation and angle knobs for each of the x and y axes. Adjust the directions one at a time.

- Iterative process: Adjust the appropriate angle knob so that the laser spot moves towards center of the second (farther) alignment target. This will move the laser

spot away from the first pinhole. Now use the corresponding translation knob to move the laser spot back toward the pinhole on the first alignment target. Repeat this process until the laser spot is centered along the axis on both alignment targets.

- Repeat this process for other axis, at which point the laser should pass through the pinholes on both alignment targets as seen below.

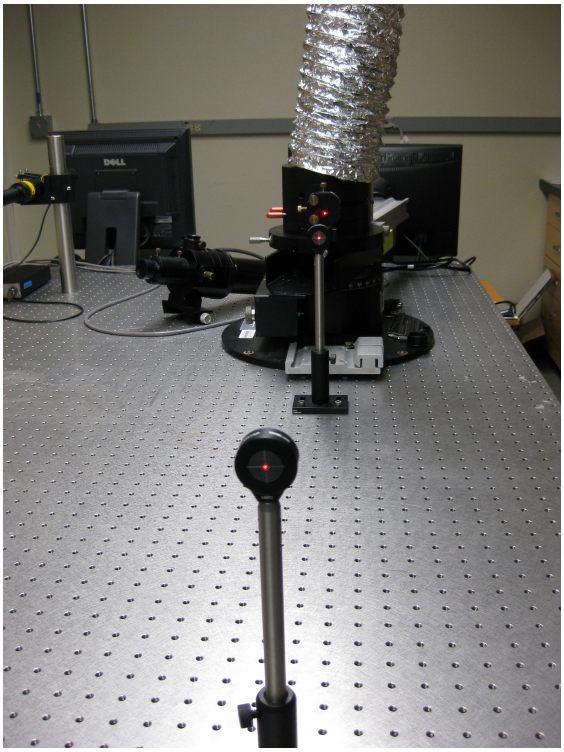

Figure 9.5: Laser optical axis fully aligned to table axis

- Remove alignment targets.
- You have now aligned the optical and table axes.

9.4 Goniometer Axis Alignment and Zeroing

This section results in the optical axis being collinear with the axis of the goniometer arm and the goniometer angle being zeroed in this configuration. After this

point no further adjustment of the laser's x and y translation should be done.

- Place pinholes on both sides of the goniometer arm with vat, housing, detector rail and all other central implements removed.

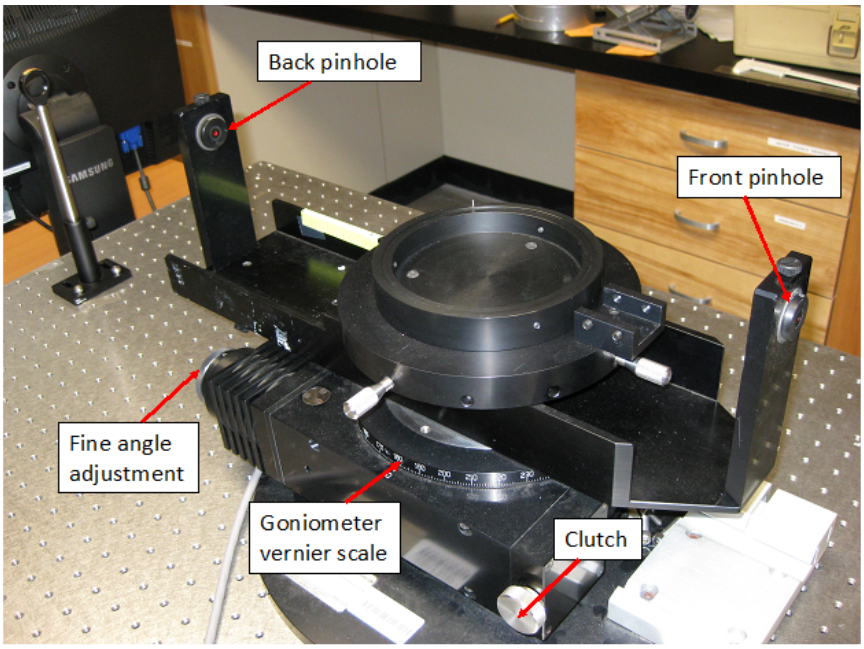

Figure 9.6: Placement of alignment pinholes and locations of goniometer angle adjustments

- Disengage clutch. The goniometer should now rotate freely. Rotate until the arm is approximately parallel to optical axis. Reengage clutch.

- Adjust laser x and y positions until the beam passes through the first (closer) pinhole.

- Now one must iteratively align the x direction of the laser beam and the angle of the goniometer arm until the beam passes straight through both pinholes.

- Iterative process: Adjust angle on goniometer arm using the fine control knob so that the laser spot moves towards the center of the second (farther) pinhole. This

will move the laser spot away from the first pinhole. Now use the x-translation knob on the laser mount to move the beam back towards the center of the first pinhole. Repeat this process until the laser spot passes straight through both pinholes.

- If the laser spot does not appear to be centered in the y-direction on the second pinhole, then the laser is not level and you will need to return to Step 1 of this alignment procedure.

- Loosen set screw located near 175° on the goniometer vernier scale disk and rotate by hand until the angle reads 0°. Tighten set screw.

- Repeat above step to zero fine adjustment knob using the set screw located on the side of the knob.

- You have now properly aligned and zeroed the goniometer.

- Remove back pinhole from the goniometer arm.

9.5 Detector Rail Alignment

This section results in the detector rail being positioned and fastened collinearly with the optical axis.

- Remove front pinhole from the goniometer arm.

- Place detector rail onto goniometer table. Fasten using two screws underneath table, *but only tighten these screws finger tight.* There should still be a small amount of play in being able to change the angle of the detector rail with respect to the rest of the goniometer setup.

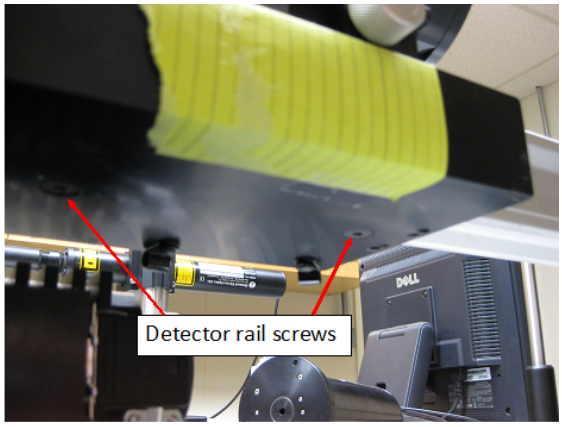

Figure 9.7: Location of detector rail adjustment screws

- Place some sort of pinhole apparatus onto the detector rail track (see example in picture below).

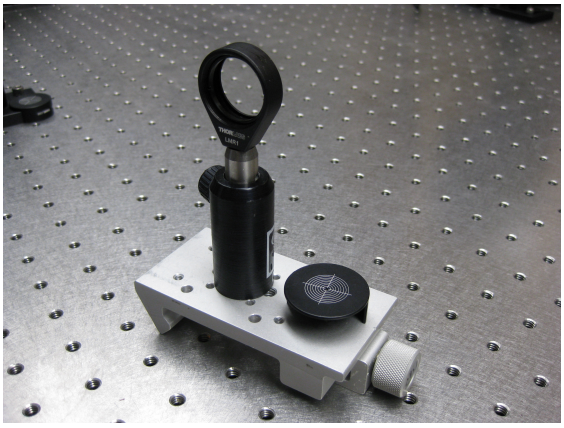

Figure 9.8: Example of pinhole apparatus which can be adjusted and moved along the detector rail

- Raise the laser height such that the beam is vertically aligned with the detector rail pinhole.

- Adjust detector rail (through play which is allowed by only hand-tightening the rail screws) such that the beam passes through the pinhole when it is at any point along the detector rail.

- Tighten detector rail screws using an Allen wrench. Ensure that the correct angle was maintained by rechecking alignment with pinhole at both ends of the rail.
- Replace front pinhole on goniometer arm.
- Adjust laser height such that the beam passes straight into this pinhole.
- Remove front pinhole and detector rail pinhole.

9.6 Sample Cell/Vat Alignment

This section results in the sample cell being centered on the central goniometer table and the vat (contained within) positioned such that the entrance window is normal to the optical axis.

- Tape a paper target on a wall as far as possible from the goniometer. Adjust target such that the laser spot hits the center.

Figure 9.9: Paper wall target with centered beam

- Place main body of the sample cell into the base of the sample cell assembly. With the laser on, rotate the main body until the 180° side window allows the beam to pass through uninhibited. Simultaneously try to center the main body in the sample

cell base as best you can by eye. The side window should be facing toward the front of the goniometer.

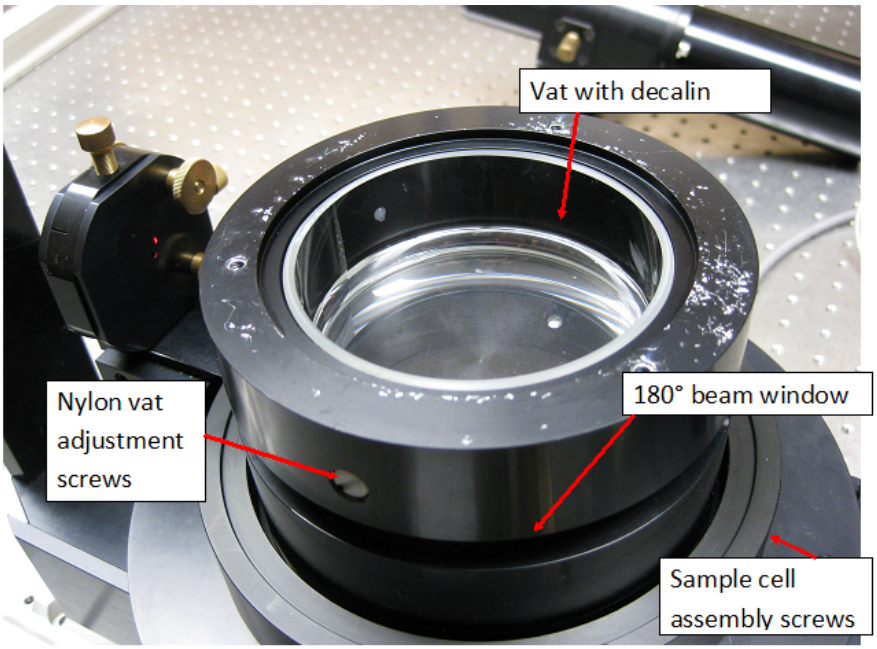

Figure 9.10: Main body of sample cell

- Locate the three allen wrench set screws around the edge of the sample cell assembly base. Starting with them equally unscrewed, tighten them each a full turn one at a time until the sample cell main body is held firmly in place.

- Double check that the laser still passes all the way through the side window. If not, you may have to loosen the set screws and readjust the main body.

- Now to insert the vat into the sample cell: be very careful when handling the vat. The scattering surface (that which, when in place, lines up with the 180° side window) should remain free of smudges, dust or finger prints so as not to introduce optical defects.

- Fill the vat up to the top of the side window with decalin.

- Hold a neutral density filter or some other reflective surface flush against the focusing optic mount.

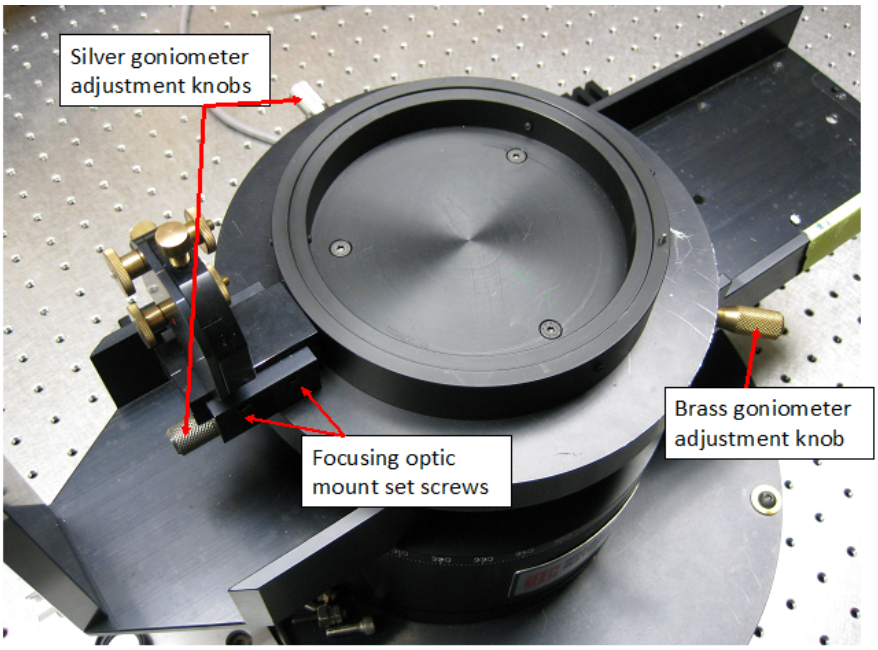

Figure 9.11: Main adjustments on the goniometer table

- Loosen the brass goniometer knob.
- Gently rotate the central goniometer table until the back reflection from the neutral density filter aligns with the exit aperture of the laser.

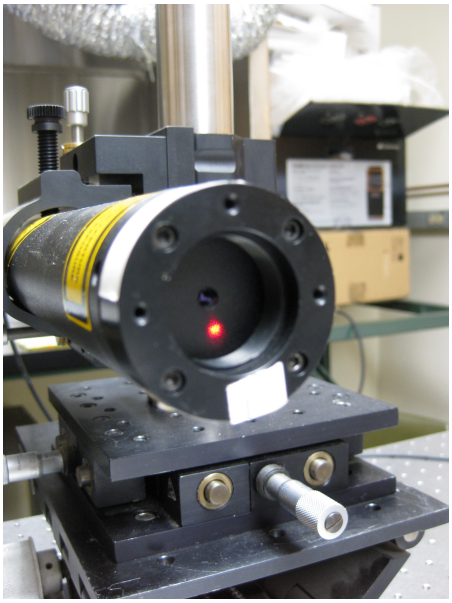

Figure 9.12: A well-aligned back reflection from a neutral density filter flush with the focusing optic mount or from the flat vat surface

- Remove the filter.
- Wearing latex gloves and only gently touching the upper surfaces of the vat, orient the vat such that the beam is approximately normally incident on the vat's flat surface. Rotate the vat such that the beam reflected from the flat surface aligns horizontally with the exit aperture of the laser. Note that the reflection will likely not be vertically centered.
- At this point the beam spot passing through the vat will not be circular and may no longer be centered on the target. If the latter is the case, adjust the horizontal central table position using the x-adjustment silver knob on the goniometer table.

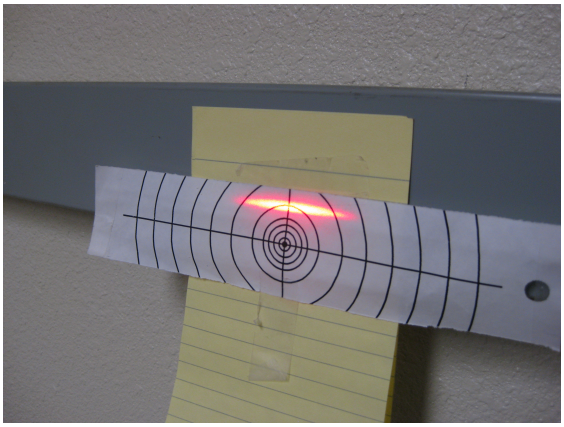

Figure 9.13: A centered beam on the wall target after adjusting central table position

- Check that the incident beam is still reflected back towards the laser aperture. If not, you will need to repeat the above steps (rotate central table, rotate vat with respect to the main body of the sample cell, horizontally translate the table) until the following three conditions are simultaneously met: the beam spot is horizontally centered on the wall target, the back reflection from the wall target is horizontally centered on the laser exit aperture, and the reflection from a neutral density filter held flush against the focusing optic mount is centered on the laser exit aperture. It may take several iterations to simultaneously satisfy these criteria.

- At this point gradually tighten the nylon screws holding the vat in place (BE CAREFUL not to overtighten: they can damage the vat).

- Tightening the nylon screws may slightly shift the position of the vat. Check that the three conditions listed above are still met. If not, loosen the nylon screws and try again.

- Place the brass manifold on top of the main sample cell body and **LOOSELY** tighten the three screws holding it in place.

- At this point the sample cell assembly should be properly aligned.

9.7 Focusing Optics Alignment

This section results in focusing optics pinholes and lens being centered and aligned.

- Slide the focusing optics mount into holder on central goniometer table.
- Tighten set screws holding mount onto goniometer table.
- Orient pinhole such that tapered side is towards the interior of the mount. Adjust its x and y positions such that the beam passes symmetrically through the pinhole.
- Tighten screws fixing pinhole in place.
- Place LINOS lens (100mm focal length) into focusing optic mount.
- Ensure that metal spacers are placed between vertical and horizontal lens adjustments screws and the lens. Otherwise, the lens will not be able to be adjusted by the screws located on the mount housing.

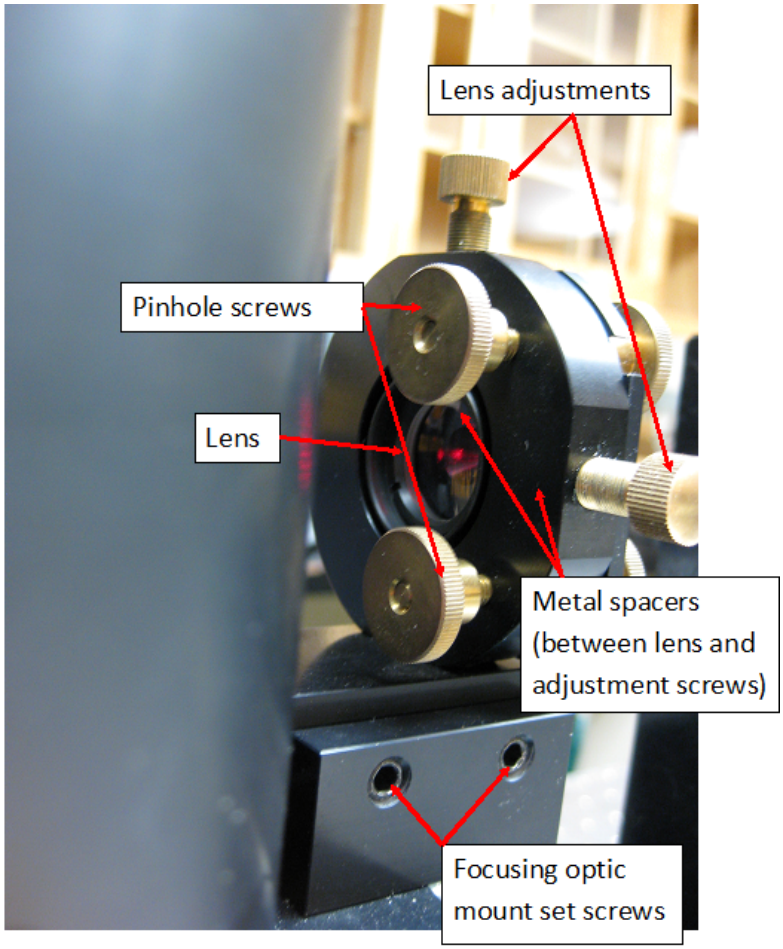

Figure 9.14: Adjustments on focusing optics

- Turn vertical and horizontal lens adjustment screws until the expanded laser beam is symmetrical and centered on the wall target.
- Place back pinhole into the focusing optics mount (oriented such that the tapered side is towards the lens). Adjust its position until the laser beam passes symmetrically through this pinhole by watching the wall target spot and edges of the pinhole.
- Tighten screws fixing the back pinhole into place.
- At this point, the focusing optics should be aligned and adjusted.

9.8 Detector Optics Adjustment

This section results in correct positioning of the detector optics slit and lens.

- Unscrew three screws holding photomultiplier tube (PMT) to detector optics.
- Slide optics onto detector rail. Tighten into place where the distance from the center of the goniometer table to the first vertical screw on the detector optics is approximately 14.5cm.

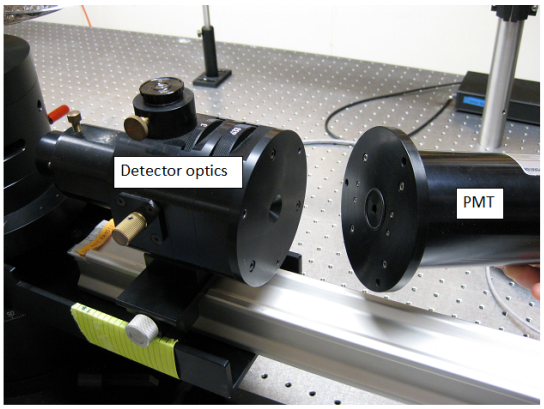

Figure 9.15: Detector optics in place on detector rail

- Make sure knob on mirror adjustment is rotated clockwise such that the laser beam passes straight through the detector optics.

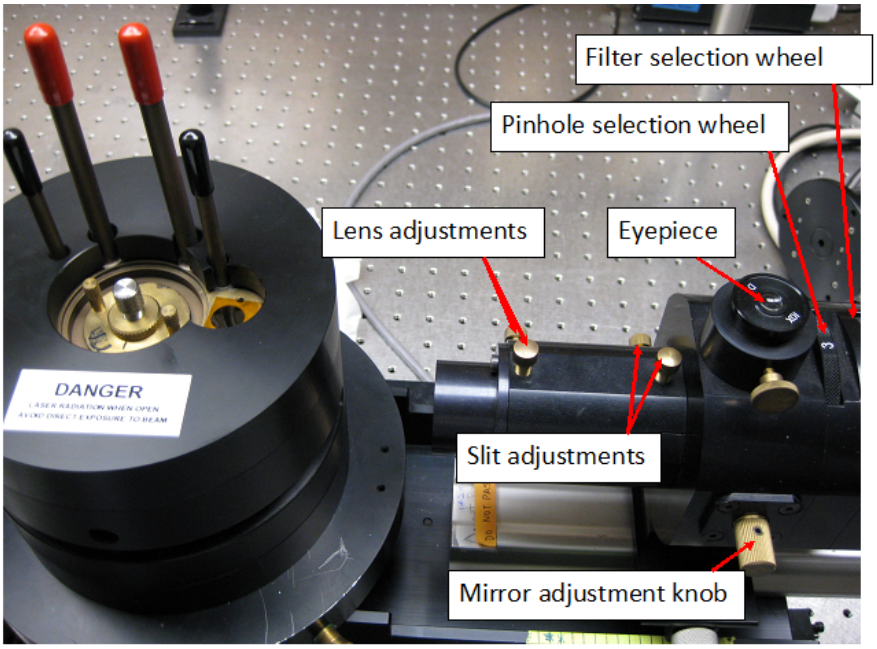

Figure 9.16: Detector optics components and adjustments

- Begin with the optics selection knobs rotated to 3mm aperture and open ('3' and 'O')
- Adjust slit vertical position to maximize beam spot intensity. You want the beam spot to be as uniformly bright, symmetrical, and centered as possible on the wall target. Repeat for lens vertical position.
- Adjust slit horizontal position to maximize beam spot intensity. Repeat for lens horizontal position. You may also need to rotate the goniometer table using the fine adjustment knob. However, these adjustments should be slight (less than $\frac{1}{10}^{\circ}$, or one mark on the knob). Most adjustments will need to be done with the horizontal (as opposed to vertical) positioning of the optics.
- Next, choose the 2mm aperture and adjust detector optics slit, lens, and possibly goniometer angle to center and maximize beam spot or diffraction pattern. Repeat for 1mm, 400μm, 200μm, and 100μm pinholes.

- Note that it is most important that the laser pattern be centered and symmetrical for the smaller apertures. For some of the larger apertures (mainly 2mm and 3mm), asymmetries may appear as the beam diffracts from the edge of the detector optics slit.

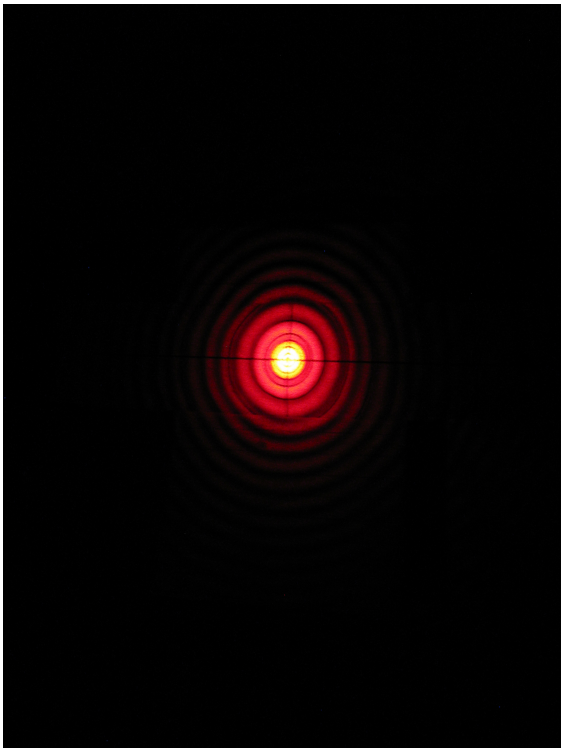

Figure 9.17: Diffraction pattern for 200μm pinhole

- If you are having problems getting good diffraction patterns, unscrew the front aperture from the detector optics and remove the lens. Adjust the slit horizontal position until the laser spot is centered on the wall target. Replace the lens and front aperture. Repeat the above process.

9.9 Center of Rotation Check

This section establishes that the previous steps have aligned the system well.

- Put the alignment pin in place of the sample holder.

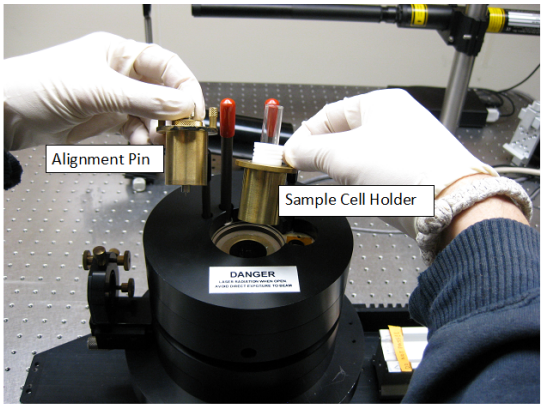

Figure 9.18: Sample cell holder and alignment pins as they are placed into the brass manifold

- Adjust pin height (by rotating screw on top of pin assembly) until the tip of the pin is below the beam. At this point, the incident laser beam should hit the pin (if not, the table is not well aligned and you may need to repeat the previous Focusing Optics and Sample Cell alignment steps).

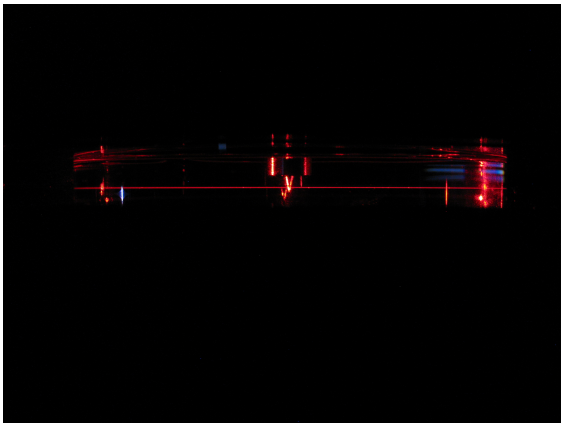

Figure 9.19: Pin well aligned with respect to the beam.

- Turn off laser beam.

- Turn knob on mirror adjustment counterclockwise by 90° so that light passing through the optics gets redirected through the eyepiece on the top of the optics.

- Shine a flashlight through the vat window onto the alignment pin.
- Look through eyepiece for tip of the alignment pin (should reflect brightly).
- If the pin tip is not centered in the slit window as viewed through the eyepiece, gently move the brass manifold on top of sample cell (this should have only been screwed loosely into place). If while moving this manifold around, you do not see the pin tip anywhere in the field of view, do not pass GO and do not collect $200. You will need to adjust the x-position on the central table such that the pin is centered in the slit and return to Sample Cell/Vat Alignment (step 5).
- If you **do** see the pin tip anywhere in the field of view of the slit, center it as best as possible by moving the brass manifold and tighten it into place fully with the three screws on top.
- Release the clutch on the main goniometer arm so that the detector rail can rotate freely.
- Continue shining the flashlight at the pin tip; keep looking through the eyepiece as you slowly rotate the goniometer arm from 0° through 150°. Ensure that the pin tip stays in the slit at all angles.
- If the pin leaves the slit window near 90°, you will need to adjust the table position by loosening the brass screw on the central table and using the silver z-adjustment screw. This *may* be okay, but you will still need to go back to step 5 and double check all alignments. Hopefully, any adjustments should be minor.
- If the pin leaves the slit window near 150°, you will need to make adjustments to the table x-position and return to step 5.

- If you have aligned everything carefully enough and the pin stays in the slit window for the entire angular range, congratulations! You have accomplished something that took us four months to develop and write up. Now leave a dire warning to make sure that undergrads do not mess with your alignment.

9.10 Rationale

The following contains a list of ways in which our procedure differs from that provided by Brookhaven Instruments (BI) and a defense of our reasoning.

- First of all, we found the BI procedure somewhat difficult to follow, both in language, assumptions, and lack of figures. We have attempted to make provisions in those areas we found lacking.

- Step 2: Since our specific laser mount and translation stages are unique to our setup and are not provided by BI, we found it necessary to elaborate on how to determine an optical axis. Additionally, we found it extremely helpful to align this optical axis with a fixed linear reference (the table) and developed a method to accomplish this using a set of alignment targets.

- Step 3: Again, in the process of aligning the optical axis with the goniometer system, we have provided instructions specific to our laser mount and also discuss an iterative procedure using both the laser adjustments and the goniometer angle. The rationale for this iterative process is that a translation of the laser affects the position of the beamspot on both pinholes equally, while an angular adjustment affects the position on the farther (back) pinhole to a greater extent. As a result, adjustments should be made to the angle while watching the back pinhole and to the horizontal translation while watching the front pinhole.

- Step 4: After following the preceding steps, we discovered that despite perfect alignment of the goniometer with the optical axis, the laser spot hit the *side* of the opening aperture on the detector optics when they were finally added to the system and did not pass straight into the center as would be expected. We learned that despite the countersunk openings for the screws fastening the detector rail in place, a fair amount of difference in the exact positioning of the rail could be made by simply tightening the screws while holding the rail in a specific configuration. As a result, we had to develop an alignment procedure for the detector rail to ensure that it is attached into place completely collinearly with the already established optical axis.

- Step 5: The BI procedure contains little information in way of how to determine placement of the sample cell assembly base. We have provided an outline for how to roughly center it on the central goniometer table. Any errors introduced by this rough procedure are accounted for and corrected.

  The central goniometer table is free to rotate with respect to the main stand, provided that the brass adjustment knob is loosened. However, for most rotations, the focusing optic mount is not maintained parallel to the optical axis. This can provide problems when adding the pinholes and lens to the focusing optic mount in a later step. It is, however, *not* so important that this mount be *collinear* with the optical axis, so long as it is parallel. The translational position of the focusing optics can be changed, but its orientation cannot. As a result, we have described the steps for using a reflective surface to ensure the back reflection is aligned with the laser aperture (that is to say, the laser is aligned normally to the surface containing the front of the focusing optics).

  Likewise, we found the initial BI procedure lacking in providing a way to align

the front flat surface of the vat. We describe a similar procedure to that mentioned for the focusing optic mount to ensure that the laser passes normally to this surface.

Our procedure stresses the importance of maintaining a horizontally centered beamspot on the wall target. This is because when the beam is normal to the front vat surface and the beamspot is *not* centered, it means that the beam is not passing through the exact center of the vat and is being refracted by the back surface. Only when the beam is both normal to the vat entrance AND centered on the wall target after passing through the entirety of the vat can it be stated that the beam passes throuh the exact center of the vat.

A true horizontal translation of the table should not affect the rotational orientation of either the vat or the central goniometer table. Unfortunately, we found that the silver x-adjustment knob on the goniometer table caused some slight rotations as well. As a result, we have described the importance of returning to verify the orientation of both the focusing optics mount and the vat after aligning the beamspot on the wall.

- Step 6: We have provided instructions on how to assemble and orient the focusing optics because it was simply assumed in the BI procedure that the focusing optics were in place and the pinholes well aligned, without ever mentioning how to accomplish this step.

- Step 7: If the preceding steps have been followed carefully enough, we found it unnecessary to substantially change the goniometer angle. Our detector optics alignment produced a rotation of less than two-tenths of a degree, which is smaller than adjustments to the main vernier scale can be made by eye. As a result, we found that it was not feasible or advisable to rezero the main goniometer angular scale at this point in the alignment, as dictated by the BI procedure. Additionally,

after several repetitions of the procedure, we were never able to obtain a suitable diffraction pattern from the 2mm or 3mm pinholes. As a result, our detector optics were aligned using mainly the smaller apertures.

- Step 8: This is this point at which our procedure differs the most from that dictated in the BI manual. While the manual stresses the importance of adjusting the central goniometer table and detector optics slit at this point, we found these steps counterproductive and we were caught in an endless loop of repeating steps. Since our procedure focuses more heavily on the preceding steps, we do so with the caveat that the two procedures accomplish slightly different end goals. We found that not everything is perfectly machined, such that aligning one set of components puts another one out of alignment, and that in the end, *something* must give. By stressing the importance of the vat/sample cell and detector optics alignment, we have decided that maintaining a direct optical axis is most important, while by stressing the importance of the center of rotation alignment, BI has decided that a consistent scattering volume is most important. Our rationale is that we have provided steps for ensuring a complete lineup of the incident beam with the flat vat entrance, center of the vat, and exit. By making adjustments to either the central goniometer table OR to the detector slit, one would be countering the steps just achieved. While this means that our procedure involving the alignment pin might not be perfect, all this means is that the scattering volume changes slightly as a function of angle the sample is viewed from. However, since most of our samples are homogeneous and we are *not* terribly concerned with scattered intensity as a function of angle, this factor is relatively unimportant. We do understand, however, that if the alignment pin is not at all visible through the detector optics, this may be indicative of issues in preceding steps and advise the user to revisit earlier steps in the procedure. We also determined that, much like the detector rail, there is

some amount of flexibility in the positioning of the brass sample cell manifold which holds the alignment pin before it is screwed down tightly. As a result, we have advised that this component initially be only loosely assembled and that its positioning be checked in this final step of the procedure.

Figure 9.20: Brookhaven Instruments Model BI-200SM after detonation of a blasting cap inside the sample vat

Chapter 10

Diffusion and Molecular Processes

10.1 Diffusion in 3 Dimensions

Techniques such as x-ray photon correlation spectroscopy (XPCS), along with its corresponding technique in the visible spectrum, dynamic light scattering (DLS) are frequently used to measure sizes of particles in solution. They do so by making use of the so-called Einstein-Stokes relation for spherical particles:

$$D = \frac{k_B T}{3\pi\eta d_H} \tag{10.1}$$

where D is the diffusion rate, k_B is Boltzmann's constant, T is temperature, η is the viscosity of the solution, and d_H is the hydrodynamic diameter, the effective size of the particle in solution. From this equation, it can be seen that the diffusion rate (and consequentially the speed of motion) of a particle in solution is directly a function of particle size. When incident light is scattered to a wave vector q from diffusing particles, the coefficient D can be modeled by the decay of the autocorrelation function as:

$$g_1(t) = e^{-Dq^2 t} \tag{10.2}$$

The inverse of the relaxation time of the exponential function, often denoted by the variable Γ can then be given:

$$\Gamma = Dq^2 \tag{10.3}$$

which can also be seen as:

$$\frac{\partial \rho}{\partial t} = D\frac{\partial^2 \rho}{\partial x^2} \tag{10.4}$$

$$\rho(x,t) = \frac{1}{\sqrt{4\pi Dt}} e^{-\frac{x^2}{4Dt}} \tag{10.5}$$

$$\overline{x^2} = 2Dt = L^2 \tag{10.6}$$

$$\langle \overline{x^2} \rangle = \int x^2 \rho(x,t) dx \Rightarrow t \propto \frac{L^2}{D} \propto \frac{1}{q^2 D} \propto \frac{1}{\Gamma} \tag{10.7}$$

Returning to equation 10.2, we have that:

$$g_1(t) = e^{-\Gamma t} \tag{10.8}$$

Since Γ is easily found from the decay rate of the autocorrelation function, the particle size can be found from:

$$d_H = \frac{k_B T}{6\pi\eta D} \tag{10.9}$$

Since q can be written as a function of θ by:

$$q = \frac{4\pi n}{\lambda_0} \sin\theta \tag{10.10}$$

Γ can also be expressed as:

$$\Gamma = \frac{k_B T \left(\frac{4\pi n}{\lambda_0} \sin\theta\right)^2}{3\pi\eta d_H} \tag{10.11}$$

and the decay time τ can be approximated by:

$$\tau = \frac{1}{\Gamma} \tag{10.12}$$

It is worth noting that instruments used for DLS or XPCS measurements are not calibrated. Instead, they are based on first principles calculations. Incorrect readings must be attributed to errors in setup/alignment or the instruments, as the setup can only be verified (and not corrected) by the use of size standards.

The intensity of scattered light is proportional to $(\text{particle diameter})^6$, so the intensity distribution is not linearly indicative of the actual size distribution of the particles.

The point where the autocorrelation function begins to decay indicates the relaxation time and thus gives information on the diameter of the particles. The slope of the decay indicates the polydispersity of the solution and thus the distribution of particle sizes about a mean diameter. The baseline can indicate the presence of large particles or aggregates that may settle out of solution.

10.2 Determination of Dimensionality of Diffusion

Diffusion along one direction in a three dimensional system behaves according to:

$$\langle x^2 \rangle = 2Dt \tag{10.13}$$

Looking at diffusion occurring over a length L for a diffusion timescale of τ (and remembering that the length L is related to the wavevector transfer by the equation $L = \frac{2\pi}{q}$), we have:

$$\tau = \frac{L^2}{2D} = \left(\frac{2\pi}{q}\right)^2 \cdot \frac{1}{2D} = \frac{2\pi^2}{q^2 D} \tag{10.14}$$

Similarly for diffusion confined to one dimension, the system behaves according to:

$$\langle x^2 \rangle = 2F\sqrt{t} \tag{10.15}$$

Making the same substitution, this equation gives:

$$\tau = \left(\frac{L^2}{2F}\right)^2 = \left(\frac{2\pi}{q}\right)^4 \cdot \frac{1}{4F^2} = \frac{4\pi^4}{q^4 F} \tag{10.16}$$

Taking the log of each of these equations gives:

$$\begin{aligned} \log(\tau) &= \log\left(\frac{2\pi^2}{q^2 D}\right) = \log\left(\frac{2\pi^2}{D}\right) + \log\left(\frac{1}{q^2}\right) \\ &= \log\left(\frac{2\pi^2}{D}\right) - 2\log(q) = -2\log(q) + \text{Const} \end{aligned} \tag{10.17}$$

for the case of free diffusion and :

$$\begin{aligned} \log(\tau) &= \log\left(\frac{4\pi^4}{q^4 F}\right) = \log\left(\frac{4\pi^4}{F}\right) + \log\left(\frac{1}{q^4}\right) \\ &= \log\left(\frac{4\pi^4}{F}\right) - 4\log(q) = -4\log(q) + \text{Const} \end{aligned} \tag{10.18}$$

for the case of confined diffusion. Both of these results, plotted as $\log(q)$ as a function of $\log(\tau)$ results in a straight line. The slope of this line varies according to the diffusion type

(-2 for free diffusion and -4 for confined 1D diffusion). The y-intercept in each case is a constant determined by the diffusion coefficient of the system. Once the diffusion type is known, a relatively straightforward way to determine the diffusion coefficient is to plot τ as a function of $\frac{1}{q^2}$ or $\frac{1}{q^4}$ (whichever is appropriate). The slope of the resulting line is inversely related to the diffusion constant as follows for free diffusion:

$$\tau = \left(\frac{2\pi^2}{D}\right)\left(\frac{1}{q^2}\right) = m\left(\frac{1}{q^2}\right) \Rightarrow D = \frac{2\pi^2}{m} \tag{10.19}$$

and as follows for confined diffusion:

$$\tau = \left(\frac{4\pi^4}{F}\right)\left(\frac{1}{q^4}\right) = m\left(\frac{1}{q^4}\right) \Rightarrow F = \frac{4\pi^4}{m} \tag{10.20}$$

10.3 Dynamic Light Scattering for Particle Sizing

Dynamic light scattering (DLS), also known as quasi-elastic light scattering (QELS) or photon correlation spectroscopy (PCS) is a technique analogous to XPCS in the visible regime. Dynamic light scattering is commonly used to determine the size of particles. The lower limit of resolution for DLS is typically considered around 2nm and the highest concentration limit is 0.002%. DLS works because intensity fluctuations are smooth and non-random. Particles are confined to move during finite periods of time. Because they don't move very quickly, particle positions are nearly the same from frame to frame and as a result, intensity doesn't fluctuate rapidly.

The diffusion coefficient can be extracted directly from the decay exponent on the autocorrelation function. Inverting the equation for the diffusion rate, the particle diameter can be found as:

$$d_H = \frac{k_B T}{3\pi\eta D} \tag{10.21}$$

The hydrodynamic diameter, d_H, is the diameter of a hard sphere with the observed diffusion rate through the solvent medium. It is not necessarily the same as the diameter of the dry particles because it depends on the surface structure, hydration of the particles, ion concentration, and many other factors.

During particle-sizing measurements, it is highly important that an accurate temperature is known because correct analysis of the autocorrelation functions and subsequent information about the sample requires knowing the viscosity of the medium under study. Viscosity is a quantity which is highly temperature-dependent. In addition, the temperature of a system needs to be stable so as to eliminate convection currents and any subsequent disturbances to particle diffusion and to maintain as much sample homogeneity as possible.

Observing the autocorrelation function for particles diffusing through a medium can provide a couple important pieces of information. The location of the first significant decay in the function indicates particle size (since the decay rate is related directly to the diffusion coefficient). Secondly, the slope of the decay indicates a quantity known as sample polydispersity. Polydispersity is an indicator of how homogeneous the particle sizes are. Assuming that the particles are monodisperse, with only small variations in size, the autocorrelation function should decay quickly. For polydisperse samples, or particles with a large spread in sizes, the autocorrelation function will decay more slowly and may exhibit features other than a single sharp drop.

There are a number of different methods for analyzing autocorrelation functions to extract particle sizing information. The first, and most basic algorithm, known as cumulants analysis fits a single decay function. Non-negative least squares (NNLS) or the CONTIN algorithms fit multiple exponential decays and allow for a wide particle size distribution.

The cumulants algorithm fits a single exponential decay (assumes single particle

size):

$$G(\tau) = \frac{\langle I(t_0)I(t_0+\tau)\rangle}{\langle I(t_\infty)\rangle^2} = B + Ae^{-2\Gamma\tau} \tag{10.22}$$

For a polydisperse sample:

$$G(\tau) = A[1 + Bg_1^2(\tau)] \tag{10.23}$$

where g_1 is a sum of exponential decays:

$$g_1(\tau) = e^{-\Gamma\tau}\left[1 + A\tau^2 + B\tau^3 + \cdots\right] \tag{10.24}$$

Chapter 11

Liquid Surfaces and Thin Films

11.1 Nanostructures

Nanostructures are materials which have at least one characteristic dimension in the length range $\sim 1 - 100$ nm, thus those particles which are made up of $\sim 1,000 - 1,000,000,000$ atoms. Nanomaterials are widely studied for their unique characteristics and properties, optical, magnetic, electronic, and others. They are heavily influenced by their size and shape. While two atoms of the same material behave quite the same, just as any two bulk samples of the same material are expected to have similar properties, two nanostructures of the same material, of slightly different dimensions, can have drastically different properties. A large contributing factor to these unique properties is the existence of surface effects due to the very large ratio of surface atoms to bulk atoms contained within nanomaterials. Typically, in most materials, surface effects may be neglected. As a result of these amongst other unique effects, the emerging field of nanotechnology is dedicated to determining the properties and potential uses of these highly customizable materials.

In general, there are two main approaches which can be taken to create nanostruc-

tured samples. In the top-down approach, the starting point is bulk matter. This matter is broken down into smaller and smaller pieces until particles of the desired dimensions are reached. Alternatively, in the bottom-up approach, the fundamental atomic and molecular building blocks are individually assembled into the required system. While hybrid top-down-bottom-up and bottom-up-top-down approaches are also feasible, this categorization typically applies to most nanosystems.

Nanoparticles are quasi-0-dimensional particles (typically spherical), for which all relevant dimensions are on the order of nanometers. Nanocrystallites are nanoparticles with a clearly ordered arrangement of atoms. Nanorods, nanotubes, and nanowires are all names for quasi-1-dimensional structures which have one dimension at least an order of magnitude greater than the others. Similarly, nanodisks, thin films, and monolayers represent a quasi-2-dimensional phase of matter. Monolayers and other such similar structures are the subject of much study because in addition to the unique properties exhibited by their constituent nanoparticles, electronic coupling between the particles can also influence their physical behaviors.

11.2 Introduction to Monolayers

A monolayer is a type of material characterized by having a thickness of only one molecule or particle. Due to a phenomenon known as self-assembly discussed shortly, monolayers can easily be formed on top of a liquid surface (the liquid being known as the "subphase"). Such a monolayer is known as a Langmuir film. From here, they can be studied either *in situ* on the liquid surface or be transferred to a solid substrate for further study or characterization. When a film is created at the liquid-air interface and is transferred to a solid substrate, it is known as a Langmuir-Blodgett film.

The easiest type of monolayer to discuss and illustrate is that formed by am-

phiphilic (surfactant) macromolecules such as lipids. This type of molecule consists of two distinguishing features: a hydrophilic ("water-loving") head and a hydrophobic ("water-fearing") tail group. When placed in contact with water, lipids tend to orient such that the head group is touching the liquid surface, with the tail group oriented away from the liquid as much as possible. The only place where it is possible for the hydrophobic tail to be completely out of contact with water is at the liquid surface. As a result, lipids placed in contact with water will tend to align themselves along the liquid surface, forming a monolayer by the process of self-assembly.

Only certain types of molecules are able to form monolayers. In the case of amphiphilic molecules, ones with too short of a hydrophobic tail or too strong of a polar group on the hydrophilic head will dissolve into the liquid subphase.

Monolayers are commonly formed using a piece of equipment known as a Langmuir-Blodgett (LB) trough. An LB trough consists of a shallow reservoir for water (or other liquid subphase), and a set of one or multiple movable barriers to adjust the surface area of the trough.

One of the most important characteristics of a monolayers is its surface pressure, as this value can provide information on how closely the molecules are packed and their subsequent dynamics on the liquid surface. Commonly, a plot is made of surface pressure as a function of surface area as the barriers of an LB trough compress the monolayer. Since the variable in this case is the surface area, the temperature remains fixed and the corresponding plot is known as an "isotherm."

11.3 Self-Assembly

The process of self-assembly involves the spontaneous association of molecules or particles into a specific geometric arrangement as the system reaches thermodynamic

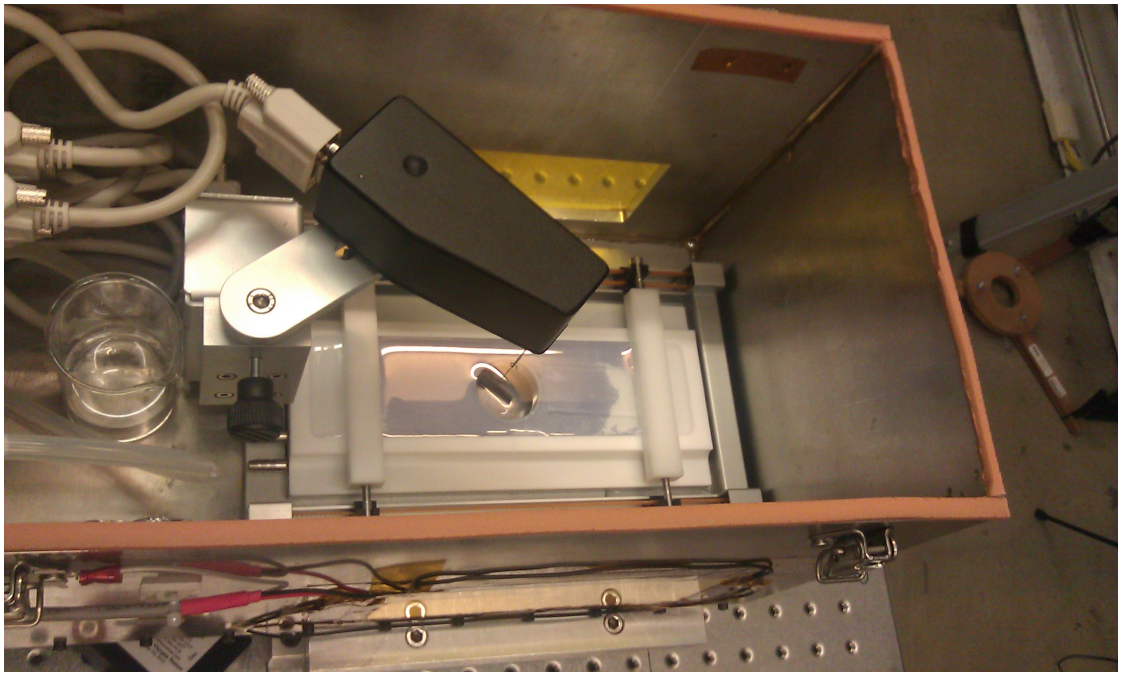

Figure 11.1: A Langmuir-Blodgett Trough with Au nanoparticle monolayer inside barriers

equilibrium. The particular variety of 2-dimensional self-assembly we are concerned with here at the liquid surface can be grouped under the heading of interfacial assembly since it occurs at the interface between liquid and gaseous phases of matter. A surface layer at this interface exhibits different properties than the bulk media on either side. In general, for electrically neutral molecules or particles, interfacial forces are relatively weak so the corresponding surface layer showing these unique properties may be only one or two layers thick. However, in the case of charged particles and correspondingly strong forces, the surface layer may be much larger.

Molecules at the surface of a liquid are less stable than those in the bulk because they experience unequal forces on various sides, as opposed to the isotropic forces acting on molecules in bulk. As a result, the interface acts to minimize the surface area, or consequently the number of particles exposed to the air. Surface tension is the force resulting from this tendency for molecules to be associated with the bulk liquid rather

than at the surface. As a result, there is no such thing as the surface tension of a given liquid or substance. Rather, surface tension must be described for a substance *at a given interface*, with the other substance at this interface being specified. Surface tension is measured perpendicular to the interface, and therefore has units of force per unit length. It can also represent the amount of work required to increase the surface area of a given interface by a unit area. As a result, this tension acts to restore the surface to a flat configuration in which its energy is minimized.

A monolayer is the primary self-assembled aggregate at the liquid-air interface because the interfacial thickness is on the same order as the size of the colloidal particles which frequently assemble at this boundary layer. Once a particle is adsorbed into the interface, the boundary layer serves as a potential well in which intermolecular forces confine their interplay. It is less favorable for the particles to interact through either of the surrounding phases than within the plane of the interface. The classes of molecules or particles which are able to form self-assembled monolayers are typically divided into three categories: amphiphilic, those with functional groups, and nonamphiphilic.

Metallic nanoparticles are often coated in surface ligands (generally fatty acids such as oleic acid or alkanethiol groups). These molecules serve multiple purposes: first, they provide particle stabilization to prevent aggregation into large clusters of particles. Additionally, nanoparticles which would not typically form monolayers on their own are often coated with surfactants, polymers, or other amphiphilic molecules to give them hydrophobic properties. As a result, such nanoparticles are widely used in studies of self assembled monolayers (SAMs).

11.4 Monolayer Formation

Since monolayers are self-assembled at the water subphase surface, it is critically important that the liquid surface be clean. Any contaminants can drastically affect the dynamic properties of the monolayer. As a result, prior to the formation of a monolayer, the subphase must be cleaned within the LB trough. A cleaning procedure is typically performed by sweeping the compression barriers across the liquid surface to minimize the surface area by bringing the contaminants close together. A glass capillary tube attached to a pump is brought in close proximity to the surface until the suction is sufficient to drive a small amount of liquid up the capillary (but without touching the surface and risking the introduction of further contaminants). The surface is cleaned in this fashion by alternately "sucking" the surface of the water clean at various points until the surface pressure remains constant through several sweepings of the barriers back and forth. Specific solvents may also be spread across the liquid surface to trap contaminant surfactant molecules and subsequently removed to "wash" the subphase surface.

The particles used to form a monolayer must be applied to the subphase layer in solution. The solvent used to dissolve the particles has the following requirements: it must dissolve a suitable amount of monolayer material, it must not chemically react with this material or dissolve into water, and it must evaporate in a short period of time, thereby leaving the particles on top of the liquid surface without residual solvent. Common solvents include n-hexane, cyclohexane, chloroform, and hexadecane. Drops of the particle/solvent solution are applied to the subphase by touching droplets to the liquid surface from a syringe, without directly touching the syringe to the surface and risking contamination. When the solution is applied to the liquid subphase, the solvent spreads across the liquid surface to form a thin film, with the particles approximately equally distributed. As the solvent evaporates, particles become trapped at the liquid-air

interface and self-assemble via interparticle forces and interactions.

11.5 Isotherm Characteristics

Monolayers represent a 2-dimensional form of matter since they are only nanometers thick. However, they undergo very similar phase transformations to their three-dimensional counterpart matter. As a result, monolayer phases are monitored by tracking surface pressure as a function of area, the equivalent of a pressure-volume diagram for bulk matter. After a monolayer has been formed, its characteristics can be modified by adjusting the surface area available to the particles. As the surface area of the trough available to the monolayer is decreased, the molecules move from a "gaseous" spread-out phase, to a "liquid" phase in which they are in closer contact. This transition is marked by a slight increase in the surface pressure. In both the gaseous and liquid phases, the polar tail groups of the molecules are in contact with the subphase liquid. This increase is followed by a horizontal region in which the surface pressure evens out as the hydrophobic tails are "lifted" from the liquid surface (prior to this surface area transition, they are spread out along the surface). An abrupt transition to higher surface pressure marks a phase change into an ordered solid arrangement of molecules, much like a crystal. If the surface area is decreased yet further, the monolayer collapses as molecular layers buckle and fold on top of each other, forming disordered multilayers. This collapse transition is marked by a sharp drop in surface pressure. Particles or molecules with longer tail groups exhibit a much higher collapse pressure.

While in the spread-out gaseous phase, monolayers follow a modified version of the ideal gas law:

$$\Pi A = NkT \tag{11.1}$$

where Π is the surface pressure, measured in units mN/m, A is the area occupied by the particles, and N, k, and T are as usual, the number of particles, Boltzmann's constant, and temperature, respectively.

In certain special cases, particularly depending on the length of the tail groups of monolayer-forming fatty acids, direct gas to solid phase transformations can be achieved with no intermediate phase, similar to the deposition (opposite of sublimation) of carbon dioxide gas into a solid as temperature is reduced at atmospheric pressure.

Monolayers show signs of nucleation and growth processes commonly seen in the generation of crystalline materials. As the surface area available to the monolayer constituent particles is decreased (and the surface pressure subsequently increases), "islands" of ordered particles begin to form and coalesce. A quantity known as the equilibrium spreading pressure (ESP) is the pressure that is spontaneously generated on the liquid surface when a crystalline solid material is brought into contact. The phase of a monolayer can be determined by comparison of its surface pressure with a previously known ESP value for the substance. A solution of particles will continue to spontaneously spread after being applied to the liquid surface until the ESP is reached. As this limit is reached, the monolayer takes on a crystalline phase.

11.6 Transfer to a Solid Substrate

The Langmuir-Blodgett technique is a process by which monolayers can be transferred from the liquid surface to a solid substrate. When a hydrophilic surface (such as a clean glass slide) is immersed into the liquid subphase, the liquid wets the substrate surface. As the slide is removed and the wetting contact line is moved across the surface, a monolayer is deposited on the slide such that the hydrophilic molecular heads are loosely bound to the hydrophilic substrate surface. This process requires a thin film

of water to remain in between the substrate and monolayer, but this layer can later be evaporated away.

11.7 Surface Pressure Measurements

The surface pressure of a monolayer is often measured by a device known as a Wilhelmy plate. A Wilhelmy plate is a small rectangle of a hydrophilic substance which is hung partially immersed below the liquid subphase in a LB trough, the force on which is monitored. Surface tension and gravity act downwards on such a plate, while buoyancy acts upward. Surface tension acts on the plate because its surface is at least partially wetted, causing the formation of a meniscus. The total force can be given by:

$$F = \rho_p glwt + 2\gamma(t+w)\cos(\theta) - \rho_L gtwh \tag{11.2}$$

where l, w, and t are the dimensions of the plate, h is the submerged depth, ρ_p is the density of the plate material, ρ_L is the density of the liquid, g is the gravitational constant, and θ is the contact angle the wetted surface makes with the plate.

Assuming that the plate is submerged to a constant depth, the change in the measured force can be given by:

$$\Delta F = \Delta\gamma \cdot 2(t+w) \tag{11.3}$$

Since the force balance can be zeroed, the surface pressure is then given by the change in the surface tension measured:

$$\Pi = -\Delta\gamma = -\frac{\Delta F}{2(t+w)} \tag{11.4}$$

Despite its ease of use, one of the disadvantages to the Wilhelmy plate method of surface

pressure measurement is that the contact angle must be known and unchanged. Typically, this is not a problem because the plate is fully wetted before being submerged into the liquid subphase; thus the contact angle is constant and approaches 0. However, if during the course of an experiment, monolayers are deposited onto the plate surface, then the value of θ can change. Additionally, the presence of the plate can perturb the formation of the monolayer on the subphase surface; particularly if the plate is placed asymmetrically with respect to the moving barriers of the LB trough, it can disrupt compression and flow of the molecules as they are compressed or expanded.

A less common alternative to the Wilhelmy plate is using a device known as a Langmuir balance. Pressure measurements using the Langmuir balance adopt a differential technique; the balance itself is a barrier which separates a clean water surface from the monolayer and measures the force on the partition between these two regions. Since the surface pressure of water is well known, it is relatively straightforward to obtain the pressure of the monolayer phase given this differential force measurement.

Chapter 12

Jamming and Ordering in Quasi-2D Self-Assembled Nanoparticle Monolayers

12.1 Abstract

We experimentally probed the interparticle dynamics of iron oxide nanoparticle thin films self-assembled at the water-air interface. Upon drop-casting on a water surface in a Langmuir-Blodgett trough and subsequent lateral compression, iron oxide nanocrystals coated in hydrophobic oleic acid ligands self-assemble into a relatively uniform quasi-2-dimensional monolayer. Utilizing X-ray Photon Correlation Spectroscopy (XPCS), we measured the characteristic relaxation time of in-plane interparticle dynamics as a function of film age through both second-order and two-time autocorrelation analysis. Stretched exponential fitting of our data yielded exponents indicating a jammed system. Films subject to a lower lateral surface pressure underwent a large-scale unjamming event, while those at higher pressure underwent smaller avalanches and showed clear

signs of aging in both the relaxation time and exponent. Despite the interesting jamming signatures and both spatial and temporal heterogeneity seen in these samples, the structure factor and overall ordering remain the same over the sample lifetime. Our early characterization paves the way for future studies of this richly complex nanoscale system.

12.2 Scientific Background

Beginning in the late 1800s, Lord Rayleigh hypothesized from experimental observations that given enough surface area, a droplet of oil spread across water forms a molecular monolayer [3]. Further work by Irving Langmuir and Katharine Blodgett transformed this new field of study from an observational curiosity into a technique for creating and extracting films of monolayer thickness [4, 5]. Now, nearly a century later, as technological developments have progressed on increasingly smaller length scales, the Langmuir-Blodgett technique, used to produce and transfer nanoscale thin films, has flourished with further applications and the introduction of engineered nanoparticles [2, 6, 7, 8, 9, 10, 11, 12, 13, 14, 15, 16, 17, 18, 19]. These developments have transformed the liquid-air interface into a veritable playground for studies involving states of matter and phase changes in quasi-2-dimensional (quasi-2D) systems.

Recent advances in nanoscale measurement techniques, including Atomic Force Microscopy (AFM), [20, 14, 21] Scanning Electron Microscopy (SEM) [11, 15, 22], Transmission Electron Microscopy (TEM) [23, 14], and X-ray Diffraction (XRD) [24, 25, 26], have allowed for engineered films with on-demand electrical, magnetic, and optical properties for technological applications [27]. Such films are finding their way into lightweight, flexible electronics [28], mirrors, sensors, antennas [10], and liquid metal batteries [29], among many other technologies. However, the continued success of monolayers and nanoscale-thin films in technological applications requires more

thorough research methods that allow for characterization of mechanical properties, necessitating examination of both the static structure and dynamics in these systems.

Experimental techniques for measuring the dynamics of ultrathin films comprised of nanoparticle building blocks has taken longer to develop than those for measuring the static structure of the same systems. Such studies have become particularly prevalent in recent years due to the dramatic increases in both spatial and temporal resolution afforded by coherent X-ray beamlines at synchrotron sources [30]. Along with the ability to study *in situ* dynamics came the capacity to observe processes such as glass formation, relaxation, collective dynamics, and jamming in real time [31, 32, 8, 33]. During jamming, an arrangement of particles undergoes structural arrest, transforming from a colloidal suspension into a disordered solid characterized by a yield stress, as the phase space no longer supports macroscopic motion [34]. The recent popularization of the topic of jammed particles as common to our everyday lives - from walking across sand to colloids used in cooking or cleaning - has led to increased interest in studying jamming on the nanoscale for technological applications [20]. Since the overall order parameter does not change between liquid and jammed states, such systems must be characterized by a method other than those conventionally used to study states of matter [35]. Most studies regarding the jamming transition in particle systems focus on 3-dimensional systems [31, 36, 37, 38, 39, 40, 41]. However, technological applications require increasingly thinner and more uniform materials, quickly approaching the 2D limit.

In this work, we examine the effects of surface pressure and dimensionality on jamming and collective motion by studying a quasi-2D system through a combination of the Langmuir-Blodgett technique with X-ray Photon Correlation Spectroscopy (XPCS) (see Figure 12.1). These techniques enable us to determine the effect of individual nanoscale particle dynamics on the macroscopic film structure and dynamics. We

present some of the first direct measurements of interparticle dynamics of nanoparticle monolayers at the water-air interface.

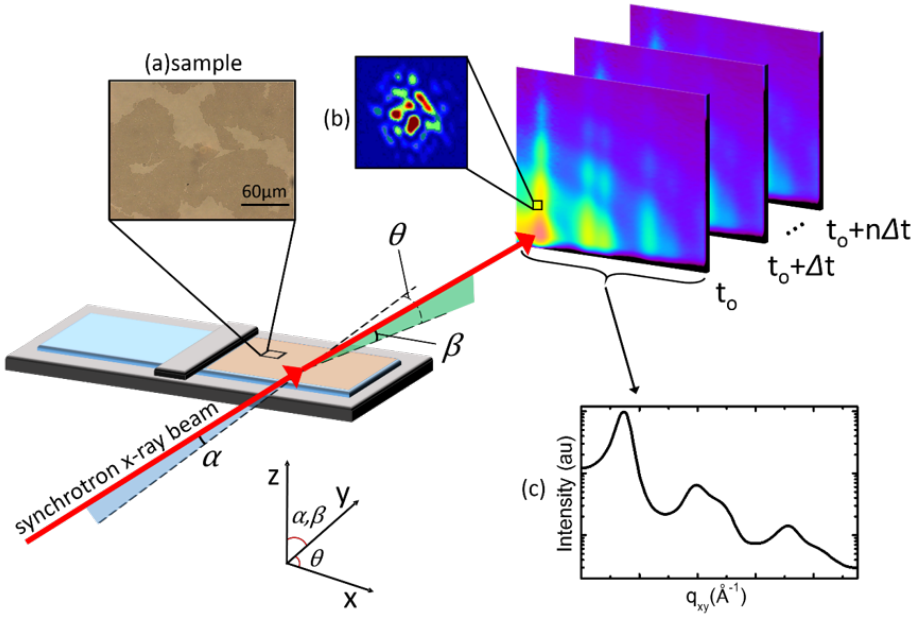

Figure 12.1: Geometry of liquid surface scattering setup. XPCS measurements were taken at the position of the first order Grazing Incidence Diffraction (GID) peak (a) inset showing optical microscopy image of film, (b) representative speckle pattern measured in XPCS superimposed on GID peak, and (c) line integral of 2D diffraction pattern showing 1st through 5th order GID peaks.

12.3 Results and Discussion

Figure 12.2a shows an optical microscopy image of a 20nm iron oxide thin film on a liquid surface, while Figure 12.2b shows a scanning electron microscopy (SEM) image of this film transferred onto a silicon substrate using the Langmuir-Schaefer technique, which preserves the interparticle structure [42]. These images show the existence of grain boundaries in the films at length scales differing by two orders of magnitude. These grain boundaries are evidence of a jammed system, with dynamics confined to collective motion of individual grains [7, 43]. Static images alone, however, cannot illuminate the

underlying dynamics of the system and so we turn our attention to other measurement techniques.

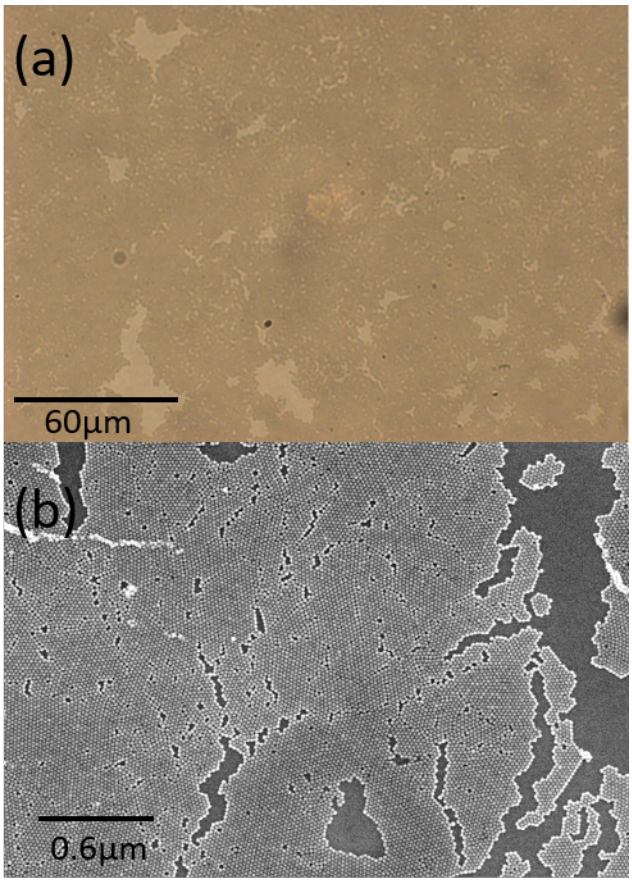

Figure 12.2: Grain boundaries across several orders of magnitude length scale suggesting jamming in (a) optical microscopy of film *in situ* on a liquid surface, and (b) Scanning Electron Microscopy of film transferred to silicon substrate via Langmuir-Schaefer transfer method.

We first discuss the general characteristics of several films compressed to varying initial surface pressures before focusing more closely on the details of one of the films (see Methods section for sample preparation). For a target pressure of 20mN/m, pressure measurements showed an initial sharp drop, followed by a smooth increase, gradually leveling out (Figure 12.3a). For target pressures of 30mN/m and 40mN/m, pressure measurements showed a similar sharp drop following compression, before monotonically and gradually leveling out. Both of these trends were pressure-dependent, reproducible

macroscale effects. The initial relaxations of pressure post-compression are indicative of out-of-equilibrium dynamics within the system [44]. We fit each of these pressure curves to a series of exponential decays, with the results shown in Table 12.1. We hypothesize that the compression process creates defects and point stresses that are able to rearrange once the barrier is fixed in position and film surface area is held constant and will explore this possibility later in conjunction with X-ray measurements.

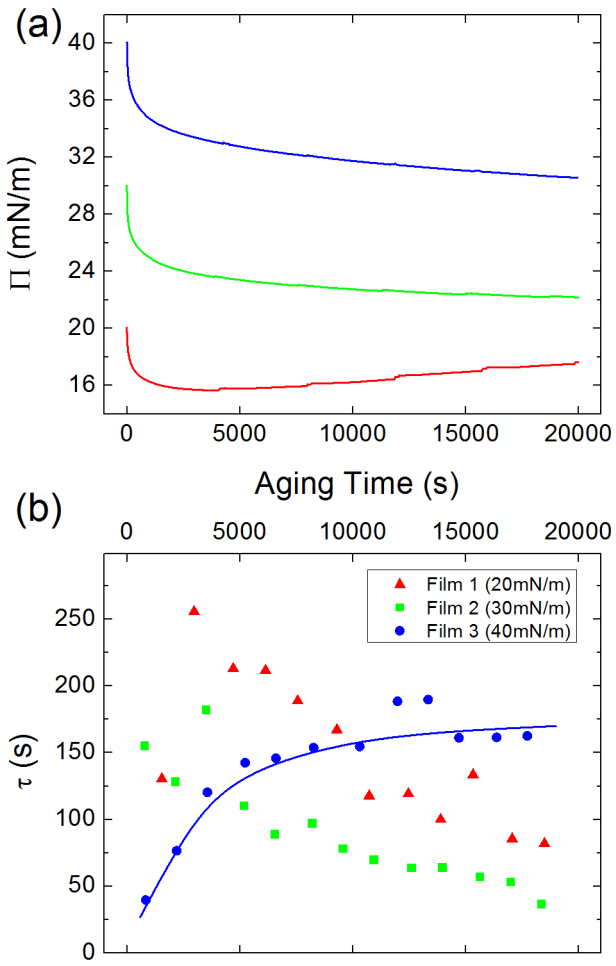

Figure 12.3: Surface pressure (Π) and characteristic relaxation time (τ) measurements for three different iron oxide thin films. (a) Pressure measurements were taken using a Wilhelmy plate and microbalance, showing reproducible trends. (b) Relaxation time measurements were calculated using XPCS technique. Film 3 shows clear signs of aging, as the relaxation times initially increase before leveling out (blue solid line provides guide to the eye).

Table 12.1: The pressure curves shown in Figure 12.3a were fit to the form $\Pi = ae^{-\frac{t}{\tau_1}} + be^{-\frac{t}{\tau_2}} + ce^{-\frac{t}{\tau_3}}$. τ_3 for film 1 is negative, corresponding to the long-timescale increase in Π.

	Film 1	Film 2	Film 3
$\tau_1(s)$	90	60	160
$\tau_2(s)$	1.2e3	1.7e3	2.1e3
$\tau_3(s)$	-1.3e5	3.5e5	2.4e5

Over the lifetime of each film, the interparticle spacing changed by less than 2Å, or 1% of the particle size, with both the particle size and spacing determined by the reciprocal space location of the first order Grazing Incidence Diffraction (GID) peak. Similarly, the width of the GID peak, indicating the level of disorder in the system, varied by less than 15% in all cases. The relative stability of the surface pressure following the initial drop, combined with the consistency of the structure factor, seem to indicate that the films quickly reach a static equilibrium without an overall change in particle ordering. To verify this, we more closely examined the interparticle dynamics using XPCS in one of the first applications of XPCS to liquid surface monolayers. To gain information on film dynamics, it is useful to analyze the second order intensity autocorrelation function, which is determined according to the formula:

$$g_2(\Delta t) = \frac{\langle I(t)I(t+\Delta t)\rangle_t}{\langle I(t)\rangle_t^2} \tag{12.1}$$

and fit to the form:

$$g_2(\Delta t) - 1 = b\left[e^{-\left(\frac{\Delta t}{\tau}\right)^{\beta}}\right]^2 \tag{12.2}$$

where $I(t)$ is the beam intensity, Δt is the variable time delay, b is the Siegert factor, τ is the characteristic relaxation time, and β is the stretching or compressing exponent, with $0 < \beta < 1$ indicating a glassy system, $\beta = 1$ indicating Brownian diffusion, and $\beta > 1$ indicating a jammed system [45, 46, 47]. The relaxation times were calculated for each

of the samples, keeping the exponent β free and minimizing chi-squared. Figure 12.3b shows the relaxation times, which are on the order of τ_1, shown in Table 12.1. For both Films 1 and 2, the relaxation time decreases over the lifetime of the film, indicating that the interparticle motion is speeding up. Film 3 shows the opposite behavior, with the relaxation times initially increasing and gradually leveling off. Since the XPCS technique probes only the local structure of the illuminated region of the sample, we can conclude that there exists both a spatial and temporal heterogeneity in the dynamics within the samples. This is in contrast with the pressure measurements, which indicate smooth macroscale behavior. X-ray measurements indicate that the relaxation time varies over a length scale of at least 40μm, the lateral distance the sample is moved between scans, and a timescale of at least 700s, the time between subsequent scans. These observed length and timescales for dynamic heterogeneity are consistent with the interpretation of the dynamics as collective motion at the grain boundaries (see Figure 12.2).

We extracted the exponent β from the fit of Equation 12.2 to the intensity auto-correlation function in order to determine the degree of jamming in our system, and the results, along with guides to the eye to elucidate the underlying trends, are plotted in Figure 12.4. As the lateral surface pressure on the film increases, so does the average value of β, indicating an increase in the degree of jamming in the system with pressure. Additionally, in the cases of Films 1 and 2 (20mN/m and 30mN/m, respectively), the exponent undergoes a significant drop over the lifetime of the film, suggesting a large-scale transition from jammed to glassy state [37]. The sample at 40mN/m does not exhibit this same signature, perhaps indicating that higher film pressures lead to a jammed state with local rearrangements but no bulk glass transition.

Although both lateral pressure and structure factor measurements point towards a quasi-static system, it is clear from relaxation time and exponent fitting that the system exhibits interesting interparticle dynamics and collective motion. We take a closer look at

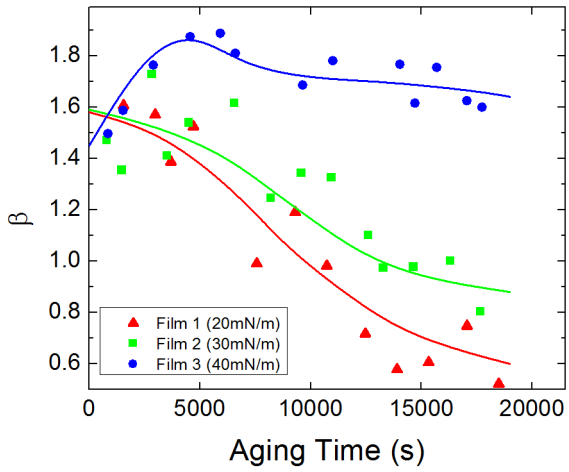

Figure 12.4: Stretching exponent (β) as a function of film age for three different films. Solid symbols represent data; solid lines are guides to the eye to reveal overall trends. The average exponent increases as initial film pressure increases. Films 1 and 2 show an overall trend of decreasing exponent as film age grows. This is indicative of a reduction in dimensionality. Film 3 shows the most constant exponent, indicating little change in its jamming state.

Film 3, for which the stretching exponent is most constant, indicating little macroscopic change, in order to observe dynamics in a consistently jammed system.

Figure 12.5 shows the autocorrelation functions, $g_2(\Delta t)$, for Film 3 at varying film ages, where the dashed lines represent the fits of the stretched exponential model (Equation 12.2) to $g_2(\Delta t)$ (data points). For earlier film ages, the relaxation time (Figure 12.3b) increased dramatically before roughly leveling off for later ages. This behavior is indicative of aging in the system as the interparticle motion slows down. Brownian diffusion dictates that the time for a particle to transverse a mean squared distance of $\overline{x^2}$ is given by:

$$t = \frac{1}{2}\overline{x^2}q^2\tau \tag{12.3}$$

where τ is the characteristic time for interparticle diffusion. Given an approximate relaxation time of 100 seconds, as shown in Figure 12.3b, it would take the particles

on the order of 10^4 seconds to traverse a distance of 100nm, the lower limit on the size of the grains. This is on the order of the observed aging time, indicating that the aging is intrinsic to the jammed state with diffusion along the grain boundaries rather than due to a dissipation of energy following the barrier compression. The speed of barrier compression is approximately six orders of magnitude faster than the interparticle diffusion rate. A similar early-age increase is visible in the stretching exponent of this film, as seen in Figure 12.4. The exponent changes from a value of 1.5, the theoretically predicted and experimentally verified jamming limit in 3-dimensions [40, 48, 49, 41], to around 1.8. This increase in exponent corresponds with a reduction in the dimensionality of the jammed system as the particles become more closely confined.

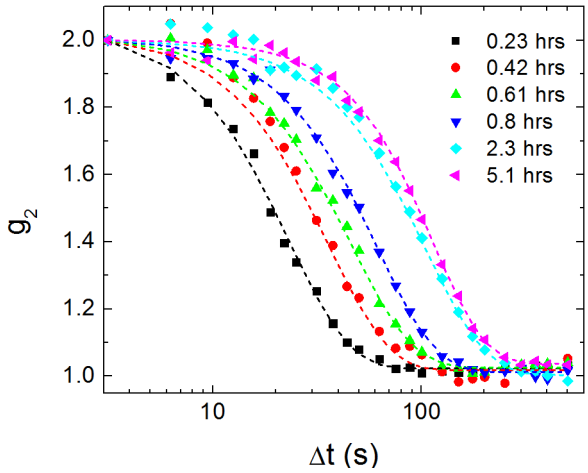

Figure 12.5: Normalized autocorrelation function g_2 for selected film ages of Film 3 at wave vector transfer $q = 0.33\text{nm}^{-1}$. Dashed lines are the result of fits to Equation 12.2.

In addition to the single-time autocorrelation analysis discussed above, we also employed the two-time intensity autocorrelation function given by:

$$g_{2,2-time}(\Delta t_1, \Delta t_2) = \frac{\langle I(t+\Delta t_1) I(t+\Delta t_2)\rangle_t}{\langle I(t)\rangle_t^2} \tag{12.4}$$

where Δt_1 and Δt_2 are two time delays encompassing the same time range. The results are shown in Figure 12.6. As the film ages, the relaxation time, τ, increases on average, as

shown by the width of the high-intensity region. However, the inset shows a representative point at which the two-time autocorrelation function pinches off. This shape is indicative of a sudden and discontinuous rearrangement of particles followed by a quick return to the original relaxation time. Such rearrangements are a signature of local avalanches in a jammed system [50], as macroscopic changes would appear in measurements of surface pressure or stretching exponent. We verified that this sudden change in the two-time correlation is not due to variable beam intensity and is visible at all measured q-values, meaning that the rearrangement happened across all length scales.

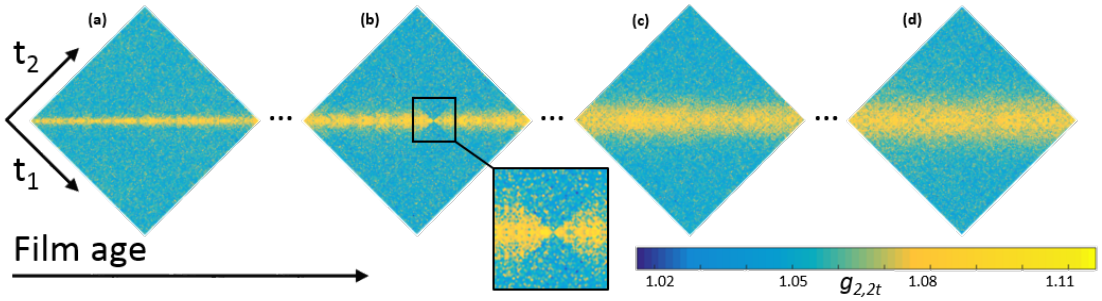

Figure 12.6: Colormap of two-time autocorrelation for various film ages. Inset shows a pinch point corresponding to a dramatic structural rearrangement of the probed sample region in the image for an age of (a) 0.23-0.42 hrs, (b) 0.61-0.8 hrs, (c) 1.3-1.45 hrs, (d) 3.9-4.1 hrs.

In conclusion, we present evidence of jamming in quasi-2D nanoparticle thin films. At lower surface pressures, the films undergo a macroscopic unjamming process, while for higher surface pressures, the films undergo smaller avalanche effects but no bulk transition. In all cases, both the overall ordering and the structure factor remain unchanged, indicating that the dynamics are confined to grain boundaries. The interparticle relaxation times show little consistency, evidence that these films are a rich system with hidden variables at inaccessible length and timescales. While our conclusions may vary depending on the chemical makeup of the nanoparticles and their associated ligands, our experiments suggest a method for further characterization as we have shown that it is possible to directly measure interparticle dynamics, including abrupt events, in liquid-air

interface monolayers. Future directions could include varying the ligand concentration to measure its effect on the jamming transition. Such monolayers represent a complex system that merits further study for potential uses in engineering and technological applications.

12.4 Methods

For these studies, we utilized organic-soluble monodisperse spherical iron oxide nanocrystals (Fe_3O_4) (www.oceannanotech.com), 20nm in diameter with a size distribution ¡5% in powder form. The oleic acid coating on these particles creates a hydrophobic coating and prevents aggregation [51]. We suspended this powder in chloroform to create a solution with a concentration of 0.5mg/mL. We drop-cast this solution onto a clean water surface in an 80 cm^2 Langmuir-Blodgett trough. After chloroform evaporation and system equilibration, the particles were spread to an approximate surface area coverage of 60%. We monitored the in-plane surface pressure throughout our XPCS measurements using a Wilhelmy plate and microbalance.

Following sample deposition and equilibration, we laterally compressed the film in a continuous, constant-speed compression of 1cm^2/min to a peak surface pressure of approximately 20mN/m, 30mN/m, or 40mN/m for various samples, before fixing the barriers in position. We called this point $t = 0$ for the film age.

Dynamics experiments were performed at beamline 8-ID-I of the Advanced Photon Source (APS). Static measurements were taken at beamline 15-ID. Specifics on the beamline optics and beam coherence of 8-ID-I are presented elsewhere [52]. The experimental set-up was placed in reflection geometry (Figure 12.1) with an angle of incidence of $\alpha = 0.14^\circ$, below the critical angle for water at an incident X-ray beam energy of 7.35keV. The sample-detector distance of about 4 meters was sufficient to

generate X-ray speckle on the order of the pixel size to allow for maximal resolution.

XPCS frames were collected every $\sim$1 second, as dictated by the readout time of the detector (Princeton Instruments), while the maximum time delay for a single data set, 2400 seconds, was determined by considering the combined effects of beam stability and maximum exposure time of the sample. Beam stability was determined using a static reference sample, while maximum exposure time was determined by monitoring reflectivity for signs of sample damage. In between measurements, we moved the sample laterally by $40\mu m$, or twice the beam width, in order to minimize sample damage. Through repeated measurements in this manner, we were able to collect data on the sample for ages between 10^3 and 10^5 seconds.

In order to achieve a compromise between signal-to-noise and spatial resolution, we probed our sample over a wave vector range of $0.30\text{nm}^{-1} < q_x < 0.36\text{nm}^{-1}$, corresponding to the maximum of the static structure factor (first order GID peak) for a mean interparticle distance of $2\pi/q = 19\text{nm}$. Second-order intensity autocorrelation functions were calculated using XPCSGUI software designed for sector 8-ID at APS.

12.5 Acknowledgements

The authors thank the NSF for support under CAREER Award No. DMR-0956131. This research used resources of the Advanced Photon Source, a U.S. Department of Energy (DOE) Office of Science User Facility operated for the DOE Office of Science by Argonne National Laboratory under Contract No. DE-AC02-06CH11357. ChemMatCARS Sector 15 is supported by the National Science Foundation under the grant number NSF/CHE-1346572. BL and SSY thank University of Chicago MRSEC for support under the grant number NSF/DMR- 1420709.

Chapter 12, in part is currently being prepared for submission for publication

of the material. Leandra S. Boucheron, Jacob T. Stanley, Yeling Dai, Siheng Sean You, Christopher T. Parzyck, Suresh Narayanan, Alec R. Sandy, Zhang Jiang, Mati Meron, Binhua Lin, and Oleg G. Shpyrko. “Jamming and ordering in quasi-2D self-assembled nanoparticle monolayers”. The dissertation author was the primary investigator and author of this material.

Bibliography

[1] S. K. Sinha and D. K. Ross, "Self-consistent density response function method for dynamics of light interstitials in crystals," *Physica B+ C*, vol. 149, pp. 51–56, 1988.

[2] Y. Dai, B. Lin, M. Meron, K. Kim, B. Leahy, and O. G. Shpyrko, "A comparative study of Langmuir surfactant films: Grazing incidence x-ray off-specular scattering vs. x-ray specular reflectivity," *Journal of Applied Physics*, vol. 110, p. 102213, 2011.

[3] J. W. S. Rayleigh, "XXXVI. Investigations in Capillarity: The size of drops. The liberation of gas from supersaturated solutions. Colliding jets. The tension of contaminated water-surfaces," *The London, Edinburgh, and Dublin Philosophical Magazine*, vol. 48, no. 293, pp. 321–337, 1899.

[4] I. Langmuir, "The Constitution and Fundamental Properties of Solids and Liquids. II. Liquids.," *Journal of the American Chemical Society*, vol. 39, no. 9, pp. 1848–1906, 1917.

[5] M. C. Petty, *Langmuir-Blodgett Films: An Introduction*. New York: Cambridge University Press, 1996.

[6] B. D. Leahy, L. Pocivavsek, M. Meron, K. L. Lam, D. Salas, P. J. Viccaro, K. Y. C. Lee, and B. Lin, "Geometric Stability and Elastic Response of a Supported Nanoparticle Film," *Physical Review Letters*, vol. 105, p. 058301, July 2010.

[7] K. Schwenke, L. Isa, and E. Del Gado, "Assembly of nanoparticles at liquid interfaces: crowding and ordering.," *Langmuir*, vol. 30, pp. 3069–3074, Mar. 2014.

[8] J. W. Swan, J. L. Bauer, Y. Liu, and E. M. Furst, "Directed colloidal self-assembly in toggled magnetic fields," *Soft Matter*, vol. 10, no. 8, p. 1102, 2014.

[9] K. Chokprasombat, C. Sirisathitkul, and P. Ratphonsan, "Liquid-air interface self-assembly: A facile method to fabricate long-range nanoparticle monolayers," *Surface Science*, vol. 621, pp. 162–167, Mar. 2014.

[10] J. B. Edel, A. A. Kornyshev, and M. Urbakh, "Self-Assembly of Nanoparticle Arrays for Use as Mirrors, Sensors, and Antennas," *ACS nano*, no. Xx, 2013.

[11] C. Y. Lau, H. Duan, F. Wang, C. B. He, H. Y. Low, and J. K. W. Yang, "Enhanced ordering in gold nanoparticles self-assembly through excess free ligands.," *Langmuir*, vol. 27, pp. 3355–60, Apr. 2011.

[12] S. S. You, R. Rashkov, P. Kanjanaboos, I. Calderon, M. Meron, H. M. Jaeger, and B. Lin, "Comparison of the Mechanical Properties of Self-Assembled Langmuir Monolayers of Nanoparticles and Phospholipids," *Langmuir*, vol. 29, no. 37, pp. 11751–11757, 2013.

[13] S. Kinge, M. Crego-Calama, and D. N. Reinhoudt, "Self-assembling nanoparticles at surfaces and interfaces.," *Chemphyschem*, vol. 9, pp. 20–42, Jan. 2008.

[14] S. C. Glotzer, M. J. Solomon, and N. A. Kotov, "Self-assembly: From nanoscale to microscale colloids," *AIChE Journal*, vol. 50, pp. 2978–2985, Dec. 2004.

[15] B. A. Grzybowski, C. E. Wilmer, J. Kim, K. P. Browne, and K. J. M. Bishop, "Self-assembly: from crystals to cells," *Soft Matter*, vol. 5, no. 6, p. 1110, 2009.

[16] M. Grzelczak, J. Vermant, E. M. Furst, and L. M. Liz-Marzán, "Directed self-assembly of nanoparticles.," *ACS nano*, vol. 4, pp. 3591–3605, July 2010.

[17] D. Mishra, M. J. Benitez, O. Petracic, G. A. Badini Confalonieri, P. Szary, F. Brussing, K. Theis-Brohl, A. Devishvili, A. Vorobiev, O. Konovalov, M. Paulus, C. Sternemann, B. P. Toperverg, and H. Zabel, "Self-assembled iron oxide nanoparticle multilayer: x-ray and polarized neutron reflectivity," *Nanotechnology*, vol. 23, p. 055707, 2012.

[18] A. Böker, J. He, T. Emrick, and T. P. Russell, "Self-assembly of nanoparticles at interfaces," *Soft Matter*, vol. 3, no. 10, pp. 1231–1248, 2007.

[19] A. Ulman, "Formation and Structure of Self-Assembled Monolayers.," *Chemical reviews*, vol. 96, pp. 1533–1554, June 1996.

[20] J. Brujic, "Jammed particles, from sandy beaches to sunscreens," *Physics Today*, pp. 64–65, 2010.

[21] Y. Wang, P. Kanjanaboos, E. Barry, S. McBride, X.-M. Lin, and H. M. Jaeger, "Fracture and failure of nanoparticle monolayers and multilayers.," *Nano letters*, vol. 14, pp. 826–830, Feb. 2014.

[22] J. Polte, R. Erler, A. Thunemann, S. Sokolov, T. T. Ahner, K. Rademann, F. Emmerling, and R. Kraehnert, "Nucleation and growth of gold nanoparticles studied via in situ small angle X-ray scattering at millisecond time resolution," *ACS nano*, vol. 4, no. 2, pp. 1076–1082, 2010.

[23] K. Abe, T. Hanada, T. Yamaguchi, H. Takiguchi, H. Nagasawa, M. Nakamoto, and K. Yase, "Two-dimensional arrangement of silver nanoparticles on water surface," *Molecular Crystallography Liquid Crystals*, vol. 322, pp. 173–178, 1998.

[24] D. K. Schwartz, "Langmuir-Blodgett film structure," *Surface Science Reports*, vol. 27, pp. 241–334, 1997.

[25] B. Ruta, Y. Chushkin, G. Monaco, L. Cipelletti, E. Pineda, P. Bruna, V. Giordano, and M. Gonzalez-Silveira, "Atomic-Scale Relaxation Dynamics and Aging in a Metallic Glass Probed by X-Ray Photon Correlation Spectroscopy," *Physical Review Letters*, vol. 109, p. 165701, Oct. 2012.

[26] L. Zhang, R. He, and H.-C. Gu, "Oleic acid coating on the monodisperse magnetite nanoparticles," *Applied Surface Science*, vol. 253, pp. 2611–2617, Dec. 2006.

[27] M. Brust, D. Bethell, C. J. Kiely, and D. J. Schiffrin, "Self-assembled gold nanoparticle thin films with nonmetallic optical and electronic properties," *Langmuir*, vol. 14, no. 5, pp. 5425–5429, 1998.

[28] S.-C. Pang, M. A. Anderson, and T. W. Chapman, "Novel electrode materials for thin-film ultracapacitors: comparison of electrochemical properties of sol-gel-derived and electrodeposited manganese dioxide," *Journal of the Electrochemical Society*, vol. 147, no. 2, pp. 444–450, 2000.

[29] K. Wang, K. Jiang, B. Chung, T. Ouchi, P. J. Burke, D. A. Boysen, D. J. Bradwell, H. Kim, U. Muecke, and D. R. Sadoway, "Lithium-antimony-lead liquid metal battery for grid-level energy storage," *Nature*, vol. 514, pp. 348–350, Sept. 2014.

[30] D. H. Bilderback, P. Elleaume, and E. Weckert, "Review of third and next generation synchrotron light sources," *Journal of Physics B: Atomic, Molecular and Optical Physics*, vol. 38, pp. S773–S797, May 2005.

[31] L. Cipelletti and L. Ramos, "Slow dynamics in glassy soft matter," *Journal of Physics: Condensed Matter*, pp. 1–41, 2005.

[32] A. Amir, Y. Oreg, and Y. Imry, "On relaxations and aging of various glasses," *Proceedings of the National Academy of Sciences*, no. 2, pp. 1–10, 2012.

[33] S. Whitelam, E. H. Feng, M. F. Hagan, and P. L. Geissler, "The role of collective motion in examples of coarsening and self-assembly," *Soft Matter*, vol. 5, no. 6, pp. 1251–1262, 2009.

[34] A. J. Liu and S. R. Nagel, eds., *Jamming and rheology: constrained dynamics on microscopic and macroscopic scales*. London: Taylor & Francis, 2001.

[35] J. T. Rogers, K. Schmidt, M. F. Toney, E. J. Kramer, and G. C. Bazan, "Structural order in bulk heterojunction films prepared with solvent additives.," in *Advanced materials*, vol. 23, pp. 2284–2288, May 2011.

[36] M. Bellour, A. Knaebel, J. Harden, F. Lequeux, and J.-P. Munch, "Aging processes and scale dependence in soft glassy colloidal suspensions," *Physical Review E*, vol. 67, p. 031405, Mar. 2003.

[37] R. Mari, F. Krzakala, and J. Kurchan, "Jamming versus Glass Transitions," *Physical Review Letters*, vol. 103, p. 025701, July 2009.

[38] L. Mohan, R. Bonnecaze, and M. Cloitre, "Microscopic Origin of Internal Stresses in Jammed Soft Particle Suspensions," *Physical Review Letters*, vol. 111, no. December, p. 268301, 2013.

[39] D. Orsi, L. Cristofolini, M. P. Fontana, A. Fluerasu, and A. Madsen, "Slow dynamics in an azopolymer molecular layer studied by x-ray photon correlation spectroscopy.," *Physical Review E, Statistical, nonlinear, and soft matter physics*, vol. 82, p. 031804, Sept. 2010.

[40] L. Cipelletti, S. Manley, R. C. Ball, and D. A. Weitz, "Universal aging features in the restructuring of fractal colloidal gels.," *Physical Review Letters*, vol. 84, pp. 2275–2278, Mar. 2000.

[41] R. Bandyopadhyay, D. Liang, H. Yardimci, D. A. Sessoms, M. A. Borthwick, S. G. J. Mochrie, J. L. Harden, and R. L. Leheny, "Evolution of Particle-Scale Dynamics in an Aging Clay Suspension," *Physical Review Letters*, vol. 93, p. 228302, Nov. 2004.

[42] J. Stanley, Y. Dai, L. Boucheron, B. Lin, M. Meron, and O. Shpyrko, "Novel comparison of microscopy and diffraction techniques on the structure of iron oxide nanoparticle monolayers transferred by Langmuir-Schaefer method," *Review of Scientific Instruments*, vol. 86, no. 6, p. 063704, 2015.

[43] Y. Dai, B. Lin, M. Meron, K. Kim, B. Leahy, T. A. Witten, and O. G. Shpyrko, "Synchrotron X-ray studies of Rapidly Evolving Morphology of Self-assembled Nanoparticle Films under Lateral Compression.," *Langmuir*, vol. 29, pp. 14050–14056, Oct. 2013.

[44] B. Lin, D. G. Schultz, X.-M. Lin, D. Li, J. Gebhardt, M. Meron, and P. J. Viccaro, "Langmuir monolayers of gold nanoparticles," *Thin Solid Films*, vol. 515, pp. 5669–5673, May 2007.

[45] R. Borsali and R. Pecora, eds., *Soft Matter Characterization*. Dordrecht: Springer Netherlands, 2008.

[46] P. Falus, M. Borthwick, S. Narayanan, A. Sandy, and S. Mochrie, "Crossover from Stretched to Compressed Exponential Relaxations in a Polymer-Based Sponge Phase," *Physical Review Letters*, vol. 97, p. 066102, Aug. 2006.

[47] D. J. Durian, "Detecting and characterizing intermittency using higher-order intensity correlation functions," in *Photon Correlation and Scattering*, vol. 7, pp. 134–136, Optical Society of America, 2000.

[48] L. Cipelletti, L. Ramos, S. Manley, E. Pitard, D. A. Weitz, E. E. Pashkovski, and M. Johansson, "Universal non-diffusive slow dynamics in aging soft matter," *Faraday Discussions*, vol. 123, pp. 237–251, Jan. 2003.

[49] J.-P. Bouchaud and E. Pitard, "Anomalous dynamical light scattering in soft glassy gels," *The European Physical Journal E*, vol. 6, pp. 231–236, 2001.

[50] C. Sanborn, K. F. Ludwig, M. C. Rogers, and M. Sutton, "Direct Measurement of Microstructural Avalanches during the Martensitic Transition of Cobalt Using Coherent X-Ray Scattering," *Physical Review Letters*, vol. 107, p. 015702, June 2011.

[51] H. Duan, M. Kuang, X. Wang, Y. A. Wang, H. Mao, and S. Nie, "Reexamining the effects of particle size and surface chemistry on the magnetic properties of iron oxide nanocrystals: new insights into spin disorder and proton," *The Journal of Physical Chemistry C*, vol. 112, pp. 8127–8131, 2008.

[52] D. Lumma, L. B. Lurio, M. A. Borthwick, P. Falus, and S. G. J. Mochrie, "Structure and dynamics of concentrated dispersions of polystyrene latex spheres in glycerol: Static and dynamic x-ray scattering," *Physical Review E*, vol. 62, no. 6, pp. 8258–8269, 2000.

[53] D. J. Griffiths, *Introduction to Electrodynamics*. Upper Saddle River: Prentice Hall, Inc., 3rd ed., 1999.

[54] D. Attwood, *Soft X-Rays and Extreme Ultraviolet Radiation*. Cambridge: Cambridge University Press, 1999.

[55] B. J. Berne and R. Pecora, *Dynamic Light Scattering With Applications to Chemistry, Biology, and Physics*. Mineola: Dover Publications, Inc., 2000.

[56] B. P. Binks and T. S. Horozov, *Colloidal Particles at Liquid Interfaces*. Cambridge: Cambridge University Press, 2006.

[57] B. W. Carroll and D. A. Ostlie, *An Introduction to Modern Astrophysics*. San Francisco: Pearson Education, Inc., 2nd ed., 2007.

[58] J. A. Clarke, *The Science and Technology of Undulators and Wigglers*. Oxford: Oxford University Press, 2004.

[59] J. Daillant and A. Gibaud, eds., *X-Ray and Neutron Reflectivity*. Berlin: Springer-Verlag, 2009.

[60] P. J. Duke, *Synchrotron Radiation: Production and Properties*. Oxford: Oxford University Press, 2000.

[61] T. Ezquerra, M. Garcia-Gutiérrez, A. Nogales, and M. Gomez, eds., *Applications of Synchrotron Light to Scattering and Diffraction in Materials and Life Sciences*. Berlin: Springer-Verlag, 2009.

[62] S. P. Gubin, ed., *Magnetic Nanoparticles*. Weinheim: Wiley-VCH, 2009.

[63] J. Hao, ed., *Self-Assembled Structures: Properties and Applications in Solution and on Surfaces*. Boca Raton: CRC Press, 2011.

[64] P. Heitjans and J. Kaerger, eds., *Diffusion in Condensed Matter*. Berlin: Springer-Verlag, 2005.

[65] F. Hippert, E. Geissler, J. L. Hodeau, E. Lelievre-Berna, and J.-R. Regnard, eds., *Neutron and X-Ray Spectroscopy*. Dordrecht: Springer, 2006.

[66] D. Hukins, *X-Ray Diffraction by Disordered and Ordered Systems*. Oxford: Pergamon Press, 1981.

[67] R. Jenkins and R. Snyder, *Introduction to X-Ray Powder Diffractometry*. New York: John Wiley & Sons, Inc., 1996.

[68] H. Kausch and H. Zachmann, eds., *Characterization of Polymers in the Solid State II: Synchrotron Radiation, X-Ray Scattering and Electron Microscopy*. Berlin: Springer-Verlag, 1985.

[69] M. Kerker, *The Scattering of Light and Other Electromagnetic Radiation*. New York: Academic Press, 1969.

[70] J. Als-Nielsen and D. McMorrow, *Elements of Modern X-ray Physics*. West Sussex: Wiley, 2nd ed., 2011.

[71] M. Birkholz, *Thin Film Analysis by X-Ray Scattering*. Weinheim: Wiley-VCH, 2006.

[72] R. Borsali and R. Pecora, eds., *Soft-Matter Characterization*. New York: Springer, 2008.

[73] C. G. Camara, J. V. Escobar, J. R. Hird, and S. J. Putterman, "Correlation between nanosecond X-ray flashes and stick slip friction in peeling tape," *Nature*, vol. 455, no. October, pp. 1089–1093, 2008.

[74] G. Knoll, *Radiation Detection and Measurement*. Hoboken: John Wiley & Sons, Inc., 2000.

[75] Y. S. Lee, *Self-Assembly and Nanotechnology: A Force Balance Approach*. Hoboken: John Wiley & Sons, Inc., 2008.

[76] E. Lifshin, ed., *X-Ray Characterization of Materials*. Weinheim: Wiley-VCH, 1999.

[77] H. Lipson and H. Steeple, *Interpretation of X-Ray Powder Diffraction Patterns*. London: Macmillan, 1970.

[78] G. Margaritondo, *Elements of Synchrotron Light for Biology, Chemistry, and Medical Research*. Oxford: Oxford University Press, 2002.

[79] A. Michette and S. Pfauntsch, eds., *X-Rays: The First Hundred Years*. Chichester: John Wiley & Sons, Inc., 1996.

[80] M. Ristig and K. Gernoth, *Particle Scattering, X-Ray Diffraction, and Microstructure of Solids and Liquids*. Berlin: Springer-Verlag, 2003.

[81] G. Roberts, ed., *Langmuir-Blodgett Films*. New York: Plenum Press, 1990.

[82] R. Roe, *Methods of X-Ray and Neutron Scattering in Polymer Science*. Oxford: Oxford University Press, 2000.

[83] W. Schaetl, *Light Scattering from Polymer Solutions and Nanoparticle Dispersions*. Berlin: Springer-Verlag, 2006.

[84] D. Sivia, *Elementary Scattering Theory for X-Ray and Neutron Users*. Oxford: Oxford University Press, 2011.

[85] W. Sproull, *X-Rays in Practice*. New York: McGraw-Hill Book Company, Inc., 1946.

[86] N. Stribeck, *X-Ray Scattering of Soft Matter*. Berlin: Springer-Verlag, 2007.

[87] M. Tolan, *X-Ray Scattering from Soft-Matter Thin Films*. Berlin: Springer-Verlag, 1999.

[88] Y. Waseda, *Anomalous X-Ray Scattering for Material Characterization*. Berlin: Springer-Verlag, 2002.

[89] Y. Waseda, E. Matsubara, and K. Shinoda, *X-Ray Diffraction Crystallography: Introduction, Examples and Solved Problems*. Berlin: Springer-Verlag, 2011.

[90] T. R. Welberry, *Diffuse X-Ray Scattering and Models of Disorder*, vol. 48. Oxford: Oxford University Press, 2004.

[91] P. Wilmott, *An Introduction to Synchrotron Radiation: Techniques and Applications*. Chichester: John Wiley & Sons, Inc., 2011.

[92] H. Winick, ed., *Synchrotron Radiation Sources: A Primer*. Singapore: World Scientific, 1994.

[93] H. Young and R. Freedman, *University Physics with Modern Physics*. San Francisco: Pearson Addison Wesley, 11th ed., 2004.

[94] J. James, *A Student's Guide to Fourier Transforms With Applications in Physics and Engineering*. Cambridge University Press, 1995.